NBS TECHNICAL NOTE 1095

U.S. DEPARTMENT OF COMMERCE / National Bureau of Standards

A Study of Techniques for Measuring the Electromagnetic Shielding Effectiveness of Materials

Perry F. Wilson
Mark T. Ma

The National Bureau of Standards[1] was established by an act of Congress on March 3, 1901. The Bureau's overall goal is to strengthen and advance the nation's science and technology and facilitate their effective application for public benefit. To this end, the Bureau conducts research and provides: (1) a basis for the nation's physical measurement system, (2) scientific and technological services for industry and government, (3) a technical basis for equity in trade, and (4) technical services to promote public safety. The Bureau's technical work is performed by the National Measurement Laboratory, the National Engineering Laboratory, the Institute for Computer Sciences and Technology, and the Institute for Materials Science and Engineering.

The National Measurement Laboratory

Provides the national system of physical and chemical measurement; coordinates the system with measurement systems of other nations and furnishes essential services leading to accurate and uniform physical and chemical measurement throughout the Nation's scientific community, industry, and commerce; provides advisory and research services to other Government agencies; conducts physical and chemical research; develops, produces, and distributes Standard Reference Materials; and provides calibration services. The Laboratory consists of the following centers:

- Basic Standards[2]
- Radiation Research
- Chemical Physics
- Analytical Chemistry

The National Engineering Laboratory

Provides technology and technical services to the public and private sectors to address national needs and to solve national problems; conducts research in engineering and applied science in support of these efforts; builds and maintains competence in the necessary disciplines required to carry out this research and technical service; develops engineering data and measurement capabilities; provides engineering measurement traceability services; develops test methods and proposes engineering standards and code changes; develops and proposes new engineering practices; and develops and improves mechanisms to transfer results of its research to the ultimate user. The Laboratory consists of the following centers:

- Applied Mathematics
- Electronics and Electrical Engineering[2]
- Manufacturing Engineering
- Building Technology
- Fire Research
- Chemical Engineering[2]

The Institute for Computer Sciences and Technology

Conducts research and provides scientific and technical services to aid Federal agencies in the selection, acquisition, application, and use of computer technology to improve effectiveness and economy in Government operations in accordance with Public Law 89-306 (40 U.S.C. 759), relevant Executive Orders, and other directives; carries out this mission by managing the Federal Information Processing Standards Program, developing Federal ADP standards guidelines, and managing Federal participation in ADP voluntary standardization activities; provides scientific and technological advisory services and assistance to Federal agencies; and provides the technical foundation for computer-related policies of the Federal Government. The Institute consists of the following centers:

- Programming Science and Technology
- Computer Systems Engineering

The Institute for Materials Science and Engineering

Conducts research and provides measurements, data, standards, reference materials, quantitative understanding and other technical information fundamental to the processing, structure, properties and performance of materials; addresses the scientific basis for new advanced materials technologies; plans research around cross-country scientific themes such as nondestructive evaluation and phase diagram development; oversees Bureau-wide technical programs in nuclear reactor radiation research and nondestructive evaluation; and broadly disseminates generic technical information resulting from its programs. The Institute consists of the following Divisions:

- Inorganic Materials
- Fracture and Deformation[3]
- Polymers
- Metallurgy
- Reactor Radiation

[1]Headquarters and Laboratories at Gaithersburg, MD, unless otherwise noted; mailing address Gaithersburg, MD 20899.
[2]Some divisions within the center are located at Boulder, CO 80303.
[3]Located at Boulder, CO, with some elements at Gaithersburg, MD.

A Study of Techniques for Measuring the Electromagnetic Shielding Effectiveness of Materials

Perry F. Wilson
Mark T. Ma

Electromagnetic Fields Division
Center for Electronics and Electrical Engineering
National Engineering Laboratory
National Bureau of Standards
Boulder, Colorado 80303

U.S. DEPARTMENT OF COMMERCE, Malcolm Baldrige, Secretary

NATIONAL BUREAU OF STANDARDS, Ernest Ambler, Director

Issued May 1986

National Bureau of Standards Technical Note 1095
Natl. Bur. Stand. (U.S.), Tech Note 1095, 72 pages (May 1986)
CODEN: NBTNAE

U.S. GOVERNMENT PRINTING OFFICE
WASHINGTON: 1986

For sale by the Superintendent of Documents, U.S. Government Printing Office, Washington, DC 20402

CONTENTS

A STUDY OF TECHNIQUES FOR MEASURING THE ELECTROMAGNETIC SHIELDING EFFECTIVENESS OF MATERIALS

Perry F. Wilson
Mark T. Ma

Electromagnetic Fields Division
National Engineering Laboratory
National Bureau of Standards
Boulder, Colorado 80303

Shielding effectiveness relates to a material's ability to reduce the transmission of propagating fields in order to electromagnetically isolate one region from another. Because a complex material's shielding capability is difficult to predict, it often must be measured. A number of measurement approaches are studied including the use of a shielded room, coaxial transmission line holders, time domain signals, the dual TEM cell, and an apertured TEM cell in a reverberation chamber. In each case we consider the system's frequency range, test sample requirements, test field type, dynamic range, time required, analytical background, and present data taken on a common set of materials.

Key words: aperture coupling; coaxial transmission line holders; dual TEM cell; frequency domain; measurement techniques; reverberation chamber; shielded room; shielding effectiveness; shielding materials; time domain.

1. INTRODUCTION

How best to shield electronic equipment effectively is a concern of both equipment users and manufacturers. Proper shielding encompasses a number of different aspects including shielding of radiated electromagnetic interference (EMI), conducted EMI, grounding, electrostatic discharge, and environmental effects, all of which contribute to the overall integrity of a system. This report concentrates on the first area, namely, radiated rf interference. Shielding here refers to the ability of a material to reduce the transmission of propagating electromagnetic (EM) fields. Shields are used to isolate a region, either to prevent interference from outside sources (susceptibility), or to avoid the leakage of unwanted radiation due to internal sources (emissions). Traditionally, shielding is based on the use of metals whose EM properties are well understood. Increasingly, however, metals are being replaced by a variety of less predictable materials. Thus there is significant interest in the development of reliable methods for measuring the shielding effectiveness (SE) of a material. An example serves to illustrate the problem.

Molded plastics have largely replaced metal boxes as the housings for commercial electronic equipment. Plastics alone are inherently transparent to EM radiation; therefore, some metal-like property must be added to insure adequate shielding. Existing approaches include conductive sprays, metal fibers injected during the molding stage, zinc arc spraying, electro- and electroless-plating, foil inserts, and other metallization processes [1], [2]. Shielding-associated expenses may well exceed 10% of an item's production cost [3]. It is important to make effective choices as to which shielding method is best suited to a particular application, especially where large production runs are planned. Recent FCC regulations applicable to commercial electronics combined with the adverse consequences of failing to pass FCC testing make the need for useful SE data at the design level all the more acute. Similar problems exist in avionics applications where, for example, graphite composites are replacing metal airframes.

Shielding problems involve a variety of EM environments. Therefore, SE measurements seek to either reproduce potential EM conditions, or to yield sufficient information to predict a material's shielding response based on some theoretical model. The basic variables of interest are: (1) frequency, (2) the incident field distribution, and (3) variations in the material under test. A few words about each of these parameters are in order.

Potentially interfering sources cover a broad spectrum due to both man-made and natural sources. Present interest is in SE data covering 100 kHz to 1 GHz. This range includes domestic FCC rules governing emissions from computing devices (Code of Federal Regulations, Title 47, Part 15, Subpart J, adopted Oct. 1979), the German VDE 0871/6.78 standard which is essentially that also proposed by CISPR [4] affecting commercial equipment sold to EEC communities and Japan, and most military requirements such as MIL-STD-461. In the near future, SE data up to 10 GHz are likely to be needed.

Interfering EM fields depend on the source type and location. Susceptibility requirements usually involve EMI originating from distant sources such as communications links, radio transmitters, lightning, etc. Thus the incident fields are plane wave in nature which leads to a need for far-field SE data. On the other hand, emissions problems often involve internal sources which may be very close to the shield material. Such near-field sources may be further classified into those which produce a high-impedance field (electric field dominant) such as a short dipole, and those that produce a low-impedance field (magnetic field dominant) like a small loop antenna. The transition point between the near- and the far-field is a distance of approximately $\lambda/2\pi$. Thus a source which at one frequency is in the near field may become a far-field source at higher frequencies. Actual shielding problems are likely to involve a combination of all of the above conditions.

Because numerous shielding materials are available, SE test methods need to be flexible enough to allow for different sample types. Materials will vary in thickness, mechanical properties, cost, as well as electrical properties. Certain test methods require that the sample be of a very specific shape to within certain tolerances. This may present a problem if the material is difficult to machine or lacks rigidity. Poor surface conductivity may be a problem if good contact to metal surfaces is necessary for a valid measurement, particularly, since most composites and plastic metallizations contain significant amounts of insulating material.

In addition to the variables mentioned above (frequency, incident field type, test material), other important considerations merit attention as well. The cost of a test system may well determine whether it is widely used. The time required to obtain data, another form of cost, can be critical making it desirable that we develop automated test systems. Repeatability is a concern. If separate groups cannot obtain like data on equivalent samples then a method is ill suited to widespread use. A large dynamic range is useful. Presently, 100 decibels is a practical limit. Materials with very different shielding capabilities may give similar results should the data fall below the noise floor. Finally, careful consideration must be given to the interpretation of SE data. Both the material's intrinsic shielding capabilities and the measurement system itself contribute to the resulting SE data. Explaining this interplay is greatly aided by developing meaningful theoretical models of measurement systems whenever possible.

The purpose of any SE test procedure is to quantitatively measure the insertion loss which results from introducing the test sample. The basic routine is depicted in figure 1. Power from a transmitter (P_t) is coupled to a receiver, first with no material present (P_r) in order to establish a reference level, and second with the sample introduced (P_r'). We will designate any measurement performed with the sample in place with a prime. In each case the source output level P_t is kept the same. The ratio of the two received powers gives the insertion loss (IL), typically expressed in decibels,

$$IL = 10\log|P_r/P_r'| \quad \text{dB.} \tag{1}$$

Beyond this basic definition the particulars of the various SE test procedures vary significantly.

Section 2 will briefly address the above-mentioned problem of separating the material's shielding capability from the properties of the measurement system itself. The discussion points out that external factors such as the antennas used, the incident field type and its

orientation, antenna separation, aperture effects, and contact impedances can all significantly affect the resulting IL data. Is one measuring the materials shielding behavior or the change in some other EM characteristic when the sample is inserted? A small-aperture coupling model enables us to identify a number of such factors which need to be considered when attempting to interpret IL data in terms of intrinsic material SE. In addition, since a number of test procedures do in fact feature aperture coupling as a method of keeping the sample small, this discussion gives some necessary theoretical background for analyzing those test configurations.

In examining the specific SE measurement methods, each section begins with some background on the test configuration, such as the equipment used, dimensions, applicable frequency range, incident test field type, sample sample requirements, dynamic range, etc. This is followed by some analysis of the system. Whenever applicable an $\exp(j\omega t)$ time convention is assumed. The shield-material parameters of interest will be conductivity σ, permittivity $\varepsilon = \varepsilon_r \varepsilon_0$ and permeability $\mu = \mu_r \mu_0$, where ε_0 and μ_0 are the free-space values and ε_r and μ_r the material's relative permittivity and permeability respectively, and thickness d. Unfortunately, these parameters are not accurately known for our test materials. In each case we attempt to use the same set of test materials thereby giving us some basis for comparing different methods. Samples include a pair of reference materials, namely, layers of gold or aluminum on Mylar. Since these materials have well defined electrical properties they can be used to examine the validity of theoretical models. Known materials also allow us to try and identify those parasitic factors of the measurement system which have not, or cannot be well controlled. In addition to these so called reference samples two realistically messy samples will be tested, these being a layered plastic- aluminum-plastic fabric-like material, and a graphite-loaded composite. Both these samples feature significant metal content but also have highly insulating surfaces. This allows us to consider the effect of contact impedance and nonhomogeneity. Other special samples, such as high permeability magnetic type materials, are tested in some cases.

Section 3 gives a discussion of the shielded-room SE measurement approach. This method is based on a modification of MIL-STD 285 [5] which specifies procedures for measuring the SE of the room itself. A source antenna is placed inside the shielded room and the receiving antenna outside. Coupling is by an aperture placed in one of the room walls. The main advantage of this approach is that shielded rooms are widely available. Unfortunately, the difficulties associated with this method are numerous, primarily due to multimoding in the room. Slight shifts in antenna positioning or in the operating frequency can cause dramatic differences both in the fields incident on the sample and in the IL data. Thus for present applications the use of shielded rooms does not appear to be promising.

Next we consider two methods based on the use of circular coaxial transmission-line holders. Section 4 examines the American Society for Testing and Materials (ASTM) proposed version. The holder is essentially an expanded section of 50 ohm circular coaxial line, operated in the dominant TEM mode. It may be disassembled to allow the insertion of an annular (washer-shaped) test sample. The equations describing reflection and transmission in the coaxial line are discussed in Appendix A and are equivalent to those describing a free space plane wave normally incident on an infinite sheet of the sample. Thus the coaxial holder simulates far-field shielding behavior. The advantage of this approach is both its ease of use and analysis. The primary difficulty is that contact impedance between the sample and coaxial holder's conductors can significantly degrade the measured results.

Section 5 considers a second type of circular coaxial holder, namely, a flanged version developed at NBS. It is similar to the ASTM model, except that instead of continuously connected conductors, a solid disk of the material is mounted between two large flanges and capacitive coupling is used to propagate the TEM mode through the sample. The unloaded reference measurement involves two pieces of the sample matching the dimensions of the flanges but leaving the space between the inner and outer conductors empty. This tends to overcome the contact impedance problem except at frequencies too low to generate sufficient displacement current. In general this fixture works well and should give repeatable far-field equivalent IL data. The flanged coaxial holder is a more difficult fixture to model than is the ASTM version. Appendix B considers an equivalent circuit description which enables us to examine factors such as the effect of insulating surfaces.

The two circular coaxial-holder techniques involve the use of waveguides operating in the fundamental TEM mode. Thus there is an upper frequency limit to their use due to the appearance of higher-order modes which confuse the incident field distribution and make the

interpretation of results difficult. In order to gain plane wave SE data at frequencies above those covered by the coaxial holders, a time domain technique is being considered, as discussed in Section 6. The sample is either a large sheet or a small sample mounted over an aperture in a large copper screen. A short pulse is used as the source signal. All unwanted signal paths to the receiving antenna can be time windowed out and only the direct path signal retained. This avoids problems due to diffracted fields and makes the sample or the copper sheet appear to be infinite in extent. Time domain measurements are very fast and give information at frequencies well above those of the other techniques considered here. Unfortunately, much of the equipment required for these measurements is, at present, unique to NBS thus it may be difficult for others to duplicate our results. In addition, this system may not be well modeled theoretically in any simple fashion.

The coaxial holders and the time domain techniques have simulated incident plane waves and thus should be considered far-field approaches. By contrast, the dual TEM cell (DTC), considered in Section 7, allows us to examine the coupling of an electric field component and a magnetic field component separately. Thus, the DTC gives us information as to the near-field shielding capability of the material, so important in emissions type EMI prevention. Dual TEM cell coupling can be nicely described theoretically.

The dual TEM cell fixture essentially uses one cell to drive another via a common aperture. The cells need to be fairly large to allow the internal mounting of the sample and proper joining of the cells. As a result the upper frequency limit is not great. An alternative approach is to use a small, apertured TEM cell as the receiver and a high frequency source as the driver. This is the idea behind an apertured TEM cell in a reverberation chamber as discussed in Section 8. The reverberation chamber allows us to generate a high frequency, statistically known field while the TEM cell receiver again allows us to consider the shielding of electric- and magnetic-field components separately. The analysis of this system is very similar to that of the DTC. At present, half of the DTC is used as the apertured TEM cell, thus the high frequency limit is the same. Therefore the study here is simply to establish the feasibility of such an approach.

The above list of SE test procedures is by no means exhaustive. Rather, it is simply the group of methods that have to date been considered in some detail at NBS. Section 9 gives information on other methods which have either appeared in the literature such as the dual-box method proposed by the ASTM as a near-field SE simulation, the transfer impedance technique, near-field coupling using dipole sources, complex-permittivity measurements, and methods under consideration at NBS which have not yet been well explored. These include the use of loaded rectangular waveguides both to go higher in frequency than can coaxial transmission lines and to avoid the contact-impedance problem, and the use of nested reverberation chambers to go to high frequencies.

The concluding remarks of Section 10 attempt to summarize the various SE test system characteristics and their range of applicability in a tabular form for quick reference. Some tentative recommendations as to which methods appear to be the most promising are also discussed. Given the wide variety of potential test conditions and materials it is unlikely that any single method will prove adequate to meet all SE data demands. Rather, some combination of different approaches will be required. It may well be that the intended use of the sample will dictate which measurement method is "best". Therefore it is important to examine as many different test approaches as is practical.

2. FACTORS INFLUENCING SHIELDING EFFECTIVENESS MEASUREMENTS

The simplest model of an EM shield is an infinite plane sheet separating a source from a receiver. This case is fundamental to understanding shielding theory. Much work has been done on this problem including Schelkunoff's basic transmission line description [6]-[10] applicable to planar sheet, cylindrical, and spherical shielding, as well as the important case of low-impedance (magnetic) field shielding [11]-[14]. An analysis of the infinite plane sheet case reveals the basic mechanisms by which a material provides shielding: reflection, absorption, and internal re-reflection [11]. Realistically, infinitely large test samples are not possible. Consequently, a number of test procedures involve covering an aperture with a relatively small piece of shield material. Therefore, it is instructive to consider the problem of EM coupling through an aperture. Specifically, we will examine coupling through an electrically small aperture (i.e. of dimensions much less than a wavelength) in a very large, perfectly conducting sheet, as depicted in figure 2. Our intention is to use this model as the means for illustrating both intrinsic and external variables which affect SE measurements.

Consider the geometry shown in figure 2a. A set of fields, $\bar{E}_i$, $\bar{H}_i$, is incident on an empty aperture in a perfectly conducting screen. A cylindrical coordinate system (ρ,ϕ,z) will be located at the aperture center, with the z axis directed normally to the aperture surface as shown. If the aperture is electrically small then the fields penetrating the aperture to the other side of the screen (z>0) will be similar to those produced by a set of equivalent dipole moments. The formal derivation of small-aperture coupling is well detailed elsewhere [15]. The present discussion requires only that we quote one basic result; namely, the fields produced by the dipoles [16]:

$$\bar{E}(R,\omega) = \frac{e^{-jk_0R}}{4\pi\varepsilon_0}\left\{\left(\frac{1}{R^3} + j\frac{k_0}{R^2}\right)\left[3\hat{R}(\hat{R}\cdot\bar{P}_0) - \bar{P}_0\right] - \frac{k_0^2}{R}\left[\hat{R}\times(\hat{R}\times\bar{P}_0)\right] + \frac{1}{c}\left(j\frac{k_0}{R^2} - \frac{k_0^2}{R}\right)\left[\hat{R}\times\bar{M}_0\right]\right\}$$

$$\bar{H}(R,\omega) = \frac{e^{-jk_0R}}{4\pi}\left\{\left(\frac{1}{R^3} + j\frac{k_0}{R^2}\right)\left[3\hat{R}(\hat{R}\cdot\bar{M}_0) - \bar{M}_0\right] - \frac{k_0^2}{R}\left[\hat{R}\times(\hat{R}\times\bar{M}_0)\right] - c\left(j\frac{k_0}{R^2} - \frac{k_0^2}{R}\right)\left[\hat{R}\times\bar{P}_0\right]\right\} \tag{2}$$

where $k_0 = \omega/c$, c is the speed of light in vacuum, $R = (\rho^2 + z^2)^{1/2}$ is the distance from the aperture center to the observation point $\hat{\rho}\rho + \hat{z}z$, $\hat{R}$ is the normalized position vector ($\hat{R} = [\hat{\rho}\rho + \hat{z}z]/R$), $\bar{P}_0$ is the equivalent electric-dipole moment due to the aperture fields, and $\bar{M}_0$ is the equivalent magnetic-dipole moment.

The dipole moments depend on both the incident fields exciting the aperture and the geometry of the aperture. This situation leads to the following decomposition:

$$\bar{P}_0 = \bar{\bar{\alpha}}_e\cdot\varepsilon_0\bar{E}(\bar{0}) = \hat{z}\varepsilon_0\alpha_e E_z(\bar{0})$$

$$\bar{M}_0 = \bar{\bar{\alpha}}_m\cdot\bar{H}(\bar{0}) = \hat{\rho}\alpha_m H_\rho(\bar{0}) \tag{3}$$

where $\bar{\bar{\alpha}}_e$ and $\bar{\bar{\alpha}}_m$ are the electric and magnetic aperture polarizability dyadics (the geometry factor), and $\bar{E}(\bar{0})$ and $\bar{H}(\bar{0})$ are the incident fields at the aperture center $(\bar{0})$. The electric-dipole moment will be normal to the aperture ($\bar{\bar{\alpha}}_e = \hat{z}\alpha_e\hat{z}$) while the magnetic-dipole moment will be tangent ($\bar{\bar{\alpha}}_m = \hat{\rho}\alpha_m\hat{\rho}$) where, as implied by (3), we have oriented the ρ axis to coincide with the tangential component of the incident magnetic field.

Equations (2) and (3) together yield expressions for the penetrating fields. For the near-field ($k_0R<<1$) and far-field ($k_0R>>1$) cases, we find respectively that:

$$\bar{E}(R,\omega) = \frac{\alpha_e E_z(\bar{0})}{4\pi}\frac{e^{-jk_0R}}{R^3}\left[\hat{\rho}\frac{3\rho z}{R^2} + \hat{z}\left(\frac{3z^2}{R^2} - 1\right)\right] \qquad \text{(near field)}$$

$$\bar{H}(R,\omega) = \frac{\alpha_m H_\rho(\bar{0})}{4\pi}\frac{e^{-jk_0R}}{R^3}\left[\hat{\rho}\left(\frac{3\rho^2}{R^2} - 1\right) + \hat{z}\frac{3\rho z}{R^2}\right]; \tag{4}$$

and

$$\bar{E}(R,\omega) = -\frac{k_0^2}{4\pi}\frac{e^{-jk_0R}}{R}\left[\frac{\rho}{R}\left(\hat{\rho}\frac{z}{R} - \hat{z}\frac{\rho}{R}\right)\alpha_e E_z(\bar{0}) + \hat{\phi}\eta_0\frac{z}{R}\alpha_m H_\rho(\bar{0})\right]$$

(far field)

$$\bar{H}(R,\omega) = -\frac{k_0^2}{4\pi}\frac{e^{-jk_0R}}{R}\left[-\frac{z}{R}\left(\hat{\rho}\frac{z}{R} - \hat{z}\frac{\rho}{R}\right)\alpha_m H_\rho(\bar{0}) + \hat{\phi}\frac{1}{\eta_0}\frac{\rho}{R}\alpha_e E_z(\bar{0})\right],$$

where $\eta_0 = 120\pi$ is the free-space impedance.

A typical receiving antenna will respond primarily to either the electric or magnetic field with the received power proportional to the square of the appropriate component in the far-field case. Thus, each of the field components in (4) leads to a type of insertion loss measurement via (1). Idealizing the problem, we let $\bar{A}$ represent the receiving antenna's response to any of the field components, denoted by $\bar{F}(R,\omega)$. The far-field insertion loss should then behave like

$$IL = 20 \log \left|\frac{\bar{F}(R,\omega)\cdot\bar{A}}{\bar{F}'(R,\omega)\cdot\bar{A}}\right|, \tag{5}$$

where the loaded aperture case is depicted in figure 2b. This expression is not strictly applicable to near-field indertion loss measurements. However, it can be used to indicate the types of variable dependencies that might occur.

Equation (5), with one of the field components in (4) inserted, may now be used to examine some of the factors influencing insertion loss measurements. It should again be emphasized that (5) does not represent any specific measurement procedure per se. Rather, it serves to illustrate some basic properties likely to be encountered in shielding studies featuring coupling through an aperture. We will consider the following variables: receiving antenna orientation, incident field distribution, and shielding material parameters.

Intuitively one would probably locate the receiving antenna along the z axis, or boresight. In this case, $\rho = 0$ and (4) along with (5) yields

$$IL = 20\log\left|\frac{\alpha_e E_z(\bar{0})}{\alpha_e' E_z'(\bar{0})}\right| = IL_E$$

$(\hat{z}\cdot\bar{A} \neq 0,\ \bar{E}\text{-measured in the near field})$,

$$IL = 20\log\left|\frac{\alpha_m H_\rho(\bar{0})}{\alpha_m' H_\rho'(\bar{0})}\right| = IL_H \tag{6}$$

$(\hat{\rho}\cdot\bar{A} \neq 0,\ \bar{H}\text{-measured in the near field})$

$$IL = IL_H \quad \left\{ \begin{array}{l} \hat{\phi}\cdot\bar{A} \neq 0,\ \bar{E}\text{-measured, far field} \\ \hat{\rho}\cdot\bar{A} \neq 0,\ \bar{H}\text{-measured, far field} \end{array} \right\}.$$

In the near-field case, insertion loss depends on either electric field coupling (IL_E) or magnetic field coupling (IL_H) through the material. If, however, the receiving antenna is located in the far field, (6) reveals that we are measuring the material magnetic shielding properties regardless of the type of receiving antenna used. For a typical conductive shield

material, the difference between IL_E and IL_H can be large. Thus, IL can change significantly as we move from the near field to far field, as might be expected.

Another consideration is the effect that loading the aperture has on the incident waveform. Ideally, the incident fields will be unchanged, that is, $E_z(\bar{0}) = E'_z(\bar{0})$ and $H_\rho(\bar{0}) = H'_\rho(\bar{0})$. If this is indeed the case, then

$$\begin{aligned} IL_E &\to 20\log|\alpha_e/\alpha'_e| \\ IL_H &\to 20\log|\alpha_m/\alpha'_m| \ , \end{aligned} \tag{7}$$

which is preferable, since we are primarily interested in measuring the material's shielding properties contained in α'_e and α'_m. In general, the loading of the aperture could affect the transmitting antenna's characteristics, especially if the aperture is located in the near field of the transmitter. In fact, viewing the aperture as an impedance, loading the aperture might actually provide a better impedance match leading to greater field penetration with the shield material in place. This type of "gain" behavior has been observed in practice.

Suppose we now shift the receiving antenna from a boresight location to a grazing orientation (z=0). Insertion loss should then behave as follows:

$$\begin{aligned} IL_E \quad & (\hat{z} \cdot \bar{A} \neq 0, \ \bar{E}\text{-measured in either the near, or far field}) \\ IL_H \quad & (\hat{\rho} \cdot \bar{A} \neq 0, \ \bar{H}\text{-measured in the near field}) \\ IL_E \quad & (\hat{\phi} \cdot \bar{A} \neq 0, \ \bar{H}\text{-measured in the far field}) \ , \end{aligned} \tag{8}$$

resulting in a new set of field coupling dependencies. For receiving antenna orientations between these two extremes, both electric and magnetic field couplings will contribute.

Three types of incident fields are usually associated with shielding measurements: plane wave, high impedance, and low impedance. For a plane wave, assuming normal incidence, both the electric and magnetic fields will be tangent to the aperture. Thus, $E_z(\bar{0}) = 0$, and in all cases (5) reduces to

$$IL \to IL_H \qquad \text{(normal plane wave)} \ . \tag{9}$$

For a plane wave incident from a grazing angle, two polarizations are possible: $\bar{E}$ in or perpendicular to the plane of incidence. In the latter case, both $E_z(\bar{0})$ and $H_\rho(\bar{0})$ are zero and negligible fields will be coupled through the aperture. For $\bar{E}$ parallel to the plane of incidence, both $E_z(\bar{0})$ and $H_\rho(\bar{0})$ are present with $E_z(\bar{0}) = \eta_0 H_\rho(\bar{0})$. If the receiving antenna is also in the far field, we find that

$$IL = 20\log\left|\frac{E_z(\bar{0})\left\{\frac{\rho}{R}\left[\hat{\rho}\,\frac{z}{R} - \hat{z}\,\frac{\rho}{R}\right]\alpha_e + \hat{\phi}\,\frac{z}{R}\,\alpha_m\right\}\cdot\bar{A}}{E'_z(\bar{0})\left\{\frac{\rho}{R}\left[\hat{\rho}\,\frac{z}{R} - \hat{z}\,\frac{\rho}{R}\right]\alpha'_e + \hat{\phi}\,\frac{z}{R}\,\alpha'_m\right\}\cdot\bar{A}}\right|$$

($\bar{E}$ measured in the far field, incident grazing plane wave)

(10)

$$IL = 20\log\left|\frac{E_z(\bar{0})\left\{\frac{z}{R}\left[\hat{\rho}\,\frac{z}{R} - \hat{z}\,\frac{\rho}{R}\right]\alpha_m + \hat{\phi}\,\frac{\rho}{R}\,\alpha_e\right\}\cdot\bar{A}}{E'_z(\bar{0})\left\{\frac{z}{R}\left[\hat{\rho}\,\frac{z}{R} - \hat{z}\,\frac{\rho}{R}\right]\alpha'_m + \hat{\phi}\,\frac{\rho}{R}\,\alpha'_e\right\}\cdot\bar{A}}\right|$$

($\bar{H}$ measured in the far field, incident grazing plane wave).

If the receiving antenna is located in the near field, then IL → IL_E if $\bar{E}$ is measured, while IL → IL_H if $\bar{H}$ is measured. Equation (10) indicates that both electric and magnetic shielding properties are important for the grazing plane-wave case, whereas a normal plane wave (9) largely tests inductive-shielding properties only. As discussed in the previous section, the effects of α_e and α_m in (10) may be decoupled individually by reorienting the receiving antenna.

If a high-impedance incident field is applied, as for example produced by an electric dipole near the aperture, then $H_\rho(\bar{0}) << E_z(\bar{0})$ and

$$IL \to IL_E \text{ (high-impedance field)} \tag{11}$$

independent of the receiving antenna type. By analogy, a low-impedance field implies that $H_\rho(\bar{0}) >> E_z(\bar{0})$, thus

$$IL \to IL_H \text{ (low-impedance field)} \tag{12}$$

in all cases. Comparing (12) and (9), we see that insertion-loss measurements using coaxial magnetic loops should yield results similar to those based on a normally incident plane wave if aperture coupling is used. This is not expected to hold true for large apertures however. If we were coupling fields through a plane sheet of material, this conclusion would not hold since in one case the wave impedance is low (loops) and in the other (plane wave) the wave impedance is η_0. Again, it should be emphasized that the range of values defined by IL_E and IL_H can be large, thus the choice of incident field significantly affects the resulting insertion loss measurements. This point will be illustrated by considering some typical material parameters, but first a bit about aperture polarizabilities.

The aperture polarizabilities α_e and α_m depend on the shape, size, and the possible loading of the aperture. They alone constitute a problem of longstanding interest. For our present purposes we need only quote a few results. Apertures associated with SE measurements are typically either square or circular. For a square aperture of side length s oriented so that one side is parallel to the $\hat{\rho}$ axis one finds that [17]

$$\begin{aligned} \alpha_e &\approx -0.114 s^3 \\ \alpha_m &\approx 0.258 s^3 , \end{aligned} \tag{13}$$

and for a circular aperture of radius r that [15]

$$\begin{aligned} \alpha_e &= -\frac{2}{3} r^3 \\ \alpha_m &= \frac{4}{3} r^3. \end{aligned} \tag{14}$$

up to terms of the order $(k_0 s)^2$ and $(k_0 r)^2$.

The polarizabilities of loaded apertures are more difficult to determine. We can adapt a result developed by Casey [18] who examined a circular aperture backed by a conducting sheet of impedance Z_s. He finds that

$$\frac{\alpha_m}{\alpha_m'} \approx \left[1 + j\,\frac{4\omega\mu_0 r}{3\pi(Z_s + 2\pi R_c)}\right] ,$$

$$\frac{\alpha_e}{\alpha_e'} \to \infty \qquad (15)$$

up to the order of terms like $(k_0 r)^2$, where R_c is the contact resistance between the material and the conducting plane containing the aperture. The sheet impedance of a lossy material of thickness d is given by [19]

$$Z_s = \eta\,\mathrm{csch}\gamma d$$

$$\eta \approx (j\omega\mu/\sigma)^{1/2} \; ; \qquad \gamma \approx (j\omega\mu\sigma)^{1/2} . \qquad (16)$$

If the material is electrically thin (i.e. $|\gamma d| << 1$) then this reduces to

$$Z_s \approx 1/\sigma d , \qquad (17)$$

which is a frequently used form. Inserting the latter expression into the loaded-aperture polarizabilities above (15) yields

$$\frac{\alpha_m}{\alpha_m'} = 1 + \frac{j\ 160\ k_0 r\ \sigma d}{1 + 2\pi\ \sigma d R_c} ,$$

$$\frac{\alpha_e}{\alpha_e'} \to \infty . \qquad (18)$$

As indicated, to this order of approximation, α_e' is negligible.

For a loaded square aperture we can readily generate an equivalent radius if we note that polarizabilities tend to be insensitive to shape. We choose r such that α_m is the same for a circular and square aperture in the unloaded case, i.e. $r = 0.58\ s$. The magnetic polarizability ratios (15) and (18) depend on material properties (σ and d) as desired, but also on the aperture size ($k_0 r$) and the contact resistance R_c, which have no intrinsic relationship to the material EM shielding properties. Given any SE measurement procedure, it is important to recognize these extrinsic factors even if they cannot be isolated.

Equation (18) may be inserted into (7) to generate some representative values for IL_H and IL_E. We see that $IL_E \to \infty$ for this approximation. Clearly, this will not be the case in practice, but it is well known that any reasonable conductor will provide high levels of shielding against electric fields. Magnetic-field shielding, as measured by IL_H, tends to be significantly lower for most materials. For example, suppose an aluminum sheet [$\sigma = 3.72(10)^7$ S/m] of thickness $d = 1.27\ (10)^{-4}$ m [0.005 in] is deposited on a plastic substrate. This might model a conductive spray applied to the plastic housing. Assuming that $H_\rho(\bar{0}) \approx H_\rho'(\bar{0})$, and choosing $k_0 r = 0.2$ as a typical value for a small aperture, we obtain

$$IL_H = 10\ \log\left\{1 + \left[\frac{1.51(10)^5}{1 + 2.96(10)^4\ R_c}\right]^2\right\} \qquad \text{dB.} \qquad (19)$$

If the contact resistance is zero, then IL_H = 103.6 decibels indicating good magnetic-field shielding. However, suppose some contact resistance exists, say R_c = 0.01 ohms. Then IL_H reduces to 54.1 decibels. If R_c rises to 1 ohm, then IL_H = 14.3 decibels. Thus, a 1-ohm contact resistance reduces IL_H by 89.3 dB, a significant change which has nothing to do with the material itself. In fact, variations in R_c could mask the actual material shielding properties. Contact resistance could be a problem where conductivity filled plastics are used since surface resins may cause R_c to be relatively high. The above example also indicates that the range defined by IL_E and IL_H can be large. As discussed, changing the antenna positioning or the incident field distribution can shift IL measurements between these values. One is tempted to speculate that, given any shield material, one could obtain any desired level of IL by changing the various factors.

Thus we see that insertion loss data may well depend more on the measurement procedure than on the material tested. When evaluating the shielding capability of various materials, it is very important to understand how shielding data are obtained.

3. SHIELDED ROOM - CW SOURCE

3.1 Test Configuration

The shielded room approach is based on a modification of MIL-STD 285 [5] which details procedures for measuring the SE of the shielded room itself. Shielded rooms are used to isolate electronic equipment from outside sources or receivers. Because they are widely available, the shielded room SE measurement method has seen significant usage. The measurement system consists of placing antennas inside and outside the shielded room. The two antennas couple via an aperture (loaded and unloaded) located in one of the walls. The screen room in use at the NBS is of dimensions 2.34 m x 2.10 m x 3.00 m with a 46-cm square aperture centrally located in one of the side walls. Frequency coverage from 30 MHz to 1 GHz is achieved using tuned dipoles, biconical, and TEM horn antennas. The receiving antenna is pointed directly at the aperture center (boresight). The transmitting (interior) antenna location can be varied although it should remain fixed while generating any individual SE curve. The incident field distribution is largely unknown. The sample must be large enough to cover the aperture and is mounted on the outside wall. A square brass ring is used to both hold the sample in place and to create electrical contact between the sample and the shielded room wall. The brass mounting ring is also in place during unloaded measurements. The dynamic range of the present system is 80-90 decibels.

3.2 Analytical Background

The shielded room acts as a cavity resonator potentially supporting a large number of modes. This tends to make the field distribution within the shielded room difficult to specify. Resonances begin at 81 MHz in the NBS shielded room and above 100 MHz we expect significant multi-moding. The excitation of these resonances varies both with frequency, and with the location of the transmitting antenna. For example, point to point coupling in a shielded room deviates up to ± 40 dB from the same measurement performed in an anechoic chamber [20]. As a result, slight shifts in transmitter location and frequency can dramatically affect the field distribution exciting the aperture. Loading the aperture with the sample introduces an additional loss mechanism which may affect the Q of the room and thus the field distribution.

At lower frequencies for which the aperture dimensions are electrically small, the model described in Section 2 applies and more can be said about the expected behavior of the SE data. For a boresight located receiving antenna eq. (6) implies that $IL \rightarrow IL_E$ or IL_H if the receiving antenna is in the near-field and responds to the E-field or H-field respectively, and $IL \rightarrow IL_H$ if the receiving antenna is located in the aperture far-field. Mendez [21] has analyzed aperture leakage from a cavity excited by elementary sources and operating below resonance. His formulation also indicates that $IL \rightarrow IL_H$ for a far-field located, boresight-oriented receiving antenna.

One approach to overcoming the difficulties caused by multimoding in a shielded room is to line the room with absorber [22]. This tactic may not be affordable for large rooms or workable at all frequencies, but where applicable it should lead to more stable results. Besides damping resonances, the absorber alters the field distribution exciting the aperture as compared to an unlined room. On a conducting wall the tangential electric and normal magnetic field components are zero. Thus the fields exciting a small aperture should be nominally the normal electric and tangential magnetic components. With the absorber in place, the room walls should behave like black screens. Since there is no reflection, the fields exciting an aperture in a black screen should be simply the incident field; for example, a plane wave if the transmitting antenna is $\lambda/2\pi$ removed from the aperture. We can adapt the small aperture theory of Section 2 by letting

$$\bar{P} = \hat{\rho}\varepsilon\alpha_e E_\rho(\bar{0})$$
$$\bar{M} = \hat{\phi}\alpha_m H_\phi(\bar{0}) \qquad (20)$$

corresponding to a plane wave incident along the z-axis. This leads to a boresight insertion loss value of

$$IL \to 20 \log \left| \frac{\alpha_e + \alpha_m}{\alpha_e' + \alpha_m'} \right| \qquad (21)$$

irrespective of whether $\bar{E}$ or $\bar{H}$ is measured. The polarizabilities of an aperture in a black screen are not available, but if they are similar to the conducting screen case, then equation (21) raises the possibility of a "gain" measurement when the sample is inserted. Referring to (13) and (14), we see that normally for an aperture in a conducting screen α_e and α_m are of opposite sign. For typical conducting materials (15) indicates that $\alpha_e' \ll \alpha_m'$, thus $\alpha_e' + \alpha_m' \approx \alpha_m'$. At low frequencies where conductive samples are not good magnetic field (low-impedance) shields, although $|\alpha_m'| < |\alpha_m|$, we may have $|\alpha_m'| > |\alpha_e + \alpha_m|$ leading to negative insertion loss. This precise phenomenon has shown up in measurements made on fairly low-loss plastics by Bodner et. al. [22] using a black screen box. An example is reproduced here as figure 3. Because $|\alpha_m'|$ decreases as frequency increases, negative insertion loss occurs only at lower frequencies. As the conductivity of their sample increased, this slight gain dip disappears due to increased absorption and reflection of the magnetic fields which results in the condition $|\alpha_e + \alpha_m| > |\alpha_m'|$. Nonetheless, gain measurements when the shield material is inserted are both surprising and possible.

A second approach to overcoming multimoding is to average, or smooth the measurement by using multiple transmitting and receiving antenna locations. This would create a spectrum of fields exciting the aperture ranging from low, to high impedance in nature. If enough different combinations are used then the average should give a reasonably well behaved SE value. Clearly, making frequent changes in antenna locations and repeating the measurement would prove prohibitively time consuming. Thus the concept of mode stirring or mode tuning has been introduced. Rather than repositioning the antennas, a rotating paddle causes the boundary conditions within the shielded room to continuously change [23] thereby creating the same averaging effect. This technique is data intensive and depends on a high level of automation in order to be practical. A variation of MIL-STD 1377 [24]-[25] which details test procedures for investigating cable leakage, shielded box integrity etc., is also being considered. A shielded box is placed in a shielded room. Each features a paddle wheel tuner. An aperture in the box is used to couple energy between the two. The nature of the fields penetrating the sample in the reverberation chamber is complicated, however, as the chamber becomes highly multi-moded the average field impedance tends toward the free-space intrinsic impedance [23]. Thus somewhat paradoxically, the data obtained in the above fashion may be considered far field in nature.

3.3 Data and Discussion

Because the walls of the shielded room are highly conductive, both the tangential electric field and normal magnetic field components will be negligible at the wall surfaces. Thus we nominally have the normal electric field and tangential magnetic field components exciting the aperture, especially when the aperture is electrically small. However, The multi-moding within the room means that little can be said about the ratio of the two field components (impedance) exciting the aperture. The fields, and thus the incident field impedance, can shift dramatically with small changes in frequency, thus shielded room data tend to be highly variable. These shifts also mean that data points need to be closely spaced. In addition, measured results are not easily repeated. Some smoothing of the data follows from using multiple source locations and averaging the results in a manner similar to the reverberation chamber approach mentioned above. This is necessarily very time consuming. The NBS approach at present is to use two source locations. A single IL curve from 1 MHz to 1 GHz can take 30-40 hours. Some automation may be possible, but not enough to significantly reduce the required effort.

Figure 4 shows an example of the data obtained from two antenna positions. The sample is the plastic-aluminum-plastic layered material. Horn antennas were used as both the source and receiver each at distances of 0.38 m (• curve) and 0.56 m (* curve) from the aperture. Thus both were in the far-field of the aperture ($\lambda/2\pi$ = 0.38 m, 0.56 m at 125, 85 MHz) if room effects are ignored. The aperture is not electrically small at the frequencies tested (400-600 MHz) in this curve. As may be seen, the data do tend to vary with small changes in frequency up to 10 dB in this case. This is likely due to the changes in the incident field impedance. The two curves representing different antenna locations tend to track each other somewhat and averaging will reduce fluctuations only slightly. This is not unexpected since at these frequencies the 18 cm shift in antenna position is much less than a wavelength. Thus the modal distribution excited should remain similar. At still higher frequencies we would expect to see more significant variations between the two curves.

Measurements similar to those above were performed on the same plastic-aluminum-plastic sample from 50 to 1000 MHz. The results are shown in figure 5. These data represent multiple curves done with different antennas and configurations. At low frequencies (50-125 MHz) the data are fairly well behaved. In this range the aperture is electrically small. Thus considering the boresight location of the receiving antennas eq. (6) indicates that we are primarily looking at inductive shielding IL_H (assuming that the receiving antenna is in the aperture far field). The data tend to follow the basic behavior predicted by (18). If we ignore the plastic layers which provide little shielding and consider only the aluminum layer which is electrically thin at these frequencies, use an equivalent aperture radius of 0.267 m, let σd = 0.128, and assume that the contact resistance in (18) is zero, then the solid curve up to 125 MHz results. The σd value is based on measurements in the flanged coaxial transmission line holder to be discussed in Section 5. Above 125 MHz the aperture is no longer electrically small. The data in figure 5 actually match theory fairly well. The discrepancy is probably due to the receiving antennas being in the aperture near field (48 cm at 100 MHz) as well as responding to more than one field component. Above 150 MHz we begin to see the effect of multimoding in the chamber which causes the incident field to vary significantly and thus the IL data. As the frequency continues to increase the data variations actually tend to narrow somewhat. This is likely due to two factors: first, the number of modes present is quite large which produces something of an averaging effect, and second, the aperture is quite large at these frequencies and therefore not as dependent on any single field component for coupling. Again this latter factor serves to average the exciting field.

Although shielded rooms are widely available, the difficulties with this approach make it unattractive. The method is time consuming and the incident field is not well controlled, thus, data are difficult to interpret.

4. ASTM PROPOSED CIRCULAR COAXIAL TRANSMISSION LINE HOLDER

4.1 Test Configuration

One of the important questions concerning a shield material is how well it shields an incident TEM wave. TEM waves will result from any source which is located in the far field. A basic requirement in SE testing is to isolate the source and receiving antennas. Since true far field testing using an infinite sheet of the sample is impossible, alternate methods are

necessary. One practical approach is to use a waveguide to excite and receive the fields. This results in a simple, well isolated system. If the waveguide is to simulate a free-space plane wave, then one that supports a TEM mode is the logical choice. This in turn suggests the use of a two-conductor transmission line. These considerations have led to the development of coaxial transmission-line holders for simulating far-field SE testing.

The most commonly used coaxial holder in use at present is that proposed by ASTM Committee D-9.12.14 as one of the Emergency Standards (ES 7-83) [26], [27]. As shown in figure 6, it consists of a section of expanded 50-ohm line which tapers at each end to mate with ordinary 50-ohm coaxial line. The central section has inner and outer dimensions of 4.35 and 9.90 cm respectively. The holder may be disassembled to allow the insertion of an annular (washer shaped) sample sample. When assembled both the inner and outer conductors ideally form continuous connections. The dominant TEM mode has no low frequency cutoff, thus the low frequency limit is determined by equipment. The high frequency limit is approximately 1 GHz and is due to the appearance of resonances associated with the higher-order modes. The dynamic range of this fixture is on the order of 90-100 decibels. The ASTM recommended holder is quite easy to use and lends itself well to an automated system, such as the present NBS bench shown in figure 7. The computer controlled system uses a spectrum analyzer to measure incident, reflected, and through powers at frequencies from 1 MHz to 1 GHz. A typical data set (40 frequencies) takes about 15 minutes to obtain.

4.2 Analytical Background

A coaxial line such as the ASTM proposed holder may be analyzed as a length of transmission line with the sample representing a loaded section, as depicted in figure 8a. The analysis is given in Appendix A with the result that under ideal conditions IL should behave according to eq. (A-20)

$$IL = 10 \log\left|1 + \frac{P_{refl}}{P_t} + \frac{P_{abs}}{P_t}\right| , \tag{22}$$

where P_{refl} and P_{abs} represent the reflected and absorbed powers and P_t is the power delivered to the end termination in the loaded case. Several special cases are also detailed in Appendix A. These are; (1) no sample present, (2) the sample is a pure dielectric ($\sigma = 0$), and (3) the sample is a very good conductor ($\sigma/\omega\varepsilon_0 >> \varepsilon_r$). We find for the latter case that, if the conductor is also thin compared to its skin depth, then IL behaves like

$$IL = 20 \log\left|1 + \frac{1}{2}\eta_0 \sigma d\right| . \tag{23}$$

Equation (23) is frequency independent and simply gives the insertion loss due to reflection alone, or alternately put, the impedance mismatch in the line.

A general analysis such as this is typically not used to describe coaxial holders. Rather, most recognize that the coaxial line approach is primarily a low frequency device and it is adequate to model the line as simple circuit as shown in figure 9. We then find that the insertion loss should behave according to (A-36), or

$$IL = 20 \log\left|1 + \frac{Z_0}{2Z_L}\right| , \tag{24}$$

where Z_0 is the characteristic impedance of the line (50 ohms) and Z_L is the impedance presented by the load. This is the result typically sighted by users and manufacturers [27]. In the ideal case (a perfect conductor) the sample would present a short across the line and $Z_L \to 0$ causing an infinite insertion-loss value. If we recognize that the impedance ratio Z_0/Z_L for an electrically thin load should duplicate that of an infinite sheet in free space, then (17) implies that $Z_L = 1/\sigma d$ while $Z_0 = \eta_0$ (intrinsic free-space impedance) and (24) reduces to (23). If we no longer require that the slab be thin then

$$Z_L/Z_0 = \eta/(\eta_0 \sinh \gamma d) , \tag{25}$$

where η and γ are the sample's intrinsic impedance and propagation constant as previously defined.

So far we have assumed that there is no problem insuring good contact between the sample and the coaxial line conductors. Realistically though, a significant contact impedance may be present. Consider the circuit model shown in figure 9. If we now have some contact impedance Z_C then it would appear in series with the load impedance of the sample, i.e.

$$Z_L \rightarrow Z_L + Z_C \ . \tag{26}$$

Under these conditions eq. (24) becomes

$$IL = 20 \log\left|1 + \frac{Z_0}{2(Z_L + Z_C)}\right| \ . \tag{27}$$

This expression indicates that contact impedance degrades insertion-loss measurements as is the case with a loaded aperture (18). If the sample is a dielectric then Z_C may not contribute that much since Z_L is already very large. However if the sample is a good conductor, as in most shield tests, then the effect of Z_C can be significant. In the limit as $Z_L \rightarrow 0$ (perfect conductor), we see that we are in fact measuring the insertion loss due to Z_C alone.

4.3 Data and Discussion

Figures 10 through 13 show the IL data for our basic sample set as measured in the ASTM version coaxial holder, as well as data from the flanged coaxial holder to be discussed in the next section. The gold-Mylar data (fig. 10) show four IL curves; two separate measurements with the annular sample inserted directly into the holder, and two curves involving the silver painting of the sample, either before or after insertion. Apparently, simply placing the sample in the coaxial holder yields little insertion loss. This may be directly attributed to contact resistance between the sample and the conductors. The gold layer has a quoted σd equal to 0.1 S [27]. Thus based on (23), if we ignore the Mylar which is radiation transparent, the gold-Mylar sample (which is electrically thin) should yield a flat 26 decibels of IL over this frequency range. As may be seen direct insertion results in data well below this expected level, nor is the curve well behaved. Users of this particular fixture have recognized that contact resistance degrades data, thus the use of silver paint where contact is desired is often recommended. However, silver paint can vary in conductivity depending on type and age and one must deal with how much to use and when. The two silver paint curves, before and after insertion, show marked differences. It certainly appears that painting the sample in place gives the highest IL level, but this may be due to excess silver paint deposited on the sample when trying to paint in the confined area of the fixture. In neither case does painting result in a flat curve, suggesting that the presence of the paint introduces a major discontinuity into the line. As silver paint per se is not under test here this is an undesirable effect.

Consider next, the aluminum-Mylar sample data shown in figure 11. The conductivity and thickness of the aluminum layer are comparable to the above gold-Mylar material, thus, we expect IL data on the order of 20-30 decibels. Again silver painting improves results, but both curves fall short of the predicted range. Neither is flat as would be expected for an electrically thin sample. Figure 12 shows the plastic-aluminum-plastic data. Here we no longer have a conductive surface on either side. As expected the direct insertion data are poor despite the aluminum layer between the plastics. Based on the aluminum layer alone, we again expect 20-30 decibels of IL. The unpainted IL measurements are for the most part less than 10 decibels, well away from this range. Silver painting before insertion does help since some contact between the exposed aluminum layer and the test fixture conductors is established, but data are still significantly degraded.

Fluctuations are even worse for the graphite composite sample, shown in figure 13, although the relative IL level measured is higher. Silver painting improves IL but results are not repeatable. For example, the four unpainted IL data curves differ by up to 10 decibels, while painting before insertion still results in variations of approximately 8 decibels.

The conclusion one draws from these data is that contact resistance is a major influence when using the ASTM proposed coaxial holder. Silver painting improves IL but the results tend to be short of expected behavior, messy, and often difficult to repeat. The use of silver paint also slows measurement time since the fixture must be carefully cleaned after each use to rid it of unwanted residues. Nonetheless, the coaxial holder approach remains attractive because of its simplicity and ability to model a far-field SE test. The flanged coaxial holder considered in the next section is an attempt to retain these advantages while better controlling the effects of poor, or variable contact.

5. FLANGED CIRCULAR COAXIAL TRANSMISSION LINE HOLDER

5.1 Test Configuration

An alternative to the ASTM type coaxial holder is a flanged version developed at NBS. This holder uses flanges, rather than continuous conductors, both to secure the sample and to capacitively couple the connectors, as shown in figure 14. The inner conductor has diameter 3.2 cm, while the outer flange has inner and outer diameter dimensions of 7.6 and 13.3 cm respectively. The sample shape is no longer annular as was the case with the ASTM holder. Instead, two pieces of material are needed. The loaded case measurement requires a disk shaped sample with a radius equal to that of the outer flange dimension, (13.3 cm). The unloaded reference measurement is done with an annular shaped piece of material matching the outer flange dimensions (7.6 cm < radius < 13.3 cm), and a disk matching the radius of the inner conductor. This allows us to repeat the capacitive coupling of the loaded case when establishing the reference level, while leaving the space between the two conductors free (unloaded). Clearly, a significant perturbation is introduced into the line, and the analysis of the flanged line, as presented in Appendix B, is more complicated. Nylon screws are used to fasten the flanges together. Metal screws tend to put the contact impedance in series with the test sample as in the ASTM version. Using nylon screws places at least some of the contact impedance perturbation is placed in parallel with the sample [28]. The frequency range is equivalent to that of the ASTM holder, 1 MHz to 1 GHz, with the lower end equipment limited and the upper end determined by the appearance of resonances. The dynamic range is also similar, 90-100 decibels. The automated system used to drive the flanged fixture is the same as that for the ASTM case, thus, the block diagram of figure 7 again applies.

5.2 Analytic Background

The circuit diagram used to model the flanged coaxial holder is shown in figure 15. We expect contact resistance between the flanges and the test material as with the ASTM holder which accounts for R_A, R_B, R_E, and R_F. In addition we now have capacitive coupling between the the flanges themselves (Z_A,Z_B,Z_E,Z_F) as well as capacitive coupling between the flanges and the sample (Z_C,Z_D). Appendix B analyzes this circuit based on Kirchhoff's voltage law with the result that insertion loss behaves according to (B-9), or

$$IL = 20 \log\left|1 + \frac{A'C'}{B(A' + C')}\right| , \tag{28}$$

where A', B, and C', defined by (B-3) and (B-4), are involved combinations of the various impedances and resistances. If we assume that the capacitive coupling is effective as should be the case at higher frequencies (i.e. Z_A,Z_B,Z_E,Z_F are negligible), then these reduce to (B-11) or

$$A' = C' = Z_0$$

$$B = Z_L + \frac{R_A R_B Z_C}{R_A R_B + Z_C(R_A + R_B)} + \frac{R_E R_F Z_D}{R_E R_F + Z_D(R_E + R_F)} . \tag{29}$$

Thus IL (28) becomes

$$IL = 20 \log\left|1 + \frac{Z_0}{2B}\right| . \tag{30}$$

Equation (30) indicates that B must equal the sample load impedance Z_L in order to approach an ideal insertion loss measurement as given by (24). Based on (29) this requires only that we have good conductivity on one side of the material, that is $R_A = R_E = 0$ or $R_B = R_F = 0$. Therefore our two reference samples, gold and aluminum on Mylar, should perform well in the flanged holder assuming that oxidation does not prevent good contact on the metal side. Alternately, if capacitive coupling to the material is sufficient to excite currents through the sample, that is $Z_C \approx 0 \approx Z_D$ then (30) reduces to (24).

5.3 Data and Discussion

Insertion-loss data for our basic samples appear in figures 10-12, and 16. In three cases (gold-Mylar, aluminum-Mylar, plastic-aluminum-plastic) the data are flat and highly repeatable. The gold-Mylar data agree well with the predicted values of 26 decibels. The differences may be attributed to inaccuracy in the quoted $\sigma d = 0.1$ S value or possibly to contact impedance. However, contact impedance is likely not much of a problem or we would expect more fluctuations with frequency. The graphite composite data, shown in figure 16, are not as well behaved. This sample is thicker than the others; thus the capacitances are not as large nor is Z_L as frequency independent. Both metal and nylon screws were used to secure the sample between the flanges. The metal screw measurements show significantly less IL and larger variations. This tends to confirm the use of nylon screws to avoid putting contact resistance in series with the sample. None of the data based on the flanged coaxial holder require the use of silver paint.

A comparison between data from the ASTM and flanged coaxial holders indicates that the flanged holder behaves more like the theoretical model described by eqs. (23) and (24). The IL data from the flanged holder are less degraded and more repeatable. In addition, for electrically thin samples (23) can be used to empirically estimate σd. For example, figures 10 through 12 show that we measure IL levels of approximately 29, 24, and 28 decibels for the gold-Mylar, aluminum-Mylar, and plastic-aluminum-plastic samples respectively. Inverting (23) this yields σd values of 0.144, 0.079, and 0.128 S. These can in turn be used to predict levels for other SE methods as we have already done in analyzing shielded room data.

6. TIME DOMAIN SOURCES

6.1 Test Configuration

Pulse (time domain) sources are of interest in SE measurement because the short duration of the signal allows us to differentiate between direct and indirect (diffracted) paths. The use of efficient FFT algorithms converts time domain data to the frequency domain for comparison to data obtained using CW sources. We will define clean time as the interval between the arrival of the desired direct path signal and the first unwanted indirect path signal. Longer clean time results in data covering a wider frequency range. The present NBS system, shown in figure 17, uses TEM horn antennas spaced 30 cm from the test material with a 350 picosecond pulse as the input. The direct path fields will be approximately plane wave if the antennas are $\lambda/2\pi$ removed from the sample, in this case above 160 MHz. If the antennas are in the aperture near-field it is difficult to predict the incident field type as well as any impedance loading effect the sample may have on the source antenna itself. The high-frequency limit to the present system, 3.5 GHz, is significantly higher than the other methods considered here. The low-frequency limit is determined by the clean time and the $\lambda/2\pi$ far-field condition and at present is approximately 200 MHz. The use of shorter pulses would allow the high-frequency end to be extended. The dynamic range is 50-60 decibels, thus this method may not be applicable to extremely good shield materials. The FFT can convert the time domain signature to the frequency domain very quickly. Thus the time needed to physically mount the sample tends to be the major factor determining measurement time.

Ideally, large sheets will be available for use with this method, as depicted in figure 17. Realistically though, small samples are more likely. Since small samples do not yield sufficient clean time to obtain meaningful data, we must resort to an aperture type measurement. At present NBS has a large copper screen (2.5 m × 2.8 m) with a centrally located circular aperture of diameter 7.6 cm (3"). A 15.2 cm (6") square plexiglass plate is used to press the sample against the aperture and is itself attached to the copper screen using four screws. This configuration yields adequate clean time but introduces the unwanted complication of aperture coupling. At the high frequencies possible with this technique the aperture is large electrically thus a simple analytical solution is not available.

6.2 Analytical Background

Pulse penetration through apertures and slabs has received considerable attention due to the interest in EMP (electromagnetic pulse) shielding. A good review of the problem is given by Karzas and Mo [29]. The problem may be approached as a sequence of transmission functions [30] these being propagation from the antenna to the sample (P_1), transmission through the sample (T), through the aperture (A), and to the receiving antenna (P_2). In the time domain these combine to give the overall attenuation of the system in terms of a convolution integral. However, in the frequency domain convolution is replaced by multiplication. Formally we may represent the power coupled between the source (P_t) and receive (P_r) antennas as

$$P_r/P_t = 20 \log|P_1(k_0l_1)\cdot T(\sigma,k_0d)\cdot A(k_0r)\cdot P_2(k_0l_2)| \ , \tag{31}$$

where l_1 and l_2 are the distances to the source and receive antennas, and we assume a circular aperture of radius r. If no test material is present then $T(\sigma,k_0d)$ is replaced with unity. This representation implies that a large sheet IL measurement should behave according to

$$IL = 20 \log\left|\frac{P_1(k_0l_1)\cdot P_2(k_0l_2)}{P_1(k_0l_1)\cdot T(\sigma,k_0d)\cdot P_2(k_0l_2)}\right| = -20 \log|T(\sigma,k_0d)| \ . \tag{32}$$

For a highly conductive screen excited by a normal plane wave [30]

$$T(\sigma,k_0d) = -j\,\frac{2\eta}{\eta_0}\operatorname{cosec}\frac{\eta_0}{\eta}k_0d = \frac{2\eta}{\eta_0 \sinh\gamma d} \ , \tag{33}$$

where η and γ are defined in (16). If $|\gamma d|$ is small (electrically thin sheet) then (32) reduces to

$$IL = 20 \log\left|\frac{\eta_0 \sinh\gamma d}{2\eta}\right| \approx 20 \log\left|\frac{1}{2}\eta_0\sigma d\right| \ , \tag{34}$$

which agrees with the coaxial holder expression (23) if $\eta_0\sigma d >> 1$. Thus under ideal conditions the large sheet time domain measurements should be similar to those obtained in the coaxial holder and should represent a valid free space shielding simulation.

The addition of an aperture alters the situation only slightly. Referring to (31) we see that the only term affected by loading the aperture is again $T(\sigma,k_0d)$, thus we again have

$$IL = -20 \log|T(\sigma,k_0d)| \ . \tag{35}$$

The difficulty here is that $T(\sigma,k_0d)$ may not be readily known. If the sample is located on the source side, then we essentially have plane wave attenuation preceeding the aperture excitation and (33) applies. This ignores the small size of the sample, contact impedances if any, sample resonances and so on. But as a first approximation we should expect a sample mounted on the source side of an aperture to yield IL data similar to that for a large sheet. If the sample is mounted on the receive antenna side, then the aperture fields rather than a plane wave will excite the material. In this case it is difficult to predict $T(\sigma,k_0d)$. Aperture resonances will also cause the impedance of the exciting field to vary and consequently the type of IL data being measured. The above considerations suggest that time domain measurements are better performed with the sample oriented toward the source. Of course at frequencies where the aperture is electrically small (4) applies and more can be said about a receive side IL measurement. However, the present aperture is no longer small above 400 MHz thus (4) is not a great aid in analyzing data.

6.3 Data and Discussion

The time domain technique IL data are shown in figures 18, and 20 through 23 beginning with the aluminum-Mylar sample (fig. 18). This material was measured using all three of the configurations discussed above, namely, a large sheet (* curve) and aperture loading of both the source (+ curve) and receive (o curve) sides. The large sheet curve is basically flat at about 29 decibels from 200-1500 MHz whereupon some undulating begins to occur. The IL measured here is somewhat higher than the 24 decibels found using the flanged coaxial holder (fig. 11). This may be due to either contact impedance degradation of the coaxial holder results or variations in the aluminum layer between the small sample used in the coaxial holder and the large sheet used in the time domain measurement. In either case agreement to within 5 decibels is reasonable in the present context. When the sample is placed on the source antenna side we see some agreement with the large sheet data (< 10 dB) above 1000 MHz with a marked decrease in the IL measured below 1000 MHz. The equivalence of these two measurements was predicted above based on the transmission function argument. The agreement is considered reasonable especially when the possible effects of small sample size are recognized. Below 100 MHz we may be seeing the loss of dynamic range. This can de demonstrated by examining empty aperture coupling relative to direct coupling (no screen) for various sized apertures (1-4 in), as shown in figure 19. Below 1500 MHz the received signal decreases rapidly, as expected from theory [31], [32]. Thus when the sample is introduced and attenuation is increased we likely encounter the noise floor at the lower frequencies. When the loaded signal is subtracted from the unloaded signal, we are in fact just subtracting the noise floor and we will show little IL if the unloaded signal is near the noise floor as may be the case here at the lower frequencies. Returning to figure 18, the third curve shows IL data for the sample on the receive antenna side. Again we see the dynamic range caused roll off below 1000 MHz and in addition relatively large spikes at 1700 MHz, 2250 MHz, and 2700 MHz. These may be due to either aperture resonances or to the sample itself resonating like a patch antenna. If we use $\lambda/2$ as an estimate of the circumferential resonant length then aperture resonances would appear at multiples of 626 MHz while patch resonances based on a $\lambda/2$ side length would appear at multiples of 984 MHz. The curve here does show a spacing of about 500 MHz between local maxima once sufficient dynamic range is achieved. Thus, it is reasonable to believe that aperture resonances are the primary cause of the beating behavior observed. Regardless, these curves together indicate that mounting the sample on the source antenna side is likely to yield more meaningful results.

Figure 20 presents the source side aperture IL data for the gold-Mylar sample. Again we see the low frequency roll off. The two peaks near 2000 MHz and 2900 MHz conform somewhat to the peaks of the aluminum-Mylar sample measured either as a large sheet or over an aperture with the sample on the source side. This would indicate that the effect is independent of both the aperture and the sample sample size. Thus we are likely observing a nonlinearity in the source signal itself.

Figure 21 gives the plastic-aluminum-plastic material IL data both for a large sheet (* curve) and a source side aperture (+ curve) measurement. Here the data agree very well above 1000 MHz tracking at about 31 decibels. This again is a higher IL level than obtained in the coaxial holder (28 dB, fig. 12) but not significantly. Measurements on the graphite composite material and two magnetic materials appear in figures 22 and 23. The graphite composite data are by no means smooth with distinct spikes at 1800 MHz and 2900 MHz. These align somewhat with the signal variations discussed above but are significantly more pronounced. Above 1000 MHz the graphite composite IL is 30-50 decibels. This is lower than the 55-80 decibels measured in the flanged holder and the difference is probably due to pushing the dynamic range of the system.

The two magnetic materials considered were a conductive, ferrite loaded material (* curve) and a second "high" permeability material referred to as the dark (color) magnetic material (o curve). The ferrite loaded sample yielded high levels of IL while the "high" permeability material was essentially transparent. This shows that the measurement is indeed a far-field one where conductivity is needed to provide shielding as opposed to a near-field low-impedance case. The ferrite loaded material, as did the graphite composite, yields high levels of IL and the data are not smooth and exhibit spikes at about 1600 MHz and 2600 MHz. These are likely due to variations in the signal strength and in both cases we are pushing the dynamic range of the system which is likely to be no better than 40-50 decibels with the aperture screen in place. An attempt was also made to measure the ferrite loaded material in the flanged holder but the dynamic range there was also inadequate.

The time-domain approach is fast, yields relatively high frequency data, and is compatible with other plane wave simulation techniques, especially when a large sheet of the sample is available. Aperture coupling using small samples appears to give reasonable results above 1000 MHz, but is not as well behaved. Unfortunately, some components of the present system are in the developmental stage. Thus, this method is not well suited for widespread use in the near future.

7. DUAL TEM CELL

7.1 Test Configuration

A TEM cell is a section of expanded 50 ohm rectangular coaxial transmission line (RCTL) tapered at each end to match ordinary 50 ohm coaxial line [33]. It is very similar to the coaxial holders discussed in Sections 4 and 5 with the difference that the cross section is now rectangular rather than circular. Clearly, the TEM cell could be used in a similar manner [34], however, no real advantage results. Instead, consider coupling two transmission lines via an aperture in a shared wall. Simple geometry indicates that rectangular cross sections are best suited to this purpose, thus we arrive at the dual TEM cell (DTC) concept [35]-[37] depicted in figure 24. The aperture transfers power from the driving cell (shown as the upper cell fed at Port 1) to the receiving cell (shown as the lower cell). The DTC is unique in that it has two output signals for a given input signal (Ports 2 and 3). Methods discussed in previous sections rely on a single receiver. As shall be seen, the aperture couples energy to the two output ports asymmetrically. This property allows us to examine individually the couplings of the normal electric and tangential magnetic field components. Thus, the DTC simulates both high- (IL_E), and low-impedance (IL_H) near-field shielding simultaneously.

The NBS DTC features identical cells. Figure 25 shows the cross section of the individual TEM cells. They are of dimensions a = 9 cm, b = 6 cm, and g = 2.2 cm. The aperture is a 5.08 cm square. The frequency range is equipment limited at the low end (1 MHz for our present system) and resonance limited at the upper end (1 GHz for the above cells). The sample is excited by the TEM mode propagating in the source cell, thus with respect to the aperture, the incident field simulates a grazing plane wave. The dynamic range is 50-60 decibels. The DTC fixture is readily automated. A sweep from 1 MHz to 1 GHz requires approximately 30 minutes. The fields are contained in the waveguides therefore input power requirements are low and the fixture itself should not be an EMI problem to others. The main difficulty is in mounting the material so that contact impedances are minimized, and ground loops or leakage are avoided. The present system uses RFI gasketing around the aperture to seal both the cells and the sample. Additional pressure is provided by a large weight (23 kg) atop the fixture. As might be expected, this mounting system does not always yield repeatable results, particularly where insulating surfaces are involved.

7.2 Analytical Background

The DTC has been analyzed previously [37] and the details are very similar to those for the apertured TEM cell to be discussed in Section 8. Thus we need only quote the necessary results. Referring to the axes shown in figure 25, we will assume that the aperture is centrally located (x = 0) and parallel to the inner conductor (y = ±b). The excitation coefficients $a^{\pm}$ for the TEM mode, propagating away from the aperture in the forward (+) and backward (-) directions, are given by [37, eq. 12], or eq. (47) (with $F_x = F_y = 1$ for a symmetric coupler) as

$$a^{\pm} = j\frac{k_0}{2\eta_0}\{\alpha_{ey} \pm \alpha_{mx}\}E_{0y}^2(\bar{0}) \ . \tag{36}$$

The aperture polarizabilities (α_{ey}, α_{mx}) are as in Section 2, and $E_{0y}(\bar{0})$ is the TEM mode vertical electric field at the aperture location. Equation (36) requires that the TEM mode field components be properly normalized [15] and an expression for $E_{0y}(x,y)$ (eq. 55) appears in the next section. As mentioned, the ± between terms in brackets implies asymmetric coupling to the two receiving ports.

Referring to (36) above we see that both electric and magnetic fields excite the aperture, similar to a grazing plane wave (10). This is in contrast to a plane wave normally

incident on an aperture (9) in which case only the tangential magnetic field couples. Thus monitoring the forward (a^+) port, where α_{ey} and α_{mx} in eq. (36) add destructively, yields a worst case plane wave IL measurement. Similar to the black screen shielded room case, at low frequencies we may have $|\alpha'_{ey}| << |\alpha'_{mx}|$ and $|\alpha_{ey} + \alpha_{mx}| < |\alpha'_{mx}|$ leading to a negative insertion loss reading at the forward port. This has been observed in practice [37]. Direct IL measurements at the output ports of the DTC have been reported by Faught et al. [36].

An alternate use of the DTC is to sum and difference the two outputs. Based on (36) this yields

$$a(\Sigma) = a^+ + a^- = j\frac{k_0}{\eta_0}\alpha_{ey}E_{0y}^2(\bar{0})$$

$$a(\Delta) = a^+ - a^- = j\frac{k_0}{\eta_0}\alpha_{mx}E_{0y}^2(\bar{0}) \quad . \tag{37}$$

In practice the two output signals are mixed in a hybrid junction to produce the sum $a(\Sigma)$ and difference $a(\Delta)$ signals. If these expressions are to be useful, the lines leading to the hybrid junction should have equal phase and attenuation accumulation. Equation (37) indicates that the sum signal depends on the normal electric field coupling while the difference signal depends on the tangential magnetic field coupling. This approach is equivalent to methods for determining the unknown dipole moments of a radiator placed in a TEM cell [38] or the unknown polarizabilities of gaskets and joints placed in a DTC [35]. Insertion loss data based on the sum and difference signals will yield

$$IL(\Sigma) = 20\log\left|\frac{\alpha_{ey}}{\alpha'_{ey}}\right| = IL_E$$

$$IL(\Delta) = 20\log\left|\frac{\alpha_{mx}}{\alpha'_{mx}}\right| = IL_H \quad . \tag{38}$$

Thus under ideal conditions, the DTC should give a measure of a material's near-field aperture-shielding performance.

7.3 Data and Discussion

The characteristics of empty DTC coupling and single port IL measurements on the plastic-aluminum-plastic sample have been reported previously [37], and data support the above equations. Figures 26 through 30 show the IL data for our present samples, beginning with the gold-Mylar sample (figure 26). The three IL curves plotted are the sum power $IL(\Sigma)$ ($=IL_E$), the difference power $IL(\Delta)$ ($=IL_H$), and a theoretical IL_H curve based on (18) with $\sigma d = 0.144$ empirically determined via (23) using the flanged coaxial holder results. We see first that $IL(\Sigma) > IL(\Delta)$ as expected for a good conductor and that $IL(\Delta)$ agrees very well with the theoretical curve. The sharp spike which appears in both of the measured curves at around 760 MHz is due to a resonance in the TEM cell. It is interesting to note the relative variability of the sum curve as opposed to the smooth difference curve. This is partially due to the dynamic range of the system since the E-field shielding tends to be larger.

Figures 27 and 28 show the data for the aluminum-Mylar and plastic-aluminum-plastic samples. We again find good agreement with theory and that $IL(\Sigma) > IL(\Delta)$. For these three electrically thin materials the $IL(\Sigma)$ and $IL(\Delta)$ curves tend to converge. Unfortunately TEM cell resonances interrupt this trend, yet, extrapolating it appears that these near-field simulation curves seek a level just below that measured in the flanged coaxial holder, a far-field simulation technique. Since there is little absorption in these three samples these curves are giving a measure of the ability of the material to reflect high-impedance, low-impedance, and plane wave type fields.

Both the graphite composite and the ferrite loaded magnetic material provided shielding which exceeded the present dynamic range of the system. By contrast the dark magnetic material, figure 29, shows little attenuation.

It appears from the above data that the DTC can well simulate a near-field aperture coupling measurement. Some thought must be given as to how to relate DTC data to a specific shielding problem since an aperture is likely to no longer be present. However, DTC data should provide a good starting point toward predicting an sample's near-field shielding capability.

8. APERTURED TEM CELL IN A REVERBERATION CHAMBER

8.1 Test Configuration

An alternative to using a TEM cell to drive a second TEM cell via aperture coupling, as is the case with the DTC, is to employ a reverberation chamber as the field source. In essence, the advantages of the DTC are retained, namely, the system is rf tight, and we can consider electric and magnetic field couplings separately. The major difference is that we now have a statistically well behaved field driving the sensing cell. A reverberation chamber begins as a simple shielded room with one significant modification. A paddle is added which may be turned continuously (mode stir) or in small discrete steps (mode tune). The paddle presence allows us to take advantage of the basic shielded room drawback discussed in section 3, namely, multimoding. In any given paddle position we simply have a shielded room with an added boundary condition. As the paddle positioning is varied, the field at any point away from the chamber walls yields a wave impedance whose average approaches the free space value η_0 [39]. Thus in a statistical sense the reverberation chamber may be used to generate a far-field like incident field. Proper average field convergence depends on exciting a large number of modes in the chamber. Thus this technique, at least from the source point of view, works best at higher frequencies. The present NBS chamber is 2.74 m by 3.05 m by 4.57 m and is used above 200 MHz into the GHz range. The TEM cell used as the receiver in the present study is half the DTC discussed in Section 7 with the same square aperture. The statistical field distribution is a good test since real world shields will no doubt encounter a range of incident field types. Unwanted scattering near the sample, due to mounting hardware for example, is not overly important since the reverberation chamber strives for a complicated boundary condition environment anyway. The dynamic range, 90-100 decibels, is quite good. The chamber is a high Q cavity, thus high field levels can be generated using only moderate input power. The primary difficulties are that the chamber will not give meaningful results if too few modes are present (in this case below 200 MHz), and that the technique can be very time consuming. Each frequency tested here requires measurements at 200 paddle positions. Although the operation may be automated and computer controlled, a typical curve presented here takes up to four hours to generate. At higher frequencies (above 1 GHz) where the mode stir technique is applicable and less input-output power normalization is required the measurement time is considerably less. Nonetheless, this method is very data intensive and likely to remain so.

8.2 Analytical Background

The analysis of an apertured TEM cell in a reverberation chamber is similar to that for the DTC except that the source field is distinctly different. Another consideration is the lack of symmetry about the aperture. An apertured coaxial transmission line is similar to half a DTC as depicted in the upper half of figure 24. For the moment we will allow the cross section of the transmission line to be arbitrary, not just rectangular. A set of local coordinates (x', y', z') will be centered at the aperture with x'-z' in the plane of the aperture, z' in the direction of propogation in the coaxial line, and y' the aperture normal. With respect to the aperture plane, small aperture theory predicts that coupling will primarily result from the presence of a normal electric field component ($E_{y'}$) and a tangential magnetic field component ($H_{x'}$). The induced aperture fields will then excite modes in the coaxial transmission line both in the forward (+z'), and backward (-z') directions. At frequencies below the cutoff of the first higher order mode only the TEM mode delivers significant power to the output ports. For an electrically small aperture the excitation should behave as if due to a pair of dipole moments $\bar{P}$ (electric) and $\bar{M}$ (magnetic). Denoting the excitation coefficients $a^{\pm}$, one finds that [15]

$$a^{\pm} = \frac{j\omega}{2}\{\mu_0 \bar{H}_0^{\mp}\cdot\bar{M} - \bar{E}_0^{\mp}\cdot\bar{P}\} \ , \tag{39}$$

where $\bar{E}_0^{\pm}$, $\bar{H}_0^{\pm}$ describe the TEM mode in the transmission line.

The dipole moments depend on the generator field $\bar{E}_g$, $\bar{H}_g$ exciting the aperture as well as the aperture characteristics themselves (size, shape, loading, etc.). Thus the dipole moments are normally expressed as the product of the incident field at the dipole location and an aperture polarizability dyadic. The polarizabilities are usually derived for the case of an aperture located in an infinite ground plane subject to a static impressed field. However, as is pointed out by Collin [40], in the case of coupling between dissimilar regions the geometry can significantly affect the dipole moments. Clearly, the reverberation chamber and a coaxial line will not be symmetric about the aperture, thus Collin's correction may be important. He proposes that the dipole moments be written

$$\begin{aligned} \bar{P} &= \bar{\mp}\, \epsilon_0 \bar{\bar{\alpha}}_e \cdot (\bar{E}_g + \bar{E}_{1sr} + \bar{E}_{2sr}) \\ \bar{M} &= \bar{\mp}\, \bar{\bar{\alpha}}_m \cdot (\bar{H}_g + \bar{H}_{1sr} + \bar{H}_{2sr}) \ , \end{aligned} \tag{40}$$

where $\bar{E}_{1sr}$, $\bar{H}_{1sr}$ represent the scattered field in region (1) which we will take to be the source region (reverberation chamber), $\bar{E}_{2sr}$, $\bar{H}_{2sr}$ represent the scattered field in the receiving region (TEM cell), and the $\bar{\bar{\alpha}}_e$, $\bar{\bar{\alpha}}_m$ are the standard, ideal, infinite ground plane, static polarizabilities described in Section 2. The $\bar{\mp}$ indicates coupling either to the source region (+) or the receiving (-) region. The inclusion of the reaction fields serves the dual purpose of accounting for the dissimilar regions coupled by the aperture and also enforcing power conservation [40]. If the reaction fields are dropped, then eq. (40) reduces to the standard expressions [15].

If we take the transmission line exterior (the reverberation chamber) to be free space for simplicity, then the reaction fields are found to be [40]

$$\begin{aligned} \bar{E}_{1sr} &= -j\frac{k_0^3}{3\pi\epsilon_0}\bar{P} \\ \bar{H}_{1sr} &= -j\frac{k_0^3}{3\pi}\bar{M} \ , \end{aligned} \tag{41}$$

while in the coaxial line we find that

$$\begin{aligned} \bar{E}_{2sr} &= -\bar{a}_y\, j\frac{\omega}{2}E_{0y}^2(\bar{0})P_y \\ \bar{H}_{2sr} &= -\bar{a}_x\, j\frac{k_0}{2\eta_0}E_{0y}^2(\bar{0})M_x \ , \end{aligned} \tag{42}$$

where $(\bar{0})$ denotes the location of the dipoles. An xyz coordinate system has been assumed in the coaxial line with the z axis lying in the direction of propagation in the coaxial line and centered on the inner conductor (c.f. fig. 25), and the x, y axes are tangent and normal to the aperture respectively.

Consider coupling into the coaxial line due to fields $\bar{E}_g$, $\bar{H}_g$ incident from outside. Substituting (41)-(42) into (40) yields the expressions satisfied by the dipole moments, namely

$$-P_y = \varepsilon_0 \alpha_{ey} \{E_{gy'}(\bar{0}') - j\frac{k_0^3}{3\pi\varepsilon_0} P_y - j\tfrac{\omega}{2} E_{0y}^2(\bar{0}) P_y\}$$

$$-M_x = \alpha_{mx} \{H_{gx'}(\bar{0}') - j\frac{k_0^3}{3\pi} M_x - j\frac{k_0}{2\eta_0} E_{0y}^2(\bar{0}) M_x\} \ . \tag{43}$$

Solving for P_y and M_x we find

$$P_y = -\varepsilon_0 \alpha_{ey} E_{gy'}(\bar{0}') \{1 - jk_0^3 \alpha_{ey} [\frac{1}{3\pi} + \frac{1}{2\eta_0} (\frac{E_{0y}}{k_0})^2]\}^{-1}$$

$$M_x = -\alpha_{mx} H_{gx'}(\bar{0}') \{1 - jk_0^3 \alpha_{mx} [\frac{1}{3\pi} + \frac{1}{2\eta_0} (\frac{E_{0y}}{k_0})^2]\}^{-1} \ . \tag{44}$$

We have assumed that the polarizability dyadics are diagonal ($\alpha_{ey} = \bar{a}_y \cdot \bar{\bar{\alpha}}_e \cdot \bar{a}_y$ etc.). Notice that the terms in parenthesis are dimensionless since the normalized TEM mode component E_{0y} has dimensions $(\text{ohms})^{1/2}/\text{m}$ and the polarizability dyadics α_{ey} and α_{mx} have dimensions m^3. If we denote the terms in parenthesis by F_y and F_x respectively, then we have

$$P_y = \frac{-\varepsilon_0 \alpha_{ey} E_{gy'}(\bar{0}')}{F_y}$$

$$M_x = \frac{-\alpha_{mx} H_{gx'}(\bar{0}')}{F_x} \ . \tag{45}$$

Thus the excitation coefficients in (39) are given by

$$a^{\pm} = \frac{jk_0}{2\eta_0} \{\frac{\alpha_{ey}}{F_y} E_{gy'}(\bar{0}') \mp \frac{\alpha_{mx}}{F_x} \eta_0 H_{gx'}(\bar{0}')\} E_{0y}(\bar{0}) \ . \tag{46}$$

Alternately this may be written

$$a^{\pm} = j\{K_y E_{gy'}(\bar{0}') \pm K_x \eta_0 H_{gx'}(\bar{0}')\} \ , \tag{47}$$

where for convenience we have defined a pair of known quantities

$$K_y = \frac{k_0}{2\eta_0} \frac{\alpha_{ey}}{F_y} E_{0y}(\bar{0})$$

$$K_x = -\frac{k_0}{2\eta_0} \frac{\alpha_{mx}}{F_x} E_{0y}(\bar{0}) \ . \tag{48}$$

The excitation coefficients $a^{\pm}$ are for the TEM mode field components $E_0^{\pm}$, and $H_0^{\pm}$. The voltages excited in the lines are related via

$$V^{\pm} = a^{\pm} A \ , \tag{49}$$

where

$$A = -\int_{P_2}^{P_1} \bar{E}_0^{\pm}(\bar{x})\cdot d\bar{l} \ , \tag{50}$$

with $P_1 \to P_2$ describing an arbitrary path from one conductor to the other. Thus the voltages generated in the forward and backward directions are

$$V^{\pm} = jA\{K_y E_{gy'}(\bar{0}') \pm K_x \eta_0 H_{gx'}(\bar{0}')\} \ . \tag{51}$$

This expression allows us to formulate an equivalent generator circuit which describes the aperture excitation of the coaxial line. Consider the circuit shown in figure 30 which Taylor and Harrison [41] propose for an analogous problem. The voltages appearing at the forward (Z^+) and backward (Z^-) loads will be

$$V^{\pm} = I_g Z_0 \pm V_g \ , \tag{52}$$

where Z_0 is the characteristic impedance of the line at the aperture location. Comparing (51) and (52) we see that

$$\begin{aligned} I_g &= j\frac{A}{Z_0} K_y E_{gy'}(\bar{0}') \\ V_g &= jAK_x \eta_0 H_{gx'}(\bar{0}') \ . \end{aligned} \tag{53}$$

This circuit can now be used to predict the power appearing at the measurement equipment, once the impedances $Z^{\pm}$ have been specified.

We are in fact interested in a rectangular coaxial line although up until this point the analysis has been quite general. In order to apply these equations we need to specify $E_{0y}(\bar{x})$ subject to the proper normalization conditions [15, eq. 48], as well as Z_0. Referring to figure 25, one finds that [37]

$$\begin{aligned} E_{0y}(\bar{x}) &= \text{sign}(y)\,\frac{2}{a} Z_0^{1/2} \sum_{mo=1}^{\infty} \frac{\cosh M[b-y\,\text{sign}(y)]}{\sinh Mb} \cos Mx \sin Ma\, J_0(Mg) \\ Z_0/\eta_0 &= \frac{\pi}{8}\{\ln(\frac{8a}{\pi g}) - \sum_{mo=1}^{\infty} \frac{2}{m}(1 - \coth Mb)\}^{-1} \ , \end{aligned} \tag{54}$$

where the coordinates here are as in figure 25, mo denotes a summation over odd m only, $M=m\pi/2a$, and J_0 is a Bessel function.

At this point we may compare results with Taylor and Harrison [41] who analyze a circular coaxial line. In this case the above expressions would be replaced with the much more familar quantities

$$\begin{aligned} E_{0\rho}(\bar{x}) &= \frac{Z_0^{1/2}}{\rho \ln(b/a)} \\ Z_0/\eta_0 &= \frac{1}{2\pi} \ln(b/a) \ , \end{aligned} \tag{55}$$

where in (55) a and b are the inner and outer radii. Substituting these into (50) and (48) yields

$$A = -\int_a^b \frac{Z_0^{1/2}}{\rho \ln(b/a)}\, d\rho = -Z_0^{1/2}$$

$$K_y = \frac{k_0}{2\eta_0}\frac{\alpha_{ey}}{F_y} E_{0y}(\bar{0}) = \frac{k_0}{2\eta_0}\left(\frac{-P_y}{\varepsilon_0 E_{gy'}(\bar{0}')}\right)\frac{Z_0^{1/2}}{b\ln(b/a)} \tag{56}$$

$$K_x = \frac{-k_0}{2\eta_0}\frac{\alpha_{mx}}{F_x} E_{0y}(\bar{0}) = \frac{-k_0}{2\eta_0}\left(\frac{-M_x}{H_{gx'}(\bar{0}')}\right)\frac{Z_0^{1/2}}{b\ln(b/a)} .$$

Letting the aperture lie on the outside conductor, i.e. $\rho = b$ leads to

$$I_g = \frac{jk_0 P_y}{4\pi\varepsilon_0 b Z_0}$$

$$V_g = -j\frac{k_0 M_x}{4\pi b} . \tag{57}$$

These equations agree with those of Taylor and Harrison [eqs. 34-35] if we absorb a minus sign into the dipole moments ($-P_y \to P_0$, $-M_x \to M_0$) to conform to their notation.

The power delivered to the two end impedances $Z^{\pm}$ is determined by

$$P^{\pm} = \frac{1}{2}\,\mathrm{Re}\{1/Z^{\pm}\}\,|V^{\pm}|^2 . \tag{58}$$

Based on the above model we may now analyze the behavior of the apertured TEM cell. First we will consider such a cell placed in an anechoic chamber. Second, the cell will be placed in a reverberation chamber and IL measurements will be performed on our various material samples.

The anechoic chamber presents a well known environment in which to test the validity of the present analysis. We begin by expanding the output powers $P^{\pm}$ in (58) in terms of K_x, K_y, and the generator fields. This yields

$$P^{\pm} = \frac{1}{2}|A|^2\mathrm{Re}\{1/Z^{\pm}\}\{|K_y|^2|E_{gy'}(\bar{0}')|^2 + |\eta_0 K_x|^2\,|H_{gx'}(\bar{0}')|^2$$

$$\pm 2\mathrm{Re}(E^*_{gy'}(\bar{0}')\eta_0 H_{gx'}(\bar{0}')K_x K_y^*)\} . \tag{59}$$

It remains to specify the generator fields $E_{gy'}(\bar{0}')$ and $H_{gx'}(\bar{0}')$. Typically, the incident field in an anechoic chamber will be a plane wave. In particular, if the cell is oriented such that the aperture plane is aligned with the magnetic field but normal to the electric field, then we have

$$\eta_0 H_{gx'}(\bar{0}') = E_{gy'}(\bar{0}')\cos\theta , \tag{60}$$

where θ is the angle between the x' axis (as defined by the aperture coordinates) and the incident magnetic field. This basic configuration should yield maximal coupling since both the dipole moments will be excited. The angle θ gives a rotation around the y' axis only however. In general, we would also rotate around the x' , and z' axes to explore the three major cuts. In these additional cases the above equation would not apply. Equation (59) should allow us to predict peak power however. The xyz coordinates fixed to the transmission line are independent of any rotatations. Substituting (60) into (59) yields

$$P^{\pm} = \frac{1}{2}|A|^2 \mathrm{Re}\{1/Z^{\pm}\}|E_{gy}(\bar{0})|^2\{|K_y|^2 + |K_x|^2\cos^2\theta \pm 2\mathrm{Re}\{K_y K_x^*\}\cos\theta\}. \quad (61)$$

Notice that (61) implies that the two ends (±) do not receive equal signals as might have been intuitively thought. As is the case with the dual TEM cell the two dipole moments will interfere constructively in one direction and destructively in the other. If a single port is monitored the pattern will not be symmetric as the cell is rotated through 360°. Equation (61) does show that

$$P^+(\theta) = P^-(\theta + \pi) . \quad (62)$$

Thus, the two output ports are related by a 180° rotation, and both the peak and average responses will be independent of which end is monitored as long as the cell is rotated 360°. Therefore we need consider only one port, say P^+. If we expand K_x, and K_y we find

$$P^+(\theta) = K\{|\frac{\alpha_{ey}}{F_y}|^2 + |\frac{\alpha_{mx}}{F_x}|^2\cos^2\theta - 2\mathrm{Re}\{\frac{\alpha_{ey}\alpha_{mx}}{F_y F_x^*}\}\cos\theta\} , \quad (63)$$

where the known terms in front of the parentheses have been collected into a term K,

$$K = \frac{1}{2}|A|^2 \mathrm{Re}\{1/Z^+\}|E_{gy}(\bar{0})|^2|\frac{k_0}{2\eta_0}|^2 E_{0y}(\bar{0})|^2 . \quad (64)$$

At low frequencies the dissimilar region coupling factors F_x and F_y should be close to unity and we can write

$$P^+(\theta) \approx K(\alpha_{ey} - \alpha_{mx}\cos\theta)^2 = K\,\alpha_{ey}^2(1 - \frac{\alpha_{mx}}{\alpha_{ey}}\cos\theta)^2 . \quad (65)$$

For a circular aperture $\alpha_{mx}/\alpha_{ey} = -2$, thus

$$P^+(\theta) = K\,\alpha_{ey}^2(1 + 2\cos\theta)^2 . \quad (66)$$

Based on (66), a plot of $P^+(\theta)$ should behave like figure 31 where the bottom θ scale is for $P^+(\theta)$ while the upper is for $P^-(\theta)$, and both are normalized to $K\alpha_{ey}^2$. This theoretical curve may be compared to anechoic chamber data, shown in figure 32, measured with a small brass TEM cell with a circular aperture at the $P^-(\theta)$ port. This figure shows that the basic behavior is as expected. There are fluctuations, perhaps due to varying amounts of connecter leakage as well as other uncontrolled factors. Also the ideal case predicts that $P^-(180°)/P^-(0°) \approx 9$ while the measured result gives a ratio of approximately 5. However, this is again probably due to the factors mentioned above. Overall though the qualitative agreement in the pattern is good.

Consider next figure 33 which shows the peak power coupled to our square apertured TEM cell in the anechoic chamber, along with the peak and average power measurements for the same cell in a reverberation chamber. The incident field ($E_{gy}(\bar{0}')$) in each case is 70.8 V/m, where in the reverberation chamber this value is deduced from an average received power at a separate receiving antenna. According to (66) the peak should occur at $P^+(0°)$ and at $P^-(180°)$. Thus $P^+_{max} = P^-_{max} \approx K(\alpha_{ey} - \alpha_{mx})^2$. For an RCTL the field distribution is given by (54). If we retain only the first term in the series expansion and note that for this particular cell the aperture is centrally located at $\bar{0} = (0,b)$, then we find

$$A = -\int_0^b E_{0y}(0,y)dy \approx \frac{4}{\pi} Z_0^{1/2}$$

$$E_{0y}(0,b) \approx \frac{2}{a} (Z_0^{1/2})/\sinh\frac{\pi b}{2a} . \tag{67}$$

Inserting E_{0y} (a = 0.09 m, b = 0.06 m) and $E_{gy'}(\bar{0}')$ = 70.8 V/m)into (64) for K, and letting the termination Z^+ be matched (50 ohms) we find that

$$K \approx -14 + 20 \log(f(MHz)) \text{ (dB)} . \tag{68}$$

The square aperture polarizabilities are given by (13) with s = 5.08 cm. Evaluating (66) we find

$$P_{max} \approx -100 + 20\log(f(MHz)) \text{ (dB)} . \tag{69}$$

Numerical results based on (69) are also shown on figure 33. The theoretical curve agrees well with the peak power measurements made in the reverberation chamber and with the two end anechoic chamber data points (500 MHz, 1000 MHz). The 700 MHz anechoic chamber data point deviates significantly, however, this is likely due to measurement errors. Data from other TEM cells taken in the anechoic chamber agree very well with theory.

As with the DTC, the basic advantage to the apertured TEM cell probe in the reverberation chamber is that we can monitor power at both ends, sum and difference the outputs via a hybrid junction, and thereby separate the electric and magnetic field couplings. By doing so we get some measure of the sample's high and low impedance shielding characteristics. We should also note that any apertured waveguide would allow us to apply this basic approach, however coaxial lines are convenient since they couple to standard connectors and 50 ohm lines, and the rectangular geometry allows us to mount flat panel samples to the probe exterior.

Putting the output signals through a mixer allows us to form the sum (Σ) and difference (Δ) voltages. We have

$$V(\Sigma) = V^+ + V^- = 2I_g Z_0 = j2AK_y E_{gy'}(\bar{0}')$$

$$V(\Delta) = V^+ - V^- = 2V_g = j2AK_x \eta_0 H_{gx'}(\bar{0}') . \tag{70}$$

The sum and difference powers will thus be

$$P(\Sigma) = 2Re\{1/Z_\Sigma\}|AK_y E_{gy'}(\bar{0}')|^2$$

$$P(\Delta) = 2Re\{1/Z_\Delta\}|AK_x \eta_0 H_{gx'}(\bar{0}')|^2 . \tag{71}$$

These expressions assume that the voltages $V^\pm$ excited at the aperture are the same as those appearing at the mixer. This should be a reasonable assumption if low loss cables are used and if the cable lengths are kept equal so that no relative phase change or attenuation are introduced.

Typically, two types of power measurement are performed in the reverberation chamber, namely, peak output (max) and average output (< >). For the sum and difference powers these may be denoted

$$P(\Sigma)_{max} = 2Re\{1/Z_\Sigma\}|AK_y|^2|E_{gy'}(\bar{0}')|^2_{max}$$

$$P(\Delta)_{max} = 2Re\{1/Z_\Delta\}|AK_x|^2\eta_0{}^2|H_{gx'}(\bar{0}')|^2_{max} \tag{72}$$

$$\langle P(\Sigma)\rangle = 2\mathrm{Re}\{1/Z_{\Sigma}\}|AK_y|^2\langle|E_{gy'}(\bar{0}')|^2\rangle$$

$$\langle P(\Delta)\rangle = 2\mathrm{Re}\{1/Z_{\Delta}\}|AK_x|^2\eta_0^2\langle|H_{gx'}(\bar{0}')|^2\rangle \ .$$

We can now see that regardless of whether we monitor peak or average power, the insertion loss should behave like

$$\begin{aligned} IL(\Sigma) &= IL_E \\ IL(\Delta) &= IL_H \end{aligned} \qquad (73)$$

assuming that the peak and average driving fields $E_{gy}(\bar{0})$ and $H_{gx}(\bar{0})$ are the same in each case (loaded and unloaded). Actual measurements indicate that IL is reasonably independent of whether the peak or average is monitored. We will typically consider data based on averages, however, peak power data may have an advantage where dynamic range is a problem. Having generated these descriptive equations leading to (73) reminiscent of DTC results we now may consider some IL measurements.

8.3 Data and Discussion

The IL data obtained via the apertured TEM cell in the reverberation chamber is shown in figures 34 through 39. As with the DTC we also show a theoretical IL_H curve based (18) with σ_d empirically determined in the flanged coaxial holder for the gold-Mylar, aluminum-Mylar, and plastic-aluminum-plastic samples. Begin with figure 34 for the gold-Mylar test material. The agreement between IL(Δ) and the theoretically predicted IL_H is not good. By accident, the Mylar side of the material was mated to the receiving cell for the loaded tests; thus the contact impedance was high. Put alternately, a shield should allow the currents excited on the cell exterior to flow over the aperture but in this case they were able to penetrate the cell interior. Figure 35 shows the equivalent aluminum-Mylar data. Here as expected the electric field shielding IL(Σ) is much greater than the magnetic field shielding IL(Δ) at the lower frequencies. In addition the agreement between our theoretical IL_H and IL(Δ) is very good. The plastic-aluminum-plastic sample yields the results shown in figure 36. Again the sum and difference curves behave as expected with good agreement between our theoretical IL_H and IL(Δ). In all of the above curves the TEM cell begins to show resonances above 700 MHz although the IL(Σ) data seem to be more sensitive to their appearance than do the IL(Δ) data, as was the case in the DTC. The multi moding in the reverberation chamber is weak below 200 MHz. Thus our present data have meaning only in this somewhat restricted range.

Before considering other samples let us compare the above apertured TEM cell data to that from the DTC. Because the gold-Mylar sample was mounted on its insulating side there is not much agreement (figs. 26 and 34). The DTC is symmetric about the sample so the side orientation is not important. As may be seen the DTC IL is much higher for both the sum and difference signals. The aluminum-Mylar data (figs. 27 and 35) are almost identical, particularly the IL(Δ) curves. The IL(Σ) data fluctuate but their basic shape is the same. This is also the case for the plastic-aluminum-plastic sample (figs.28 and 36). The theoretical curves based on (18) or (73) are identical.

Figure 37 shows the graphite composite IL data. In general IL(Σ) > IL(Δ) but not to the extent of the previous materials. This material shows significantly higher shielding levels especially at the lower frequencies leading one to suspect that the composite has some magnetic reflecting capability to it. The sample is also significantly thicker than are the others so we may be seeing an appreciable amount of absorption. The IL range found via this technique, 60-80 decibels, is similar to that found in the flanged coaxial holder (fig. 16). Thus the graphite composite material appears to be a very effective near- and far-field shield.

Figure 38 shows IL data for the ferrite loaded magnetic material also measured via the time domain system (fig. 23). This material contains both ferrite and conductive material thus we see high levels of IL at the lower frequencies. In fact the data for both IL(Δ) and

IL(Σ) are of the same order. The IL levels here tend to be lower than with the time domain suggesting that this materials near-field SE capability is not as great as its plane wave SE.

Finally we tested a material which consists of a copper-ferrite-copper layering. Thus we expect that this material should have very good electric and magnetic shielding properties. Figure 39 shows the IL data and we definitely see here IL(Δ) exceeding IL(Σ) although only slightly. This material proved to be an excellent shield and in fact tended to exceed the dynamic range of the system. Thus instead of using averages, peak readings were used to determine the IL since these are more likely to be above the noise floor. Separate measurements have shown that peak and average measurements tend to closely track each other at a difference of about 7-8 decibels [23]. Thus an insertion-loss measurement should be independent of whichever is used since two signals are subtracted. Figure 40 shows both the sum and difference based on both the average and peak power measurements for our plastic-aluminum-plastic sample. As may be seen they track quite well.

9. OTHER METHODS

The SE test methods studied in the preceding sections by no means form an exhaustive list. Other methods often mentioned include measuring transfer impedance measurements [42]-[44], the dual box fixture proposed by the ASTM [26],[27], direct complex permittivity measurements, and rectangular waveguides. In the context of the present study these additional techniques are briefly discussed.

9.1 Surface Transfer Impedance Measurements

A fixture for mesuring surface transfer impedance is pictured in figure 41. The system was originally designed to evaluate the SE of shielded cables and gaskets but may also be used to investigate the SE of a washer shaped sample. The surface transfer impedance Z_{st} is defined as the ratio of the tangential electric field E_t induced on the interior of the shield to the surface current density J excited on the exterior of the shield by external sources [19]

$$Z_{st} = E_t/J \ . \tag{74}$$

Referring to figure 41, the surface transfer impedance may be measured by comparing the voltage V (as shown) across the interior of the sample to the driving current I. The idea is similar to that of the coaxial holders discussed in sections 4 and 5 since conducted currents are used to test SE rather than radiated fields. In fact, the circuit diagram for the transfer impedance fixture is the same as given by figure 9. A difficulty is that we again have contact impedances in series with the load impedance. The fixture does allow for adequate contact to be formed between the sample and the fixture as opposed to the ASTM proposed coaxial holder. Air pressure is used to aid in creating contact. The reported frequency range is from dc to 700 MHz whereupon fixture resonances begin to occur. The dynamic range should approach 100 decibels [42]. It should be possible to automate this system thus measurement time is expected short.

Surface transfer impedance data, either measured or theoretical, can be used to predict SE performance. Birkin et. al. [19] discuss approximations relating Z_{st} to SE for a set of basic geometries, both for low- and high-impedance fields. They find that

$$\begin{aligned} IL_E &\approx 20 \log|Z_E/Z_{st}| \\ IL_H &\approx 20 \log|Z_H/Z_{st}| \ , \end{aligned} \tag{75}$$

where Z_E and Z_H are functions of frequency, and the shield geometry. For example

$$Z_E = [8\pi\varepsilon_0 V/S \ f(Hz)]^{-1} \ , \tag{76}$$

where V/S represents the shields volume to surface ratio. This expression is applicable to spheres, cylinders, parallel plate enclosures, and a single sheets provided that the exciting

field is spatially uniform and produces a uniform interior field. The equivalent Z_H expressions are more complicated

$$Z_H = (V/S)j\omega\mu_0 \quad \text{(sphere, cylinder, parallel plate)}$$
$$Z_H = \omega\mu_0(r_1 + r_2) \quad \text{(flat plate excited by identical coaxial loops)} \tag{77}$$

where in the latter expression r_1 and r_2 are the distances from the loops to the flat sheet, and it is assumed that $(r_1 + r_2) >>$ the loop radius and that $(r_1 + r_2) >> 0.03$.

A second approach to extrapolating surface transfer impedance data to high- and low-impedance field SE is to note that Z_{st} is related to plane wave attenuation via [43]

$$\text{IL (plane wave)} = 20 \log|Z_{st}/50| \ , \tag{78}$$

where we have assumed that the fixture is a 50 ohm measurement system. The insertion loss for elementary sources (dipole and loop) in the near-field of a plane sheet will approach the measured plane wave IL value at a rate of approximately 20 decibels per decade, E-field (dipole) from above and H-field (loop) from below. The curves meet at the near-field, far-field transition point, $\lambda/2\pi$. This projection ignores contact impedances and the effects of finite geometry, but should indicate the basic expected behavior.

9.2 The ASTM Proposed Dual Box

The ASTM has proposed the use of a dual box in order to perform high- impedance and low-impedance IL measurements. The dual box consists of two small metal chambers coupled via a rectangular aperture as shown in figure 42. Each chamber contains an antenna, either a dipole for high-impedance data or small loops for low-impedance data. In essence, however, the dual box is simply a scaled version of the shielded room approach and suffers some of the same problems. By keeping the chambers small, one can avoid multimoding, but specifying the field distribution exciting the sample remains difficult. It may be possible through very rigid standardization of the technique to obtain repeatable data but interpreting results and relating them to other methods is still formidable.

9.3 Complex Permittivity Measurements

If a material's complex permittivity can be measured directly, then one could predict shielding effectiveness under a variety of conditions [6]-[14]. Unfortunately, complex permittivity measurements in the microwave frequency range are problematic [46]. Balanced bridge networks are difficult if not impossible to balance in the case of highly lossy materials and their use is usually limited to below 100 MHz. Open and disk resonators (cf. [46]) extend to much higher frequencies, however, these also tend to be valid only for low loss materials and not the highly conductive composites often of interest here. These measurements will also yield some type of bulk permittivity which may lead to poor SE predictions for non-isotropic and inhomogenous materials. Nonetheless complex permittivity measurements would be valuable when available.

9.4 Rectangular Waveguides

It may be possible to perform IL measurements at microwave frequencies by loading rectangular waveguides operating in the TE_{10} mode, much as is done with the coaxial holders. The sample would have to be cut to fit the guide but this should be no more difficult than with most methods. Various sized waveguides could be used to achieve broad frequency coverage. One advantage to this approach is that contact impedance should not be a problem since we are not trying to create a short across a transmission line. Instead, viewing the IL measurement as a microwave circuit problem, we are measuring the scattering matrix due to introducing the sample. A difficulty is that this method would not simulate any of the standard shield tests; high impedance, low impedance, or plane wave. The TE_{10} mode consists of two magnetic and an electric field components. These cannot be separated thus we are not considering a near-field IL test. The wave impedance is a function of frequency, as opposed to a plane wave or TEM mode, thus these measurements would not readily relate to free space

shielding simulation. If one could determine how to interpret results with respect to our standard SE information needs then this approach might prove to be quite useful.

10. CONCLUSIONS

Six SE measurement approaches have been studied here and experience has been gained as to their relative advantages and disadvantages. The basic characteristics of each method are summarized in Table 1 (see p. 55). In order to well characterize a given piece of shield material both its far- and near-field shielding capability are of interest. Based on Table 1 and the present study the following techniques appear to be the most promising:

Method	Field Type	Frequency
Flanged Coaxial Holder	Far-field	≤ 1 GHz
Time Domain	Far-field	≥ 1 GHz
Dual TEM Cell	Near-field	≤ 1 GHz
Apertured TEM Cell in a Reverberation Chamber	Near-field	≥ 200 MHz ≤ 4 GHz

Using the above four methods a shielding material may be well studied over a broad frequency range. They combine both good system characteristics with good theoretical support which together yield meaningful insertion loss data.

11. ACKNOWLEDGMENTS

The authors are grateful to a number of people who have aided in the preparation of this manuscript. In particular we would like to recognize John Adams, Galen Koepke, Andy Ondrejka, Eric Vanzura, and Myron Crawford for their careful measurements. Reviews by David Hill, Bing H. Liu, Matt Young, and Lorant Muth were much appreciated. Thanks also to C. K. S. Miller for his support of this effort. This study was also partially supported by the U.S. Army Aviation Systems Command.

12. REFERENCES

[1] Miller, M. B. Materials and techniques used in EMI/RFI shielding of plastic chassis for electronic systems. SPE Shielding Plastics Symp. Rec. 1984 June; Chicago, IL. 139-150.

[2] Mooney, P. J. Plastics EMI shielding: the evolving state of the art. EMC Techn. vol. 4: 19-28; 1985 October-December.

[3] Armstrong, H. W. The long term environmental effects upon conductive coatings for plastic enclosures. MIDCON Symp. Rec. 1982 November; Dallas, TX. 28/2/1-5.

[4] May, N. RFI shielding of enclosures. Electronic Engineering. vol. 55: 77-78; 1983 May.

[5] MIL-STD 285 Attenuation measurements for enclosures, electromagnetic shielding, for electronic test purposes, method of. DoD. 1956 June.

[6] Schelkunoff, S. A. Electromagnetic Waves. New York: Van Nostrand; 1943. 305-315.

[7] Cowdell, R. B. New dimensions in shielding. IEEE Trans. Electromagn. Compat. EMC-10(1): 158-167; 1968 March.

[8] Stirrat, W. A. USAECOM contributions to shielding theory. IEEE Trans. Electromagn. Compat. EMC-10(1): 63-66; 1968 March.

[9] Schulz, R. B.; Plantz, V. C.; and Brush, D. R. Low-frequency shielding resonance. IEEE Trans. Electromagn. Compat. EMC-10(1): 7-15; 1968 March.

[10] Babcock, L. F. Computer determination of electromagnetic wave shielding effectiveness. IEEE Trans. Electromagn. Compat. EMC-10(1): 331-334; 1968 March.

[11] Levy, S. Electromagnetic shielding effect of an infinite plane conducting sheet placed between circular coaxial coils. Proc. IRE. vol. 24: 923-941; 1936 June.

[12] Moser, J. R. Low-frequency shielding of a circular loop electromagnetic field source. IEEE Trans. Electromagn. Compat. EMC-9(1): 6-18; 1967 March.

[13] Bannister, P. R. New theoretical expressions for predicting shielding effectiveness for the plane shield case. IEEE Trans. Electromagn. Compat. EMC-10(1): 2-7; 1968 March.

[14] Bannister, P. R. Further notes for predicting shielding effectiveness for the plane shield case. IEEE Trans. Electromagn. Compat. EMC-11(2): 50-53; 1969 May.

[15] Collin, R. E. Field Theory of Guided Waves. New York: McGraw-Hill; 1960. 288-298.

[16] Taylor, C. D. Electromagnetic pulse penetration through small apertures. IEEE Trans. Electromagn. Compat. EMC-15(1): 17-26; 1973 February.

[17] Susskind, C. Obstacle-type artificial dielectrics for microwaves. Jr. Brit. IRE. vol. 12: 49-62; 1952 January.

[18] Casey, K. F. Low-frequency electromagnetic penetration of loaded apertures. IEEE Trans. Electromagn. Compat. EMC-23(4): 367-377; 1981 November.

[19] Birkin, J. A.; Wallenberg, R. F.; and Milton, O. Advanced composite aircraft electromagnetic design and synthesis. IEEE Int. Electromagn. Compat. Symp. Rec. 1981 August; Boulder, CO. 562-569.

[20] Free, W. R. Radiated EMI measurements in shielded enclosures. IEEE Int. Electromagn. Compat. Symp. Rec. 1967 July; Washington, D.C. 43-53.

[21] Mendez, H. A. Shielding theory of enclosures with apertures. IEEE Trans. Electromagn. Compat. EMC-20(2): 296-305; 1978 May.

[22] Bodner, D. G.; Denny, H. W.; and Jenkins, B. Shielding effectiveness measurements on conductive plastics. IEEE Int. Electromagn. Compat. Symp. Rec. 1979 October; San Diego, CA. 27-33.

[23] Crawford, M. L.; and Koepke, G. H. Operational considerations of a reverberation chamber for EMC immunity measurements - some experimental results. IEEE Nat. Electromagn. Compat. Symp. Rec. 1984 April; San Antonio, TX. 47-54.

[24] MIL-STD 1377.

[25] Lee, J. D. MIL-STD-1377 vs. MIL-STD-285 microwave shielding effectiveness measurements. IEEE Int. Electromagn. Compat. Symp. Rec. 1975 October; San Antonio, TX. 4BIf1-f4.

[26] Oberholtzer, L. C.; Mauriello, A. J.; and Stutz, D. E. A treatise on the new ASTM ESI shielding standard. ITEM 1984. 1984. 174-178.

[27] Simon, R. M.; and Stutz, D. Test methods for shielding materials. EMC Techn. vol. 2: (4): 39-48; 1983 October-December.

[28] Week, R. A. Thin-film shielding for microcircuit applications and a useful laboratory tool for plane-wave shielding evaluations. IEEE Trans. Electromagn. Compat. EMC-10(1): 105-112; 1968 March.

[29] Karzas, W. J.; and Mo, T. C. Linear and nonlinear diffusion through a ferromagnetic conducting slab. IEEE Trans. Antennas Propagat. AP-26(1): 118-129; 1978 January.

[30] Franceschetti, G.; and Papas, C. H. Steady state and transient electromagnetic coupling through slabs. IEEE Trans. Antennas Propagat. AP-27(9): 590-596; 1979 September.

[31] Ari, N.; Hansen, D.; and Schar, H. Electromagnetic pulse (EMP) penetration through circular apertures in the frequency domain. Proc. IEEE. 73(2): 368-369; 1985 February.

[32] Cathey, W. T. Approximate expressions for field penetration through circular apertures. IEEE Trans. Electromagn. Compat. EMC-25(3): 339-345; 1983 August.

[33] Crawford, M. L. Generation of standard EM fields using TEM transmission cells. IEEE Trans. Electromagn. Compat. EMC-16(4): 189-195; 1974 November.

[34] Hariya, E.; and Masahiro, U. Instruments for measuring the electromagnetic shielding effectiveness. IEEE Int. Electromagn. Compat. Symp. Rec. 1984 October; Tokyo, Japan. 800-805.

[35] Whitson, A. L.; and Vance, E. F. Bolted lapped-joint EMP shields. Stanford Res. Inst. Int. 1977 June; Menlo Park, CA. DNA 4472-f.

[36] Faught, A. N.; Dowell, J. T.; and Scheps, R. D. Shielding material insertion loss measurement using a dual TEM cell system. IEEE Int. Electromagn. Compat. Symp. Rec. 1983 August; Washington, D. C. 286-290.

[37] Wilson, P. F.; and Ma, M. T. Shielding effectiveness measurements with a dual TEM cell. IEEE Trans. Electromagn. Compat. EMC-27(3): 137-142; 1985 August.

[38] Ma, M. T.; and Koepke, G. H. A method to quantify the radiation characteristics of an unknown interference source. Nat. Bur. Stand. (U.S.) Tech. Note 1059; 1982 October.

[39] Crawford, M. L.; and Koepke, G. H. Design, evaluation, and use of a reverberation chamber for performing electromagnetic susceptibility/vulnerability measurements. Nat. Bur. Stand. (U.S.) Tech. Note to be published; 1986.

[40] Collin, R. E. Small aperture coupling between dissimilar regions. Electromagnetics. vol. 2: 1-24; 1982.

[41] Taylor, C. D.; and Harrison, C. W. On the excitation of a coaxial line by an incident field propagating through a small aperture in a sheath. IEEE Trans Electromagn. Compat. EMC-15(3): 127-131; 1973 August.

[42] Awerkamp, D. R. Shielding effectiveness of filled composites and coated plastics," in IEEE Int. Electromagn. Compat. Symp. Rec. 1981 August; Boulder, CO. 277-280.

[43] Faught, A. N.. An introduction to shield joint evaluation using EMI gasket transfer impedance data. IEEE Int. Electromagn. Compat. Symp. Rec. 1982 September; Santa Clara, CA. 38-44.

[44] Jerse, T. A. Low transfer impedance - a key to effective shielding. RF Design. vol. 7: 29-32; 1984

[45] Birch, J. R.; and Clarke, R. N. Dielectric and optical measurements from 30 Mhz to 1000 GHz. Radio Electron. Eng. vol. 52(11/12): 566-584; 1982 November/December. 1982.

[46] Clarke, R. H.; and Rosenberg, C. B. Fabry-Perot and open resonators at microwave and millimeter wave frequencies,2-300 GHz. J. Phys. E: Sci. Instrum. vol. 15: 9-24; 1982 January.

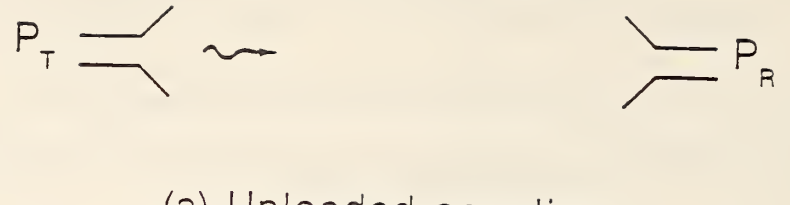

(a) Unloaded coupling.

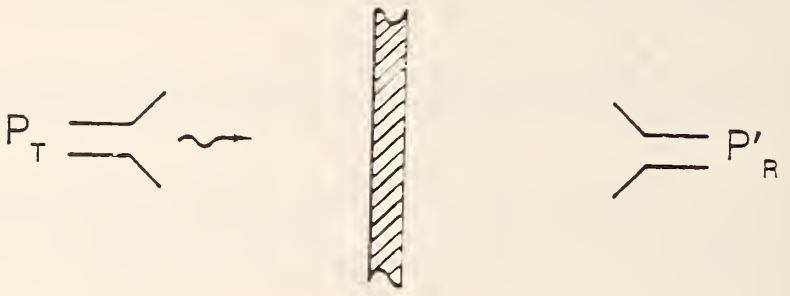

(b) Loaded coupling.

$$IL = 10 \log \left| \frac{P_R}{P'_R} \right| dB$$

Figure 1. A typical arrangement for measuring the shielding effectiveness of a material.

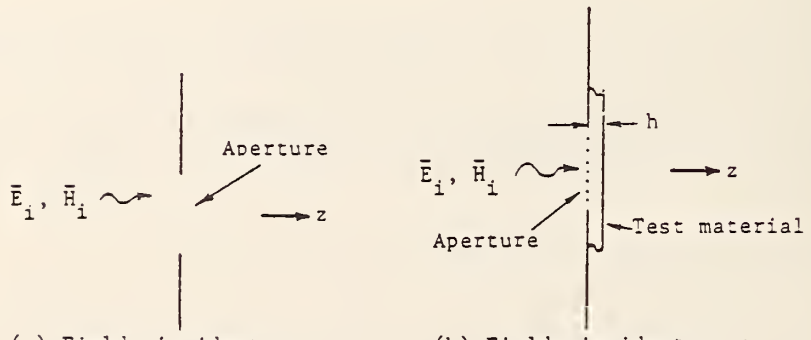

(a) Fields incident on an empty aperture

(b) Fields incident on a loaded aperture

Figure 2. An aperture shielding effectiveness measurement.

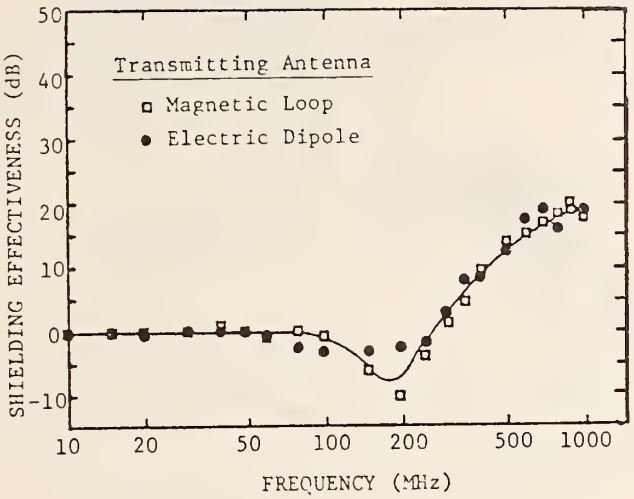

Figure 3. Shielding effectiveness of inject molded panel.

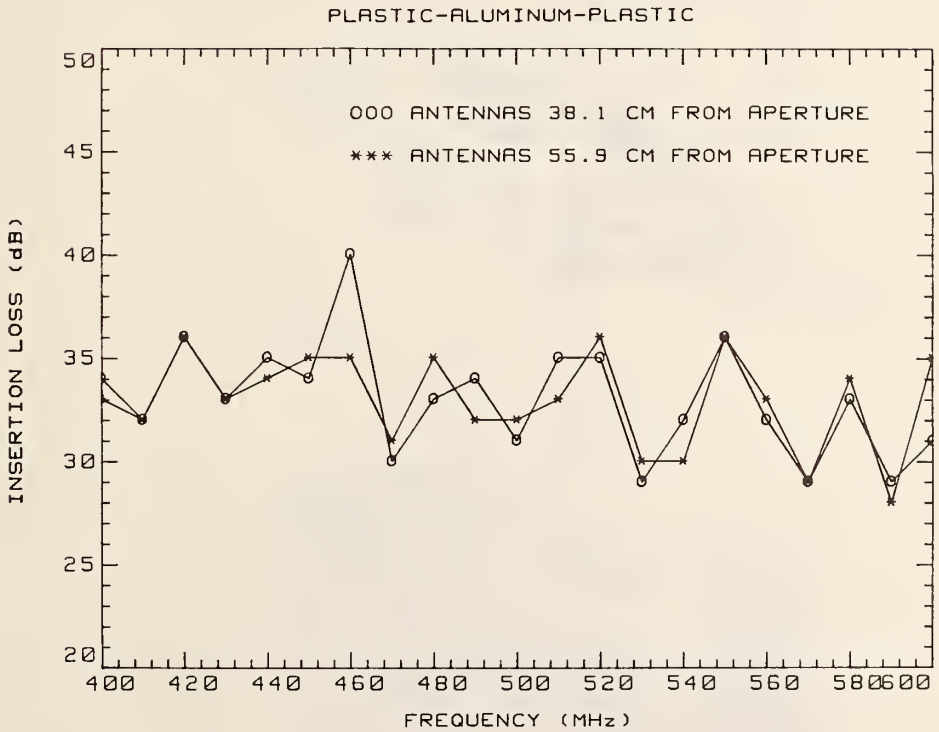

Figure 4. Shielded room IL measurements on the plastic-aluminum-plastic sample.

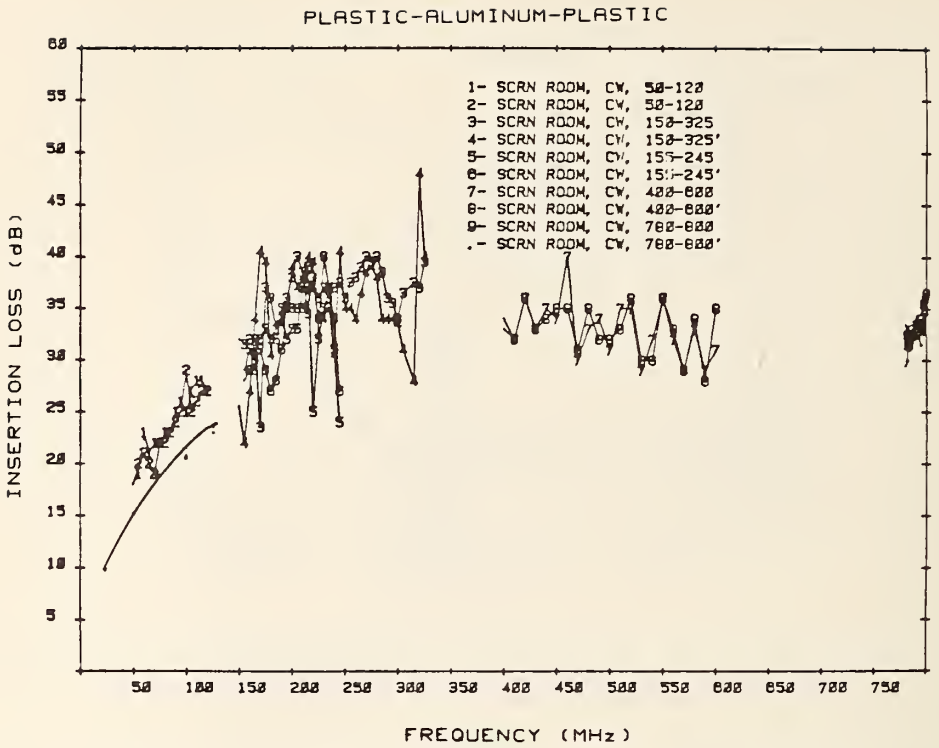

Figure 5. Shielded room IL measurements on the plastic-aluminum-plastic sample, multiple antenna locations.

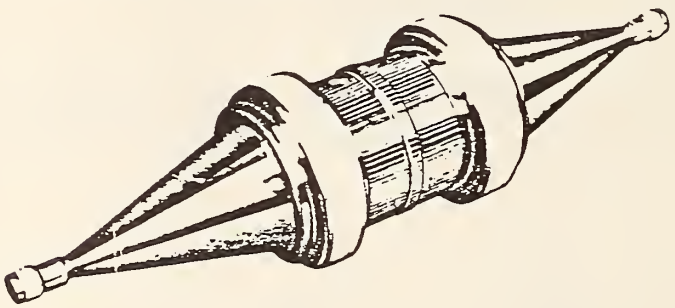

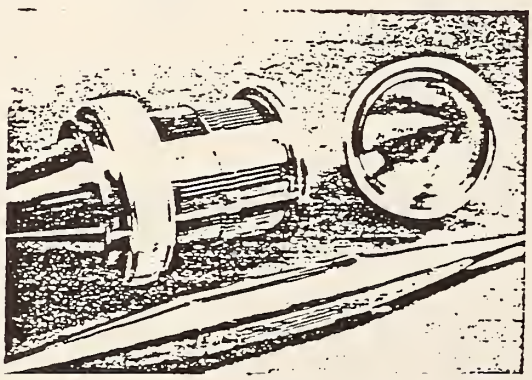

Figure 6. ASTM proposed coaxial transmission line holder.

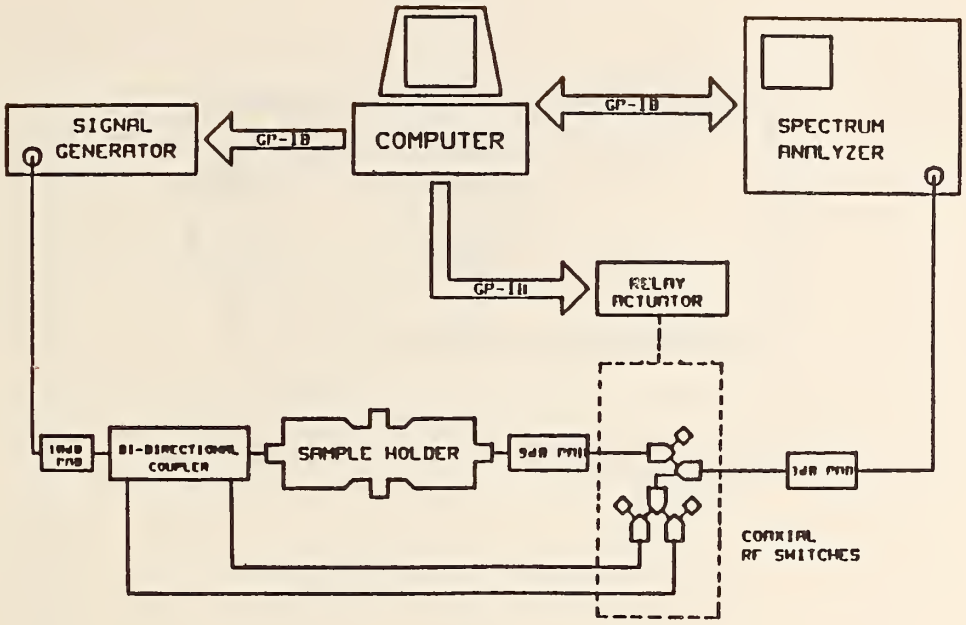

Figure 7. Block diagram of an automated coaxial holder IL measurement system.

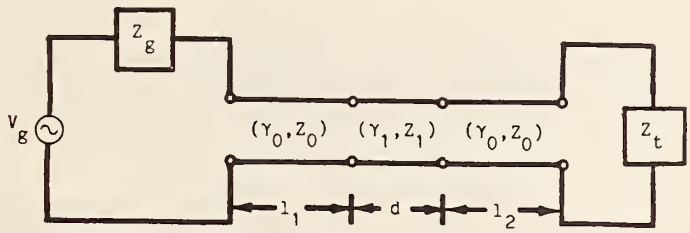

a. ASTM proposed coaxial holder as a reflective transmission line.

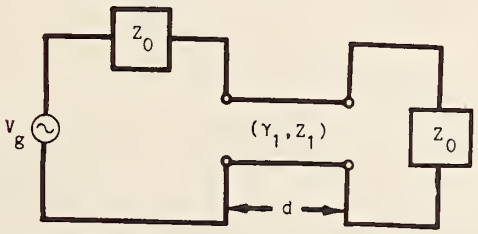

b. Matched line model.

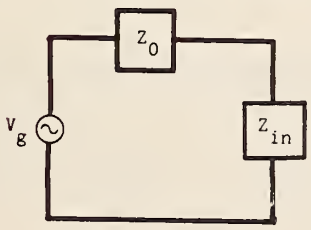

c. Input load seen by the generator.

Figure 8. ASTM proposed coaxial holder circuit models.

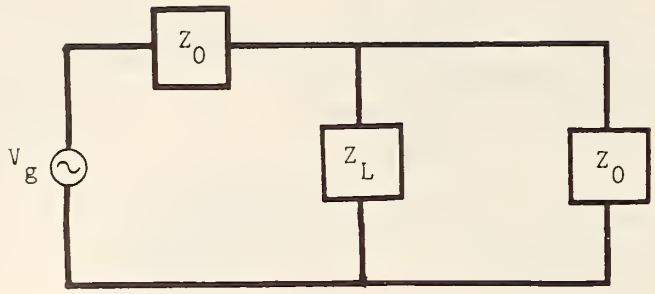

Figure 9. Idealized coaxial holder transmission line circuit model.

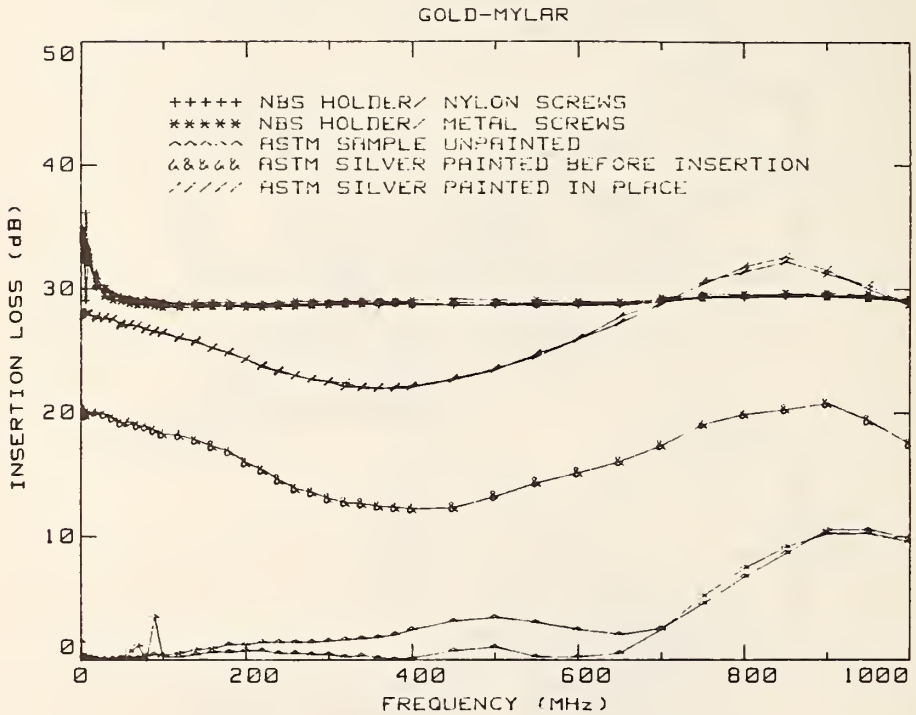

Figure 10. Insertion loss for the gold-Mylar sample measured in the ASTM proposed, and NBS flanged coaxial holders.

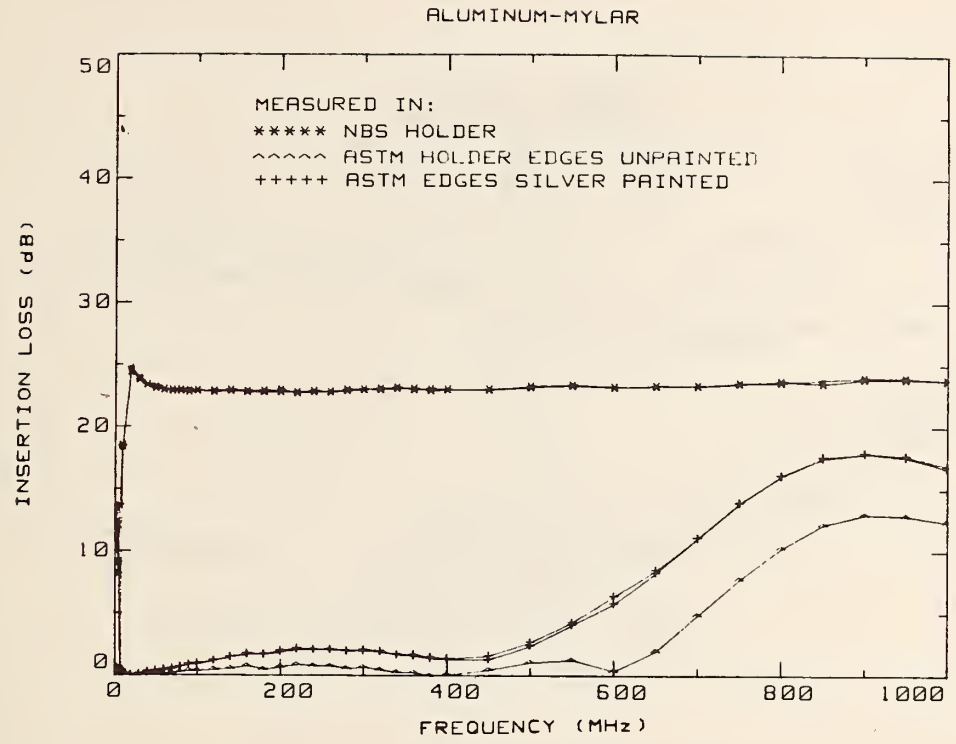

Figure 11. Insertion loss for the aluminum-Mylar sample measured in the ASTM proposed, and NBS flanged coaxial holders.

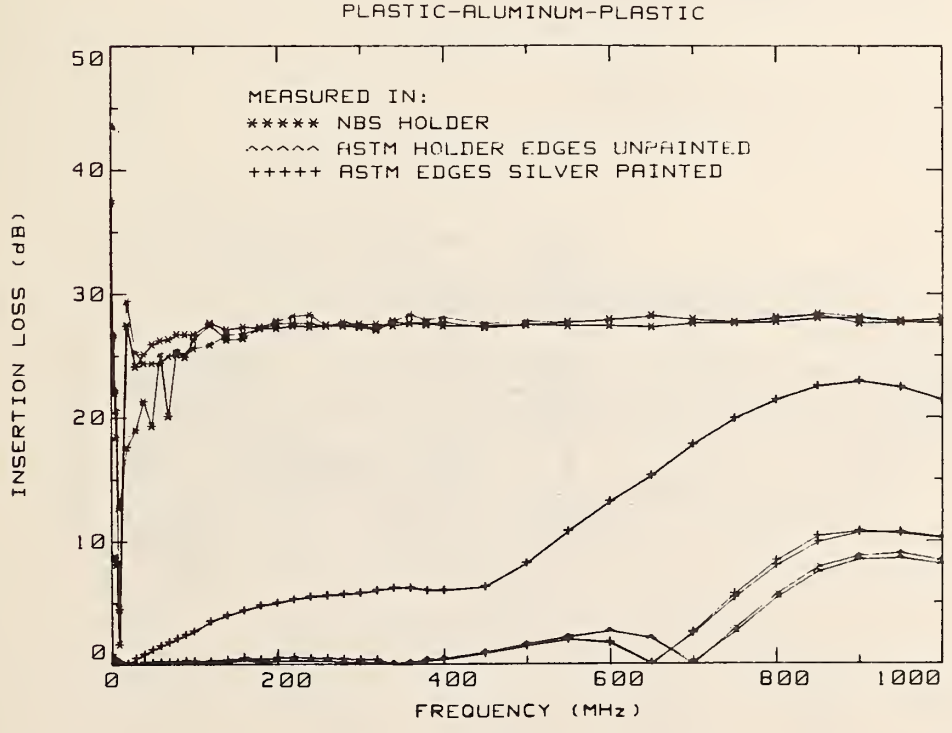

Figure 12. Insertion loss for the plastic-aluminum-plastic sample measured in the ASTM proposed, and NBS flanged coaxial holders.

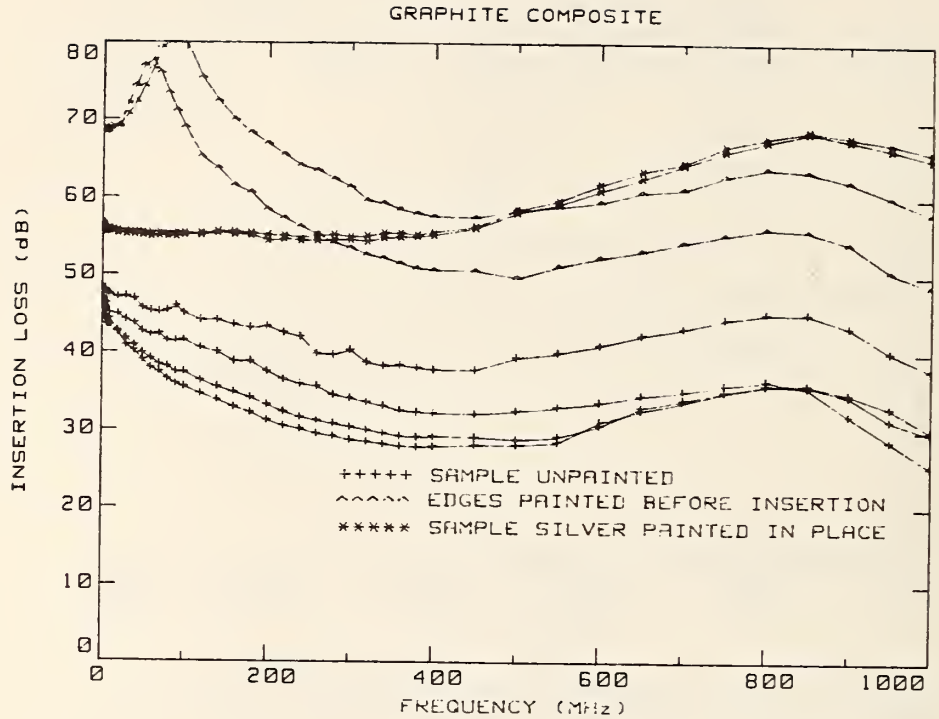

Figure 13. Insertion loss for the graphite composite sample measured in the ASTM proposed coaxial holder.

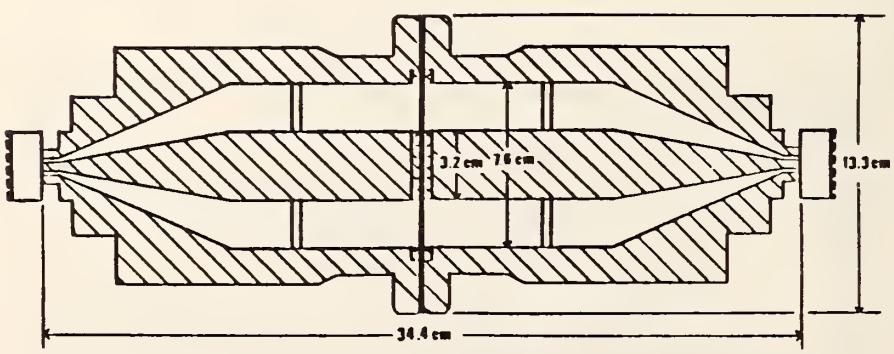

Figure 14. Flanged coaxial transmission line holder.

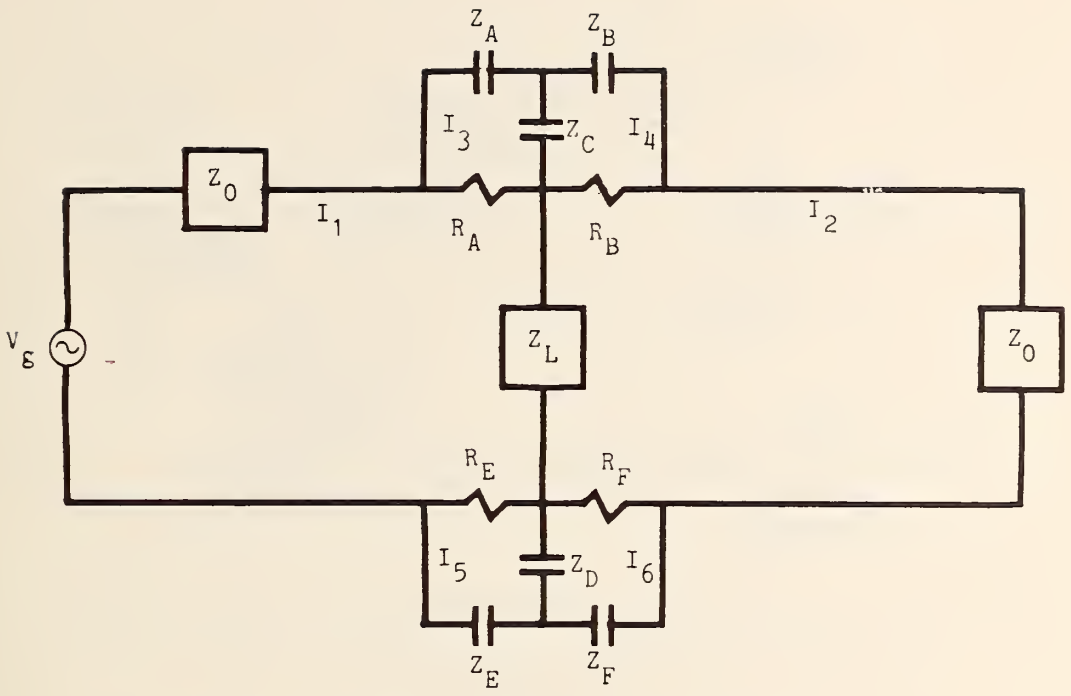

Figure 15. Flanged coaxial holder circuit model.

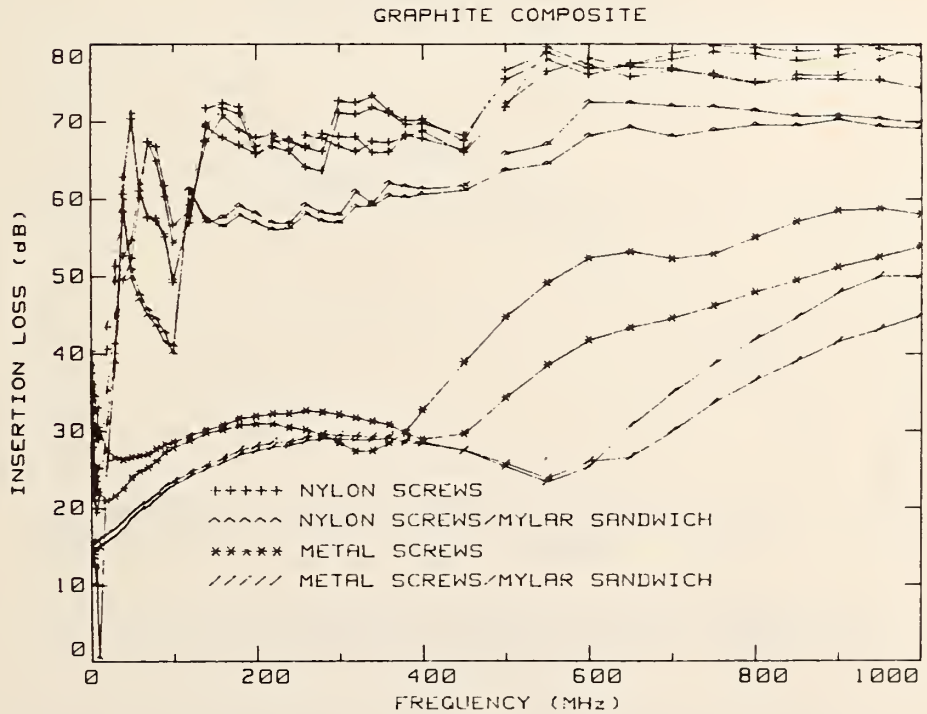

Figure 16. Insertion loss for the graphite composite sample measured in the NBS flanged coaxial holder.

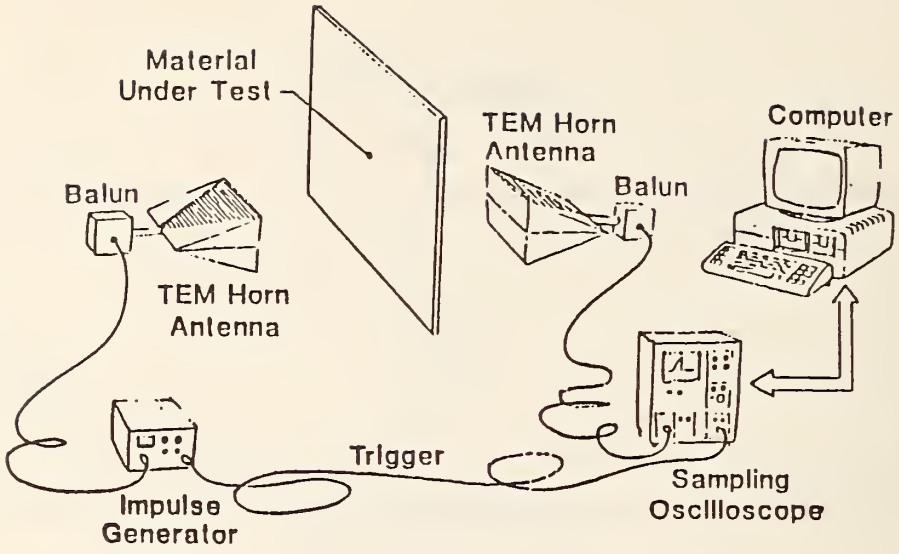

Figure 17. The time domain shielding effectiveness measurement system.

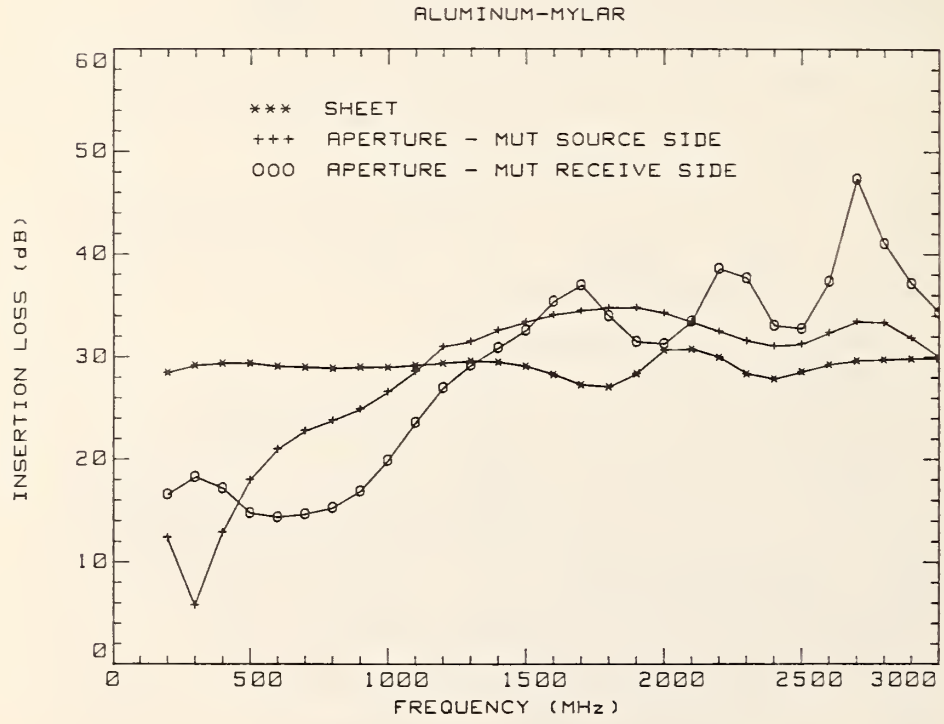

Figure 18. Insertion loss for the aluminum-Mylar sample (large sheet and aperture) measured with the time domain system.

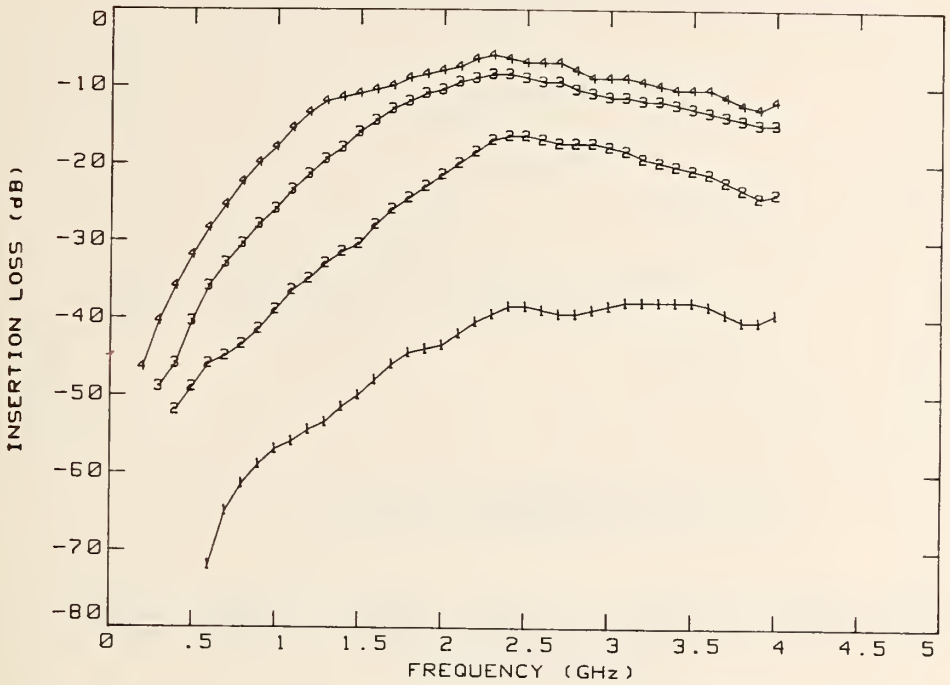

Figure 19. Time domain signal coupling between horn antennas for various empty aperture sizes (1-4 in).

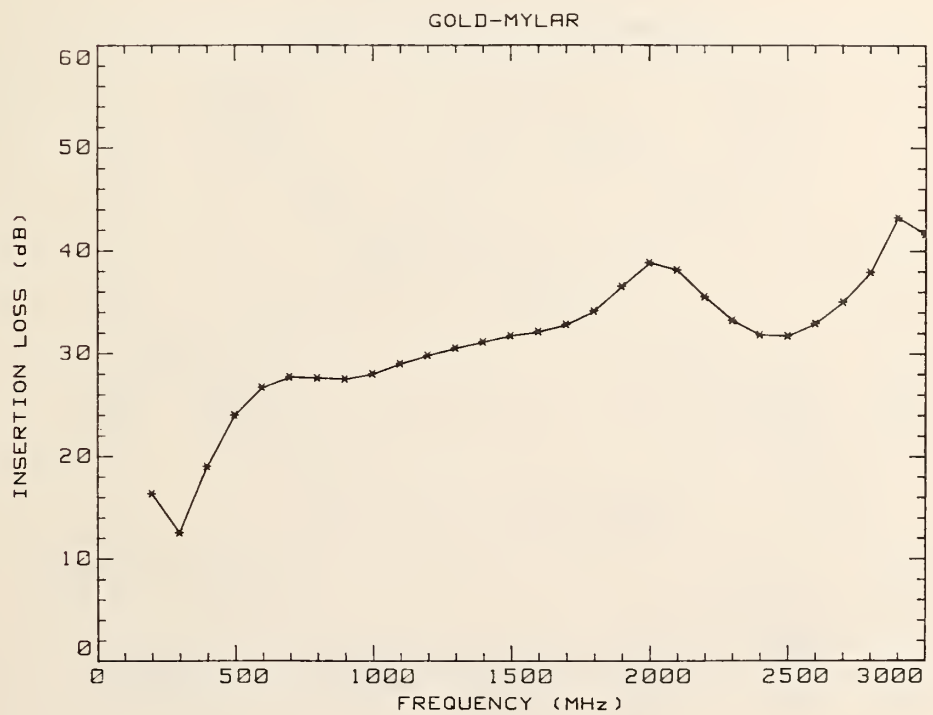

Figure 20. Insertion loss for the gold-Mylar sample (source side over an aperture) measured with the time domain system.

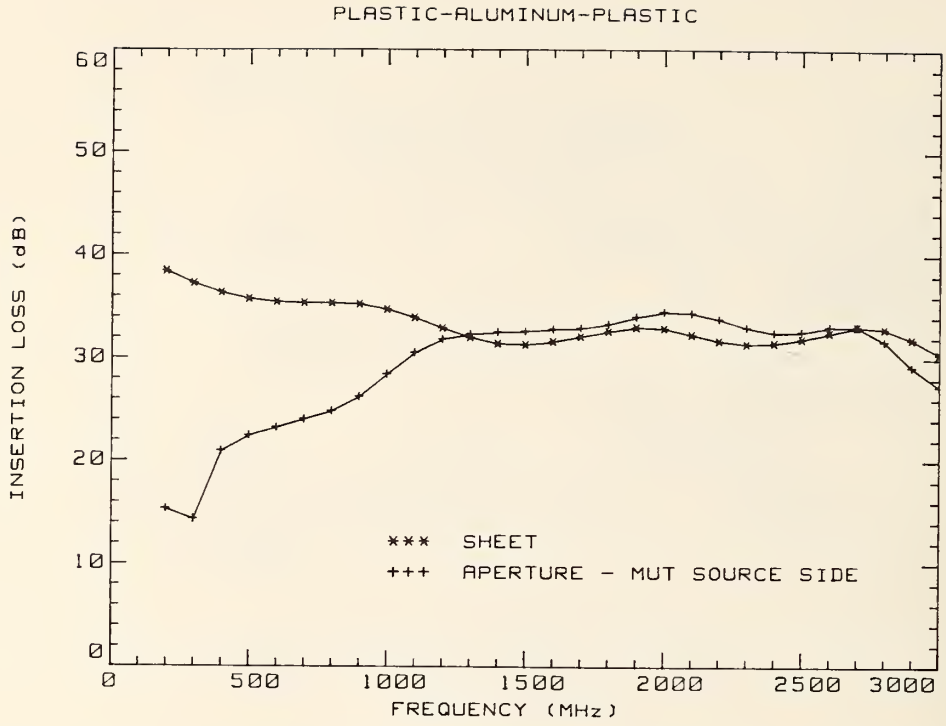

Figure 21. Insertion loss for the plastic-aluminum-plastic sample (large sheet and source side over an aperture) measured with the time domain system.

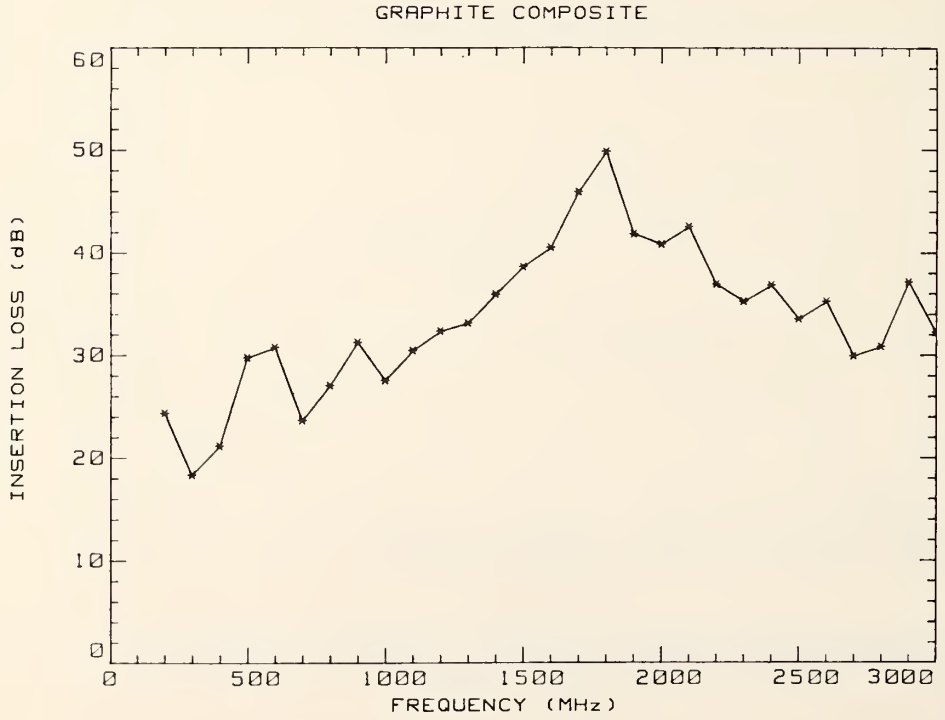

Figure 22. Insertion loss for the graphite composite sample (source side over an aperture) measured with the time domain system.

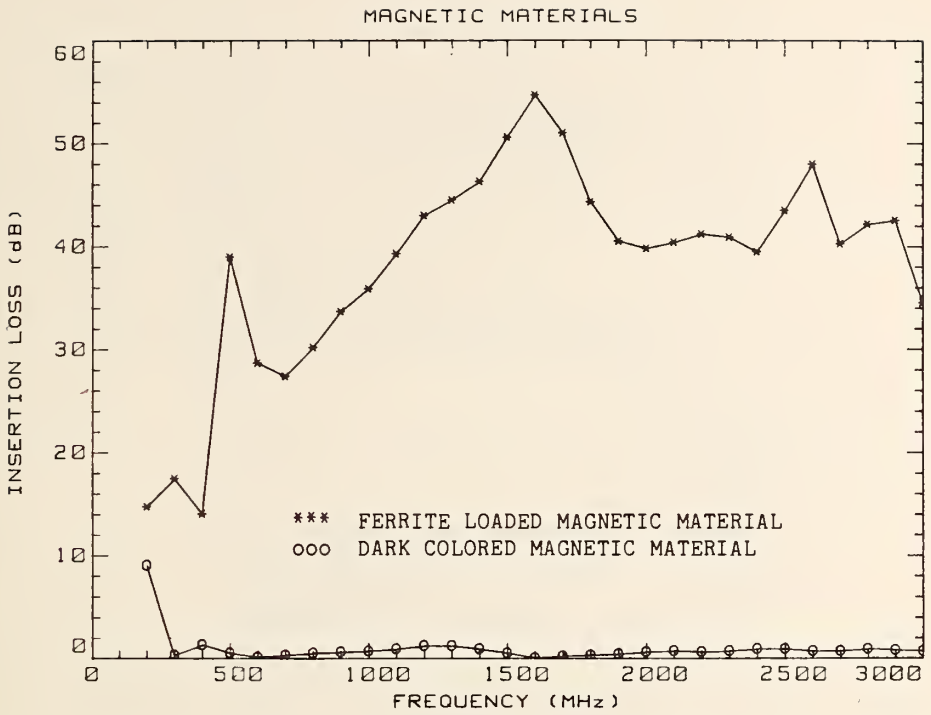

Figure 23. Insertion loss for two magnetic material samples (source side over an aperture) measured with the time domain system.

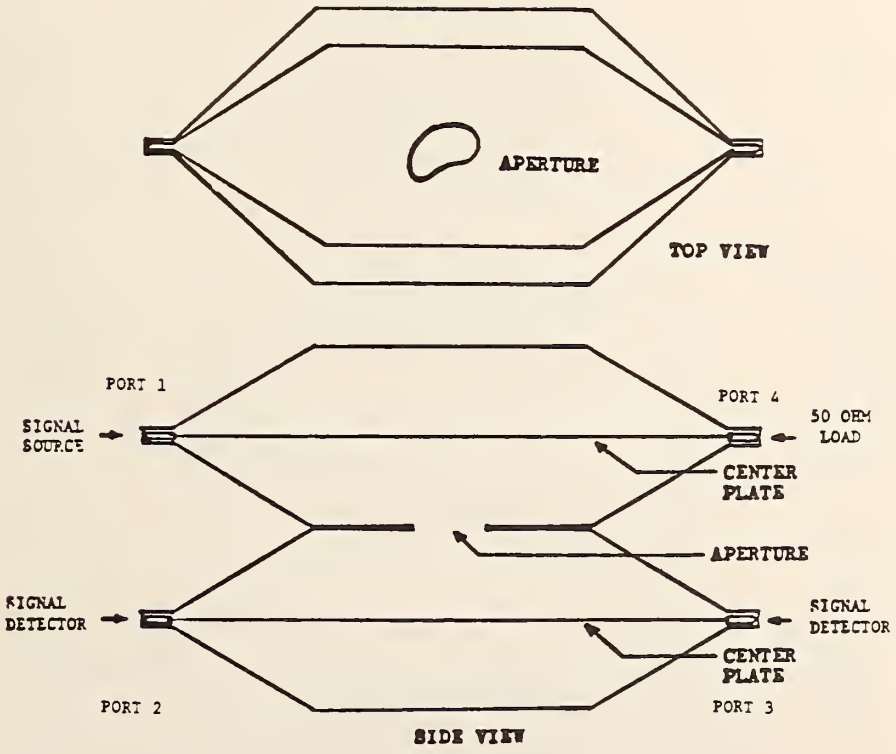

Figure 24. The dual TEM cell.

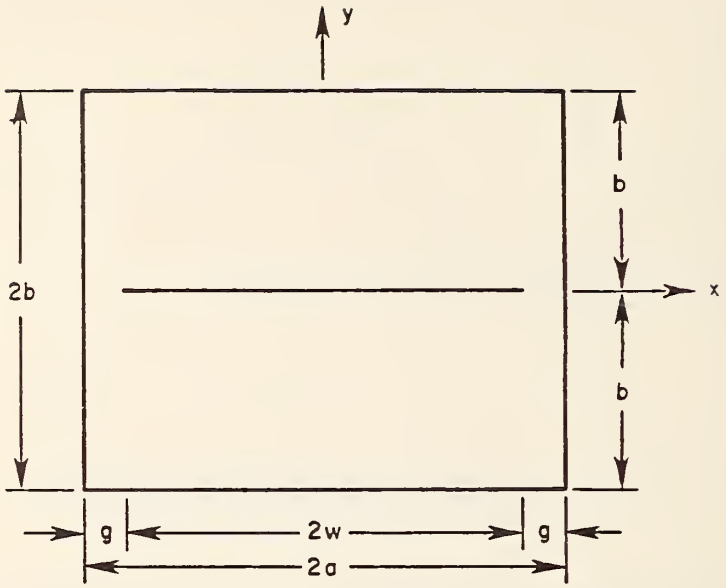

Figure 25. The cross section of a rectangular coaxial transmission line.

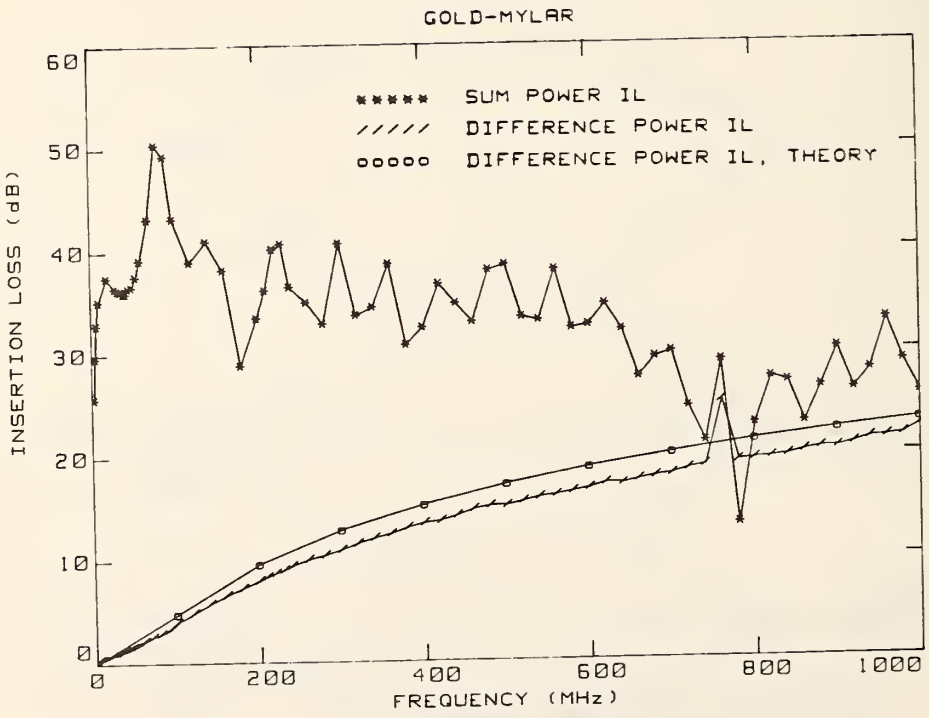

Figure 26. Insertion loss for the gold-Mylar sample measured in the dual TEM cell.

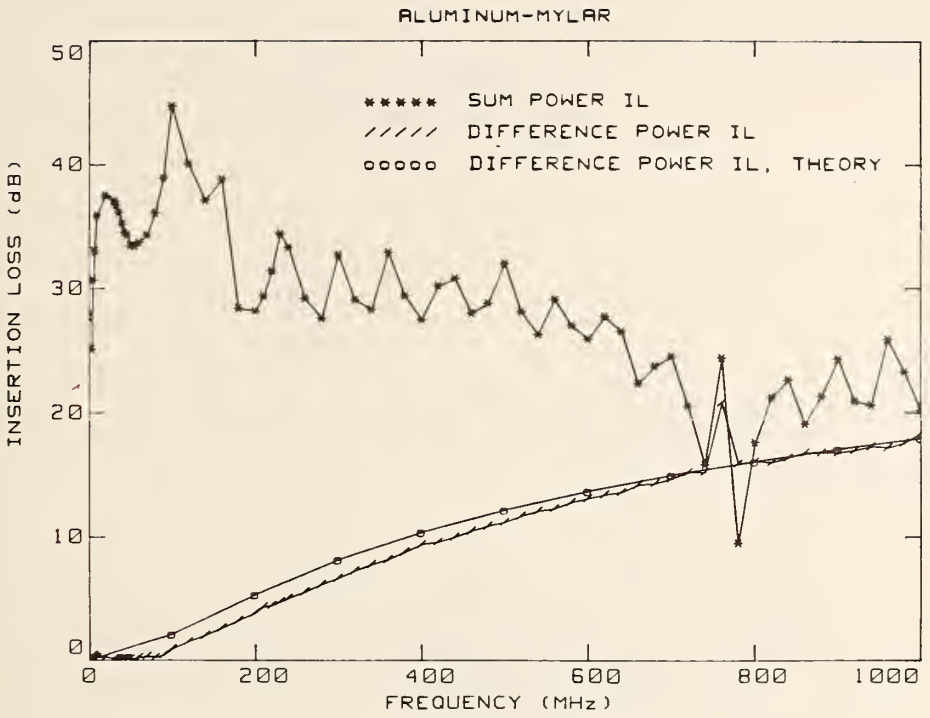

Figure 27. Insertion loss for the aluminum-Mylar sample measured in the dual TEM cell.

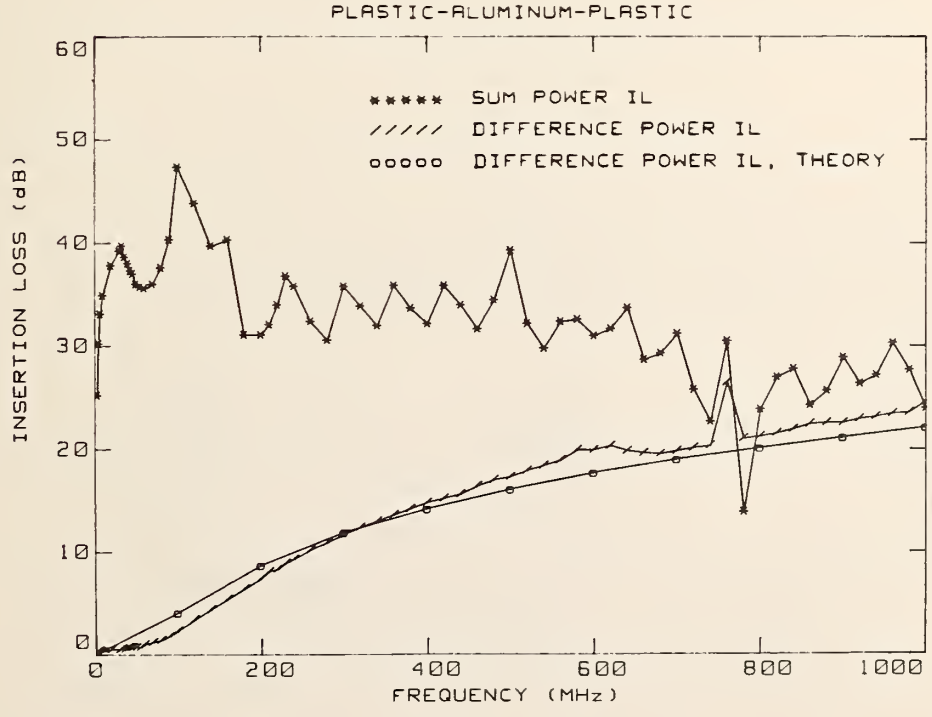

Figure 28. Insertion loss for the plastic-aluminum-plastic sample measured in the dual TEM cell.

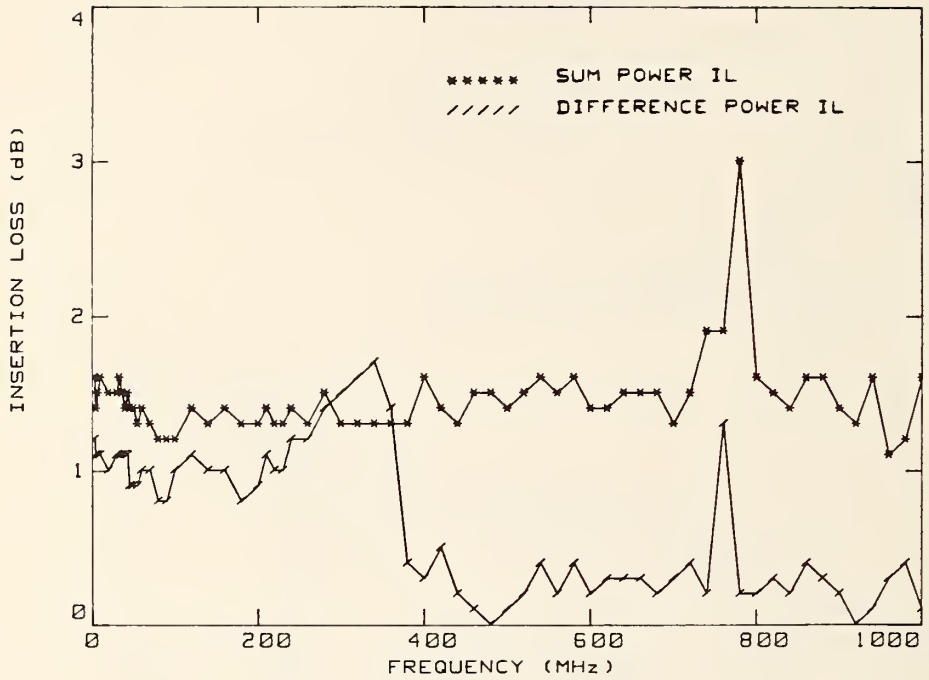

Figure 29. Insertion loss for a magnetic material sample measured in the dual TEM cell.

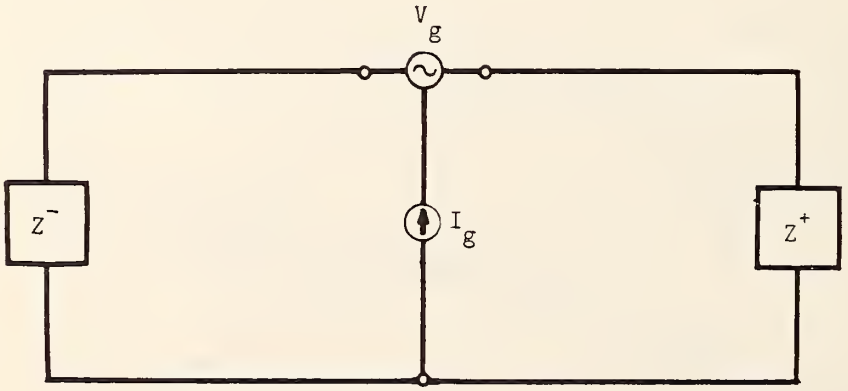

Figure 30. Apertured coaxial transmission line equivalent circuit model.

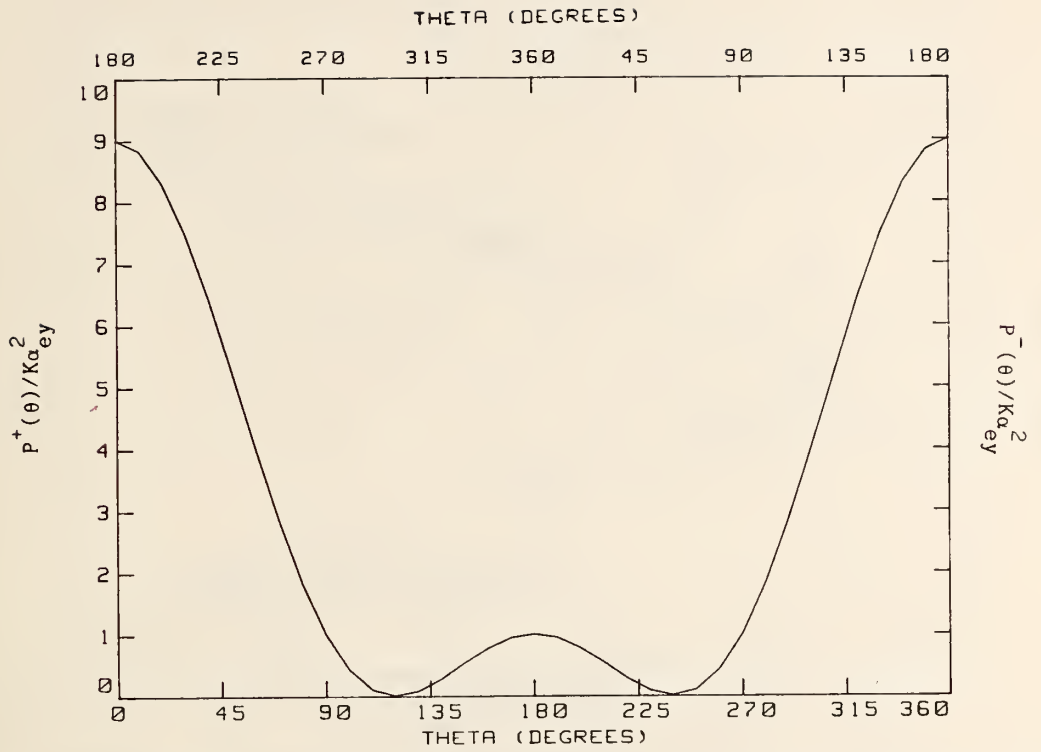

Figure 31. Normalized power coupled to the output ports (theory) as a function of theta (angle about the aperture normal) for an apertured coaxial transmission line.

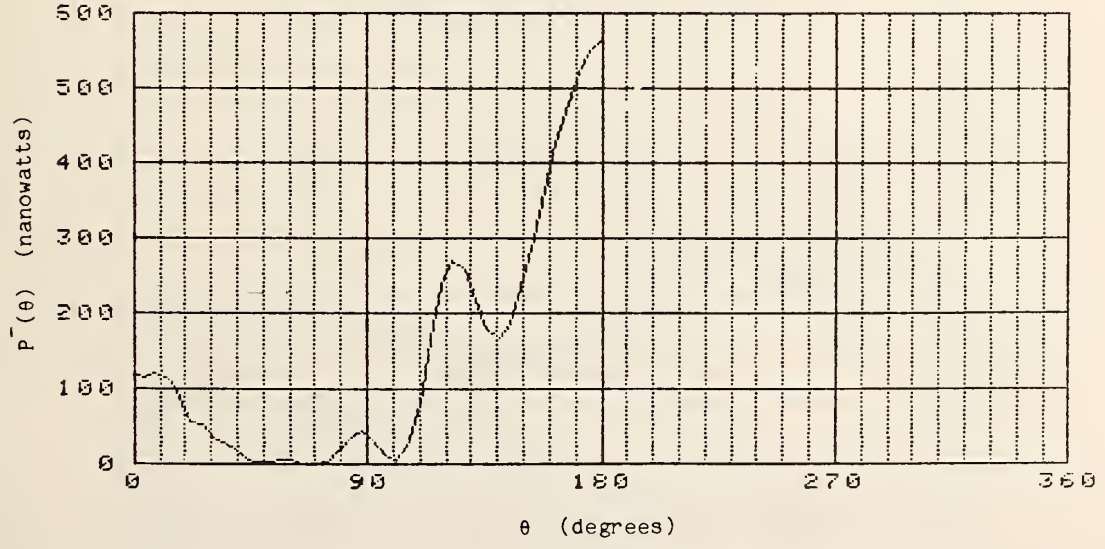

Figure 32. Power coupled to one of the output ports (measured) for an apertured coaxial transmission line.

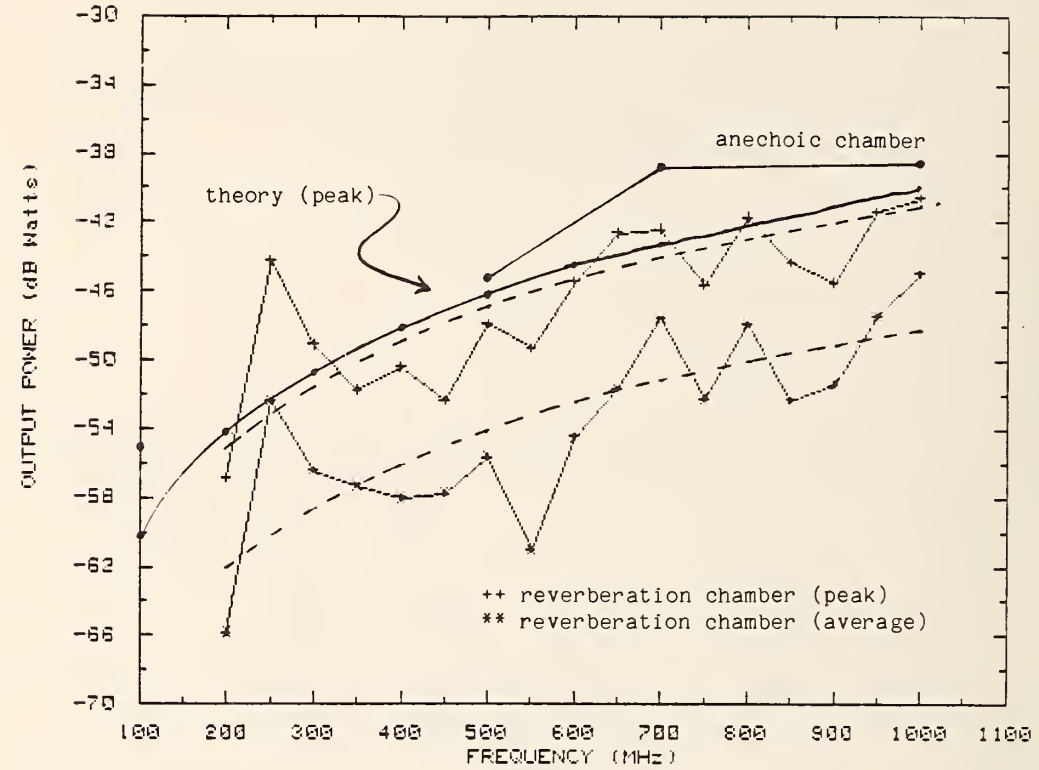

Figure 33. Power coupled to a square apertured rectangular coaxial transmission line measured in both an anechoic chamber and a reverberation chamber.

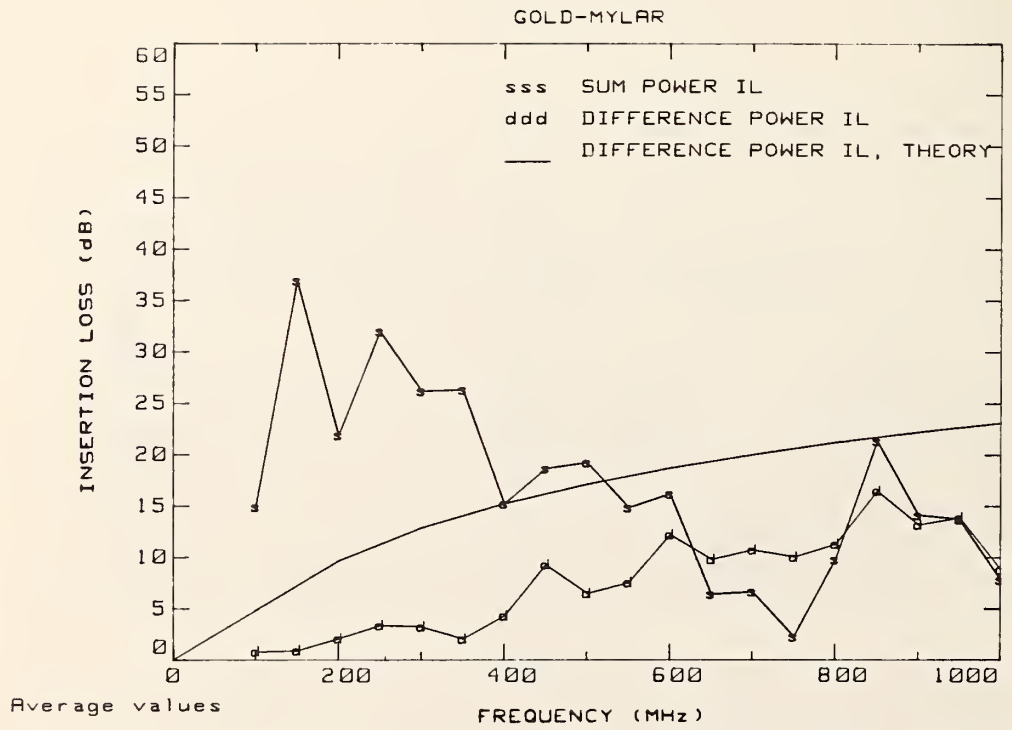

Figure 34. Insertion loss for the gold-Mylar sample measured with a square apertured rectangular coaxial transmission line in a reverberation chamber.

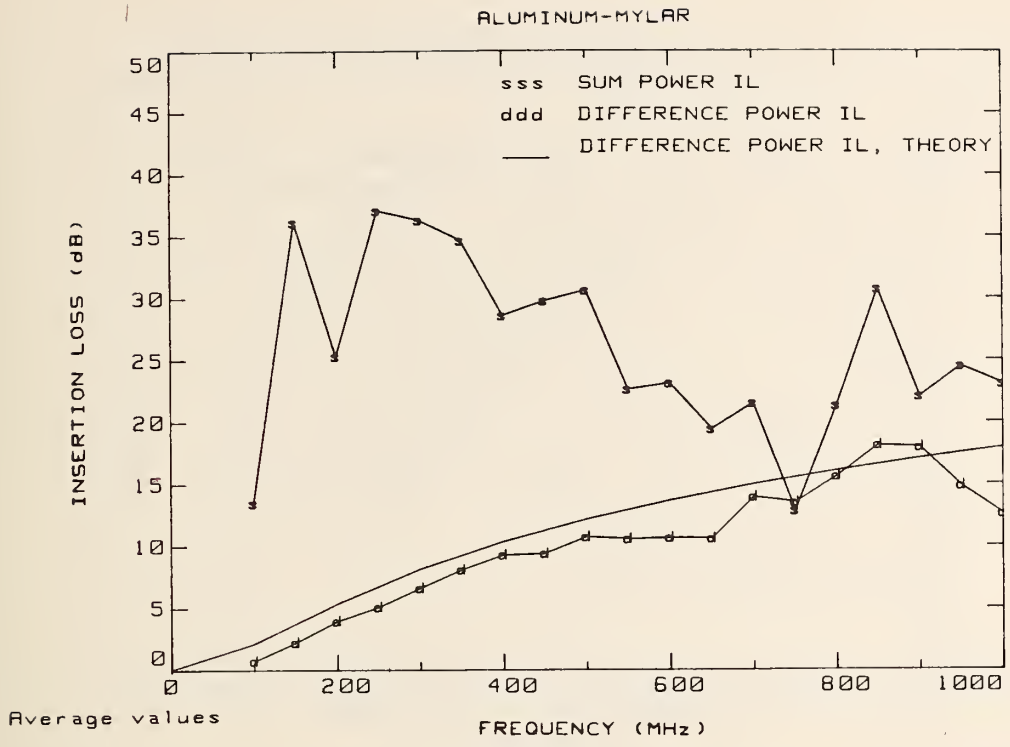

Figure 35. Insertion loss for the aluminum-Mylar sample measured with a square apertured rectangular coaxial transmission line in a reverberation chamber.

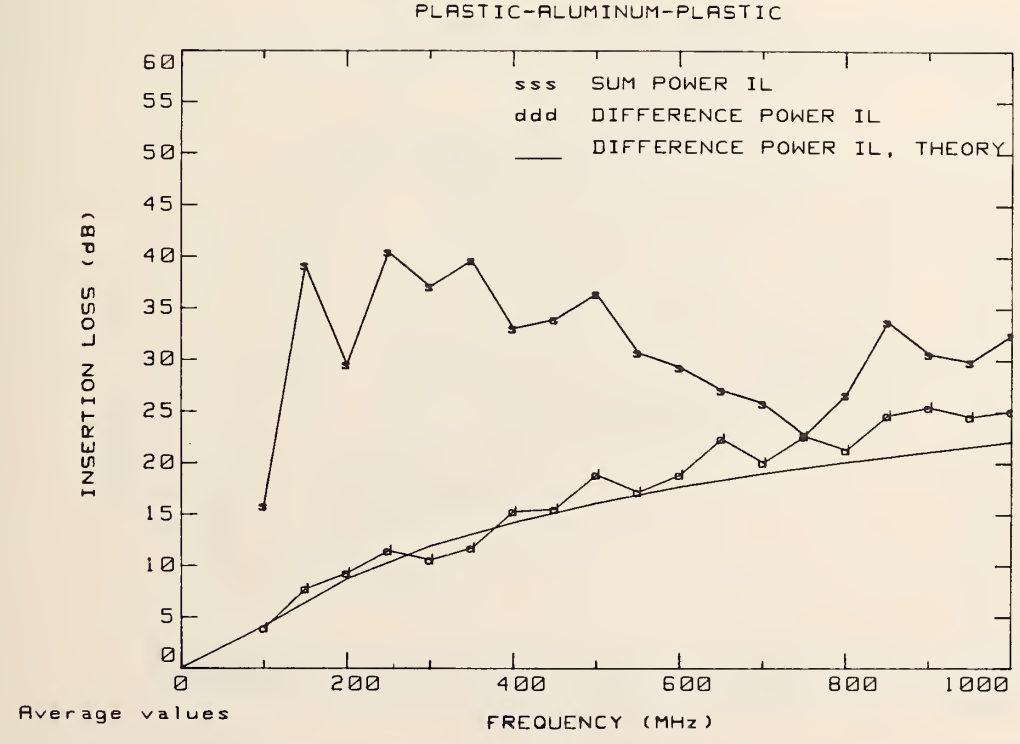

Figure 36. Insertion loss for the plastic-aluminum-plastic sample measured with a square apertured rectangular coaxial transmission line in a reverberation chamber.

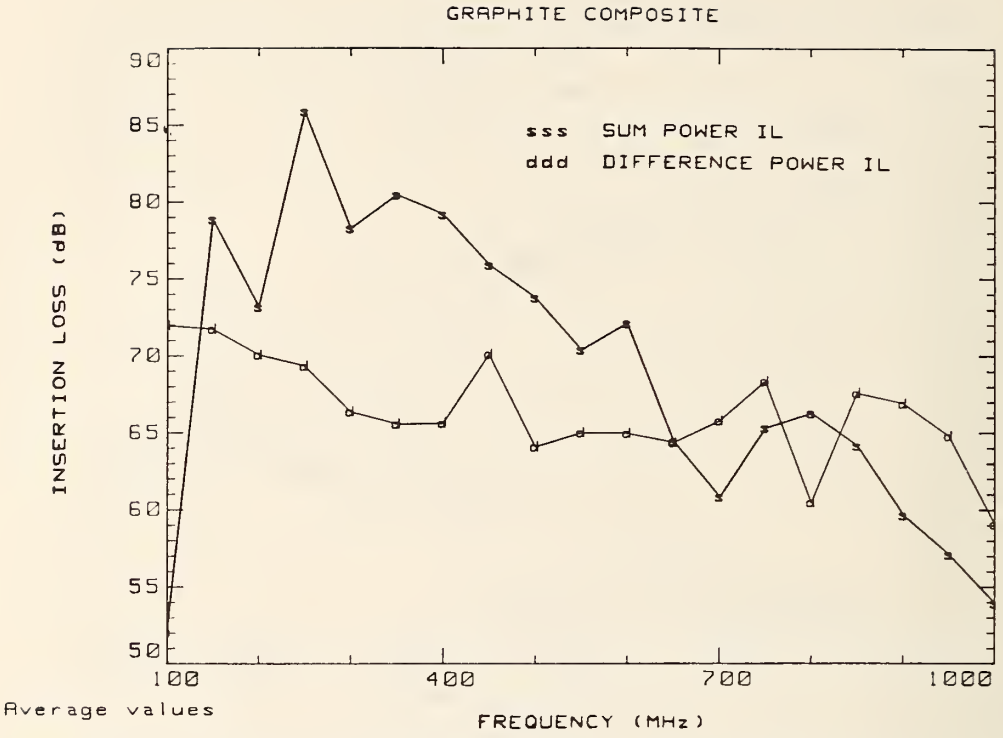

Figure 37. Insertion loss for the graphite composite sample measured with a square apertured rectangular coaxial transmission line in a reverberation chamber.

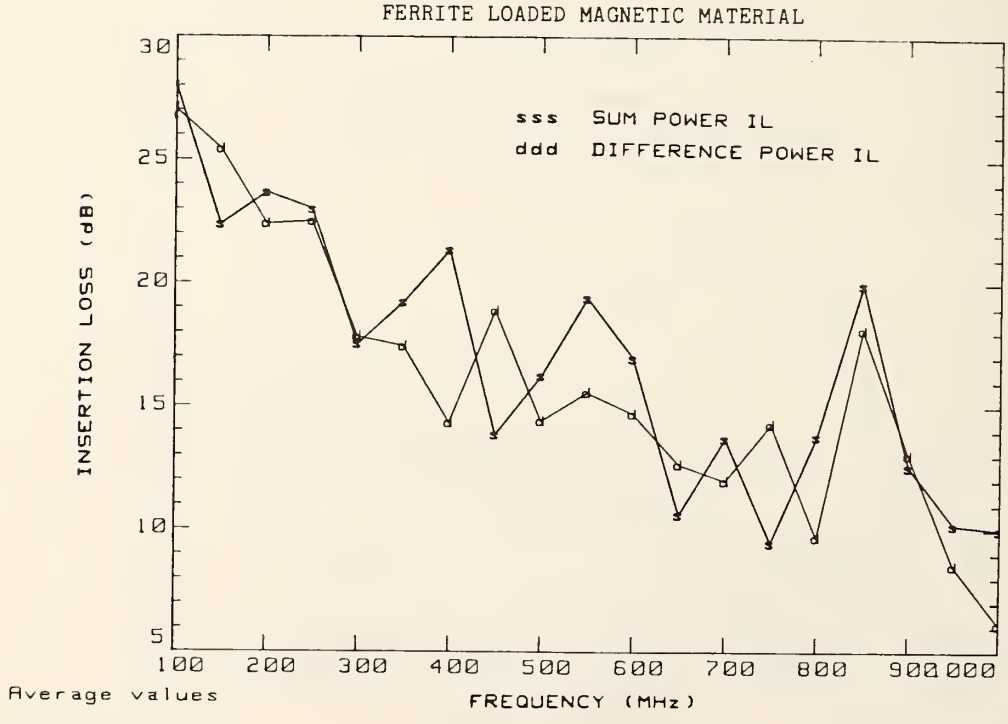

Figure 38. Insertion loss for a magnetic material sample measured with a square apertured rectangular transmission line in a reverberation chamber.

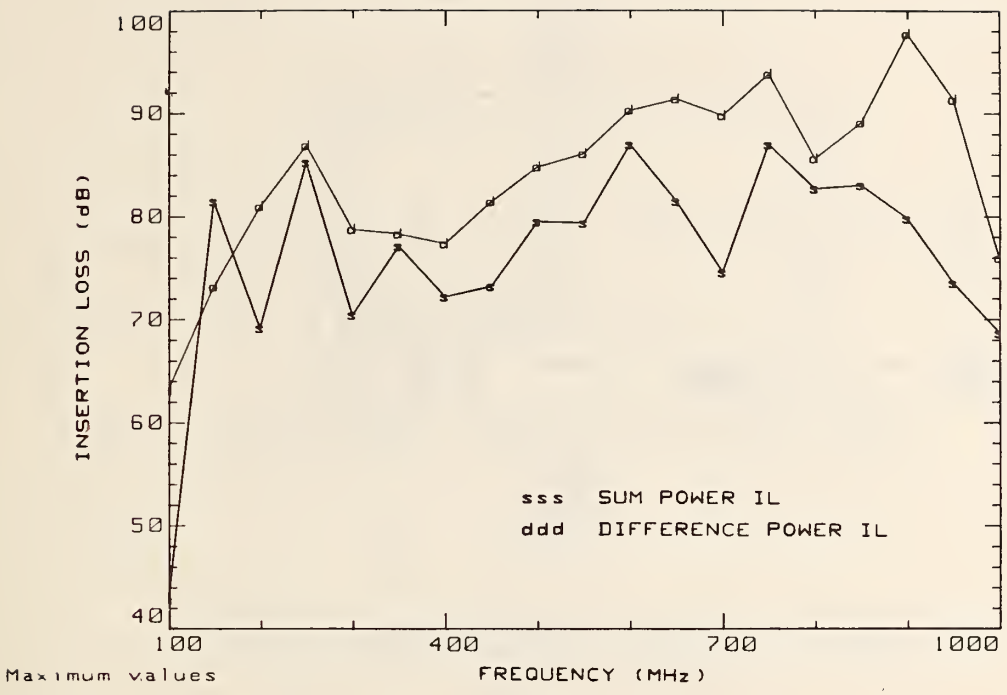

Figure 39. Insertion loss for a copper-magnetic-copper layered material measured with a square apertured rectangular transmission line in a reverberation chamber.

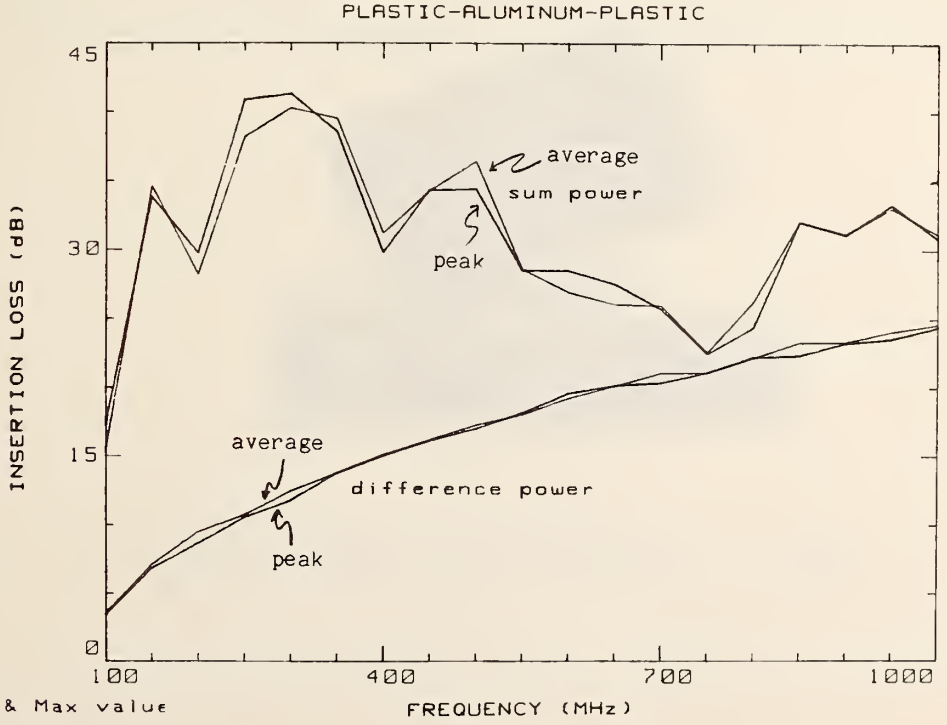

Figure 40. Insertion loss for both the peak and average signals for the plastic-aluminum-plastic sample measured with a square apertured rectangular transmission line in a reverberation chamber.

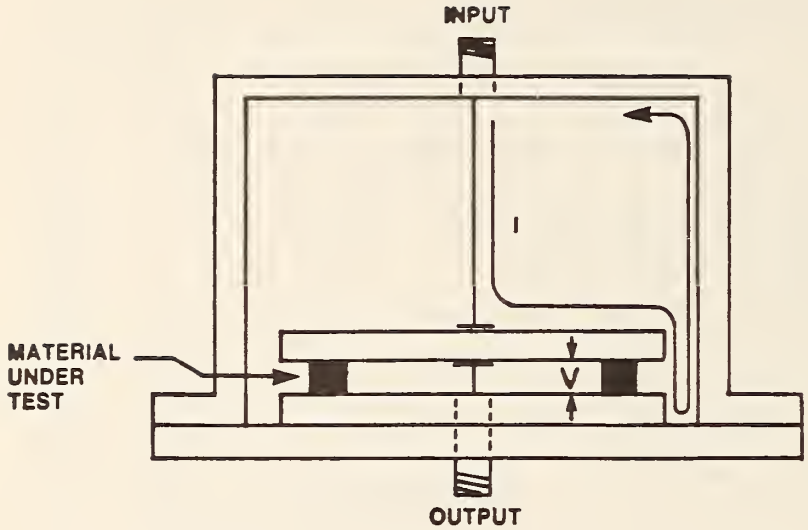

Figure 41. The transfer impedance measurement system.

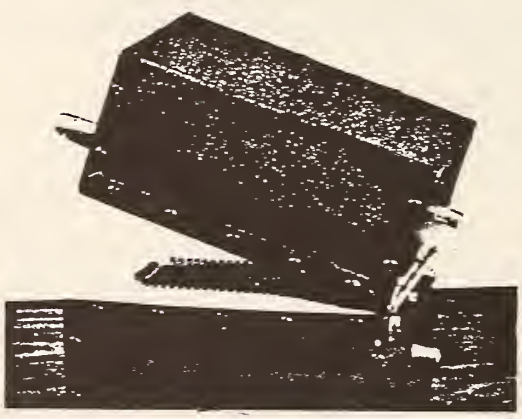

Figure 42. The ASTM proposed dual chamber fixture.

Table 1. Summary of SE test methods

SE TEST METHOD	FREQUENCY		FIELD TYPE SIMULATED	MUT REQUIREMENTS	THEORETICAL SUPPORT FOR DATA	DYNAMIC RANGE (dB)	REPEATA-BILITY	TIME REQUIRED FOR MEAS. (HRS)
	LOW	HIGH						
SHIELDED ROOM	30 MHz (LBE)	I GHz (LBE)	UNKNOWN	COVER AN APERTURE	POOR	80-90	POOR	30-40
ASTM TYPE COAXIAL HOLDER	I MHz (LBE)	I GHz	NORMAL PLANE WAVE	ANNULAR DISK	GOOD	90-I00	MODERATE	.25
FLANGED COAXIAL HOLDER	1 MHz (LBE)	1 GHz	NORMAL PLANE WAVE	CIRCULAR + REFERENCE RING & DISK	GOOD	90-I00	GOOD	.25
TIME DOMAIN	200 MHz	3.5 GHz (LBE)	NORMAL PLANE WAVE	LARGE SHEET	GOOD	50-60	GOOD	.25
				COVER AN APERTURE	MODERATE	40-50	GOOD	.25
DUAL TEM CELL	I MHz (LBE)	I GHz	NEAR-FIELD OR GRAZING PLANE WAVE	COVER AN APERTURE	GOOD	50-60	GOOD	.5
APERTURED TEM CELL	200 MHz	I GHz (LBE)	NEAR-FIELD	COVER AN APERTURE	GOOD	90-100	GOOD	3-4

APPENDIX A ASTM PROPOSED COAXIAL HOLDER CIRCUIT ANALYSIS

The ASTM coaxial holder may be schematically represented as shown in figure 8a, where V_g is the voltage source and Z_g the associated internal generator impedance, Z_0 and γ_0 are the characteristic impedance and propagation constant of the line (nominally 50 ohms and jk_0 respectively), Z_1 and γ_1 are the characteristic impedance and the propagation constant in the test material loaded section of the line, Z_t is the termination impedance (typically a 50 ohm load), and l_1, l_2 and d are the lengths of the empty line sections and material loaded section as indicated in figure 8a.

We need not analyze the most general case, however, since in practical applications we would have $Z_g = Z_t = Z_0$. In this case the ASTM holder schematic reduces to that of figure 8b. The specific quantities for a circular coaxial transmission line are as follows,

$$
\begin{aligned}
Z_0 &= \frac{\eta_0}{2\pi} \ln(b/a) \quad ; \quad \eta_0 = (\mu_0/\varepsilon_0)^{1/2} \\
Z_1 &= \frac{\eta_1}{2\pi} \ln(b/a) \quad ; \quad \eta_1 = \eta_0(\mu_r/\varepsilon_{r1})^{1/2} \\
\varepsilon_{r1} &= \varepsilon_r - j\sigma/\omega\varepsilon_0 \\
\gamma_1 &= jk_0(\mu_r\varepsilon_{r1})^{1/2}
\end{aligned}
\qquad \text{(A-1)}
$$

where a and b are the inner and outer radii, ε_r, μ_r and σ are the relative permittivity, permeability and the conductivity of the material as defined in the introduction, and propagation in the various sections is according to $\exp(-\gamma_j z)$.

The power coupled to the termination (Z_0) for the above reflective transmission line may be readily determined. Begin with the reflection coefficient $\Gamma(z)$ just beyond the output terminal ($z = 0^-$) which is

$$\Gamma(0^-) = \frac{Z_0 - Z_1}{Z_0 + Z_1} . \qquad \text{(A-2)}$$

Thus at $z = -d^+$ (just right of the input terminal) we have

$$\Gamma(-d^+) = \frac{Z_0 - Z_1}{Z_0 + Z_1} e^{-2\gamma_1 d} . \qquad \text{(A-3)}$$

The impedance Z(z) at z = -d is given by

$$Z(-d) = Z_1 \frac{1 + \Gamma(0^-)e^{-2\gamma_1 d}}{1 - \Gamma(0^-)e^{-2\gamma_1 d}} = Z_1 \frac{Z_0 + Z_1 \tanh\gamma_1 d}{Z_1 + Z_0 \tanh\gamma_1 d} . \qquad \text{(A-4)}$$

Therefore the power to the input port is determined by the schematic shown in figure 8c. The input power P_{in} is given by

$$
\begin{aligned}
P_{in} &= \frac{1}{2}|I_{in}|^2 \, \mathrm{Re}\{Z(-d)\} \\
I_{in} &= V_g/\{Z_0 + Z(-d)\} .
\end{aligned}
\qquad \text{(A-5)}
$$

Maximal input power P_{max} occurs when the load is matched, or $Z(-d) = Z_0$. This corresponds to no test material present, i.e. $Z_1 = Z_0$. We then have

$$P_{max} = V_g^2/8Z_0 \ . \tag{A-6}$$

The difference between P_{max} and P_{in} is the amount of power reflected by the material P_{refl} given by

$$P_{refl} = |\Gamma(-d^-)|^2 \, P_{max} \ , \tag{A-7}$$

and the reflection coefficient $\Gamma(-d^-)$ just left of the material is given by

$$\Gamma(-d^-) = \frac{Z(-d) - Z_0}{Z(-d) + Z_0} \ . \tag{A-8}$$

Notice that

$$|\Gamma(-d^-)|^2 = 1 - \frac{4Z_0 Re\{Z(-d)\}}{|Z(-d) + Z_0|^2} \ . \tag{A-9}$$

Thus

$$P_{refl} = \frac{1}{8Z_0}|V_g|^2 \left(1 - \frac{4Z_0 Re\{Z(-d)\}}{|Z(-d) + Z_0|^2}\right) \ . \tag{A-10}$$

The input power available at the sample will be the difference between the maximal power and the reflected power, i.e.

$$P_{max} - P_{refl} = \frac{1}{2}|V_g|^2 \frac{Re\{Z(-d)\}}{|Z(-d) + Z_0|^2} = P_{in} \ , \tag{A-11}$$

as predicted by (A-5).

We next may consider the output power delivered to the termination load. The current just inside the material is

$$I(-d^+) = I_g e^{\gamma_1 d}[1 - \Gamma(-d^+)] = I_{in} \ , \tag{A-12}$$

where I_g is the current produced by the generator. Thus we have

$$I_g = I_{in} e^{-\gamma_1 d}/[1 - \Gamma(-d^+)] \ . \tag{A-13}$$

The current in the termination I_t at $z = 0$ is given by

$$I_t = I_g[1 - \Gamma(0^-)] = I_{in} e^{-\gamma_1 d}[1 - \Gamma(0^-)]/[1 - \Gamma(-d^+)] \ , \tag{A-14}$$

or upon substitution of (A-2) and (A-3)

$$I_t = \frac{I_{in} Z_1}{Z_1 \cosh\gamma_1 d + Z_0 \sinh\gamma_1 d} \ . \tag{A-15}$$

Thus the power delivered to the termination P_t is

$$P_t = \frac{Z_0}{2} |I_{in}|^2 \left|\frac{Z_1}{Z_1 \cosh\gamma_1 d + Z_0 \sinh\gamma_1 d}\right|^2 . \tag{A-16}$$

We also have that $P_{in} - P_t$ represents the power absorbed by the material P_{abs}, that is

$$\begin{aligned} P_{abs} &= \frac{1}{2}|I_{in}|^2 \, \mathrm{Re}\{Z(-d)\} - \frac{Z_0}{2} |I_t|^2 \\ &= \frac{1}{2}|I_{in}|^2 \left[\mathrm{Re}\{Z(-d)\} - Z_0 \left|\frac{Z_1}{Z_1 \cosh\gamma_1 d + Z_0 \sinh\gamma_1 d}\right|^2 \right] . \end{aligned} \tag{A-17}$$

Together these quantities sum to P_{max}, i.e.

$$P_{max} = P_{refl} + P_{abs} + P_t . \tag{A-18}$$

If we divide this relationship by P_t then we have

$$\frac{P_{max}}{P_t} = 1 + \frac{P_{refl}}{P_t} + \frac{P_{abs}}{P_t} . \tag{A-19}$$

This of course represents an insertion loss measurement,

$$IL = 10 \log\left|\frac{P_{max}}{P_t}\right| = 10 \log\left|1 + \frac{P_{refl}}{P_t} + \frac{P_{abs}}{P_t}\right| . \tag{A-20}$$

The above expression (A-20) simply reiterates the fact that if there is no reflected or absorbed power then there is no insertion loss. Equation (A-20) may alternately be written

$$IL = 10 \log\left|\frac{P_{refl}}{P_t} + \frac{P_{in}}{P_t}\right| , \tag{A-21}$$

where

$$\begin{aligned} \frac{P_{refl}}{P_t} &= \frac{\left[|Z(-d) + Z_0|^2 - 4Z_0 \mathrm{Re}\{Z(-d)\}\right] |Z_1 \cosh\gamma_1 d + Z_0 \sinh\gamma_1 d|^2}{4Z_0^2 |Z_1|^2} \\ \frac{P_{in}}{P_t} &= \frac{\mathrm{Re}\{Z(-d)\} |Z_1 \cosh\gamma_1 d + Z_0 \sinh\gamma_1 d|^2}{Z_0 |Z_1|^2} . \end{aligned} \tag{A-22}$$

We now may check some special cases.

(1) No load material is present. This implies that $Z_1 = Z_0$ and $\gamma_1 = jk_1$ ($k_1 = k_0(\varepsilon_r)^{1/2}$ and γ_1 is purely imaginary), and we see that $Z(-d) = Z_0$. Thus

$$\frac{P_{refl}}{P_t} = 0$$

$$\frac{P_{in}}{P_t} = 1 \ ,$$

and (A-21) shows that IL→0 as expected.

(2) The load material is a pure dielectric. In this case Z_1 is real, $\mu_r = 1$, $\gamma_1 = jk_1$, $\cosh\gamma_1 d = \cos k_1 d$, $\sinh\gamma_1 d = j\sin k_1 d$, and

$$\mathrm{Re}\{Z(-d)\} = \frac{Z_0 Z_1^2(1 + \tan^2 k_1 d)}{Z_1^2 + Z_0^2 \tan^2 k_1 d}$$

$$|Z(-d) + Z_0|^2 = \frac{4Z_0^2 Z_1^2 + (Z_1^2 + Z_0^2)^2 \tan^2 k_1 d}{Z_1^2 + Z_0^2 \tan^2 k_1 d} \ . \tag{A-23}$$

Inserting these into (A-22) yields

$$\frac{P_{refl}}{P_t} = \frac{(Z_1^2 - Z_0^2)^2 \sin^2 k_1 d}{4Z_0^2 Z_1^2}$$

$$\frac{P_{in}}{P_t} = 1 \ , \tag{A-24}$$

and thus

$$IL = 20\log\left|1 + \frac{(Z_1^2 - Z_0^2)\sin k_1 d}{2Z_0 Z_1}\right| \ . \tag{A-25}$$

We see from (A-17) that no power is absorbed in the material, as expected, and only reflection introduces insertion loss. Also,

$$\frac{P_{refl}}{P_t} = 0 \quad \text{if } k_1 d = \text{an integer multiple of } \pi, \tag{A-26}$$

corresponding to the well known result that a half-wave thickness of dielectric introduces no reflection (if surrounded by the same material).

(3) The load material is a good conductor ($\sigma/\omega\varepsilon_0 >> \varepsilon_r$), then

$$\gamma_1 \approx \sigma\eta_1$$

$$\eta_1 \approx (1 + j)/\sigma\delta \ , \tag{A-27}$$

where δ is the skin depth. If, in addition the material is electrically thin (i.e. $d/\delta << 1$) and we retain only first order terms in σd, then we find

$$Z(-d) \approx \frac{Z_0(\eta_0 + \eta_1^2 \sigma d)}{\eta_0(1 + \eta_0 \sigma d)}$$

$$\mathrm{Re}\{Z(-d)\} \approx \frac{Z_0}{1 + \eta_0 \sigma d} \tag{A-28}$$

$$|Z_0 + Z(-d)|^2 \approx \frac{Z_0^2(2 + \eta_0\sigma d)^2}{(1 + \eta_0\sigma d)^2} .$$

The power expressions in (A-21) reduce to

$$\frac{P_{refl}}{P_t} \approx \frac{(\eta_0\sigma d)^2}{4}$$

$$\frac{P_{in}}{P_t} \approx 1 + \eta_0\sigma d , \tag{A-29}$$

and combine to give the following insertion loss

$$IL \approx 20 \log\left(1 + \frac{1}{2}\eta_0\sigma d\right) . \tag{A-30}$$

The above result may also be derived based on the analysis of the simple circuit model shown in figure 9. If we consider this model we find

$$P_{in} = \frac{1}{2}|I_{in}|^2 \, Re\{Z_{in}\}$$

$$Z_{in} = \frac{Z_0 Z_L}{Z_0 + Z_L} , \text{ and } I_{in} = \frac{V_g}{Z_{in} + Z_0} , \tag{A-31}$$

where Z_L is the impedance presented by the sample. Combining the above yields

$$P_{in} = \frac{1}{2}V_g^2 \frac{Z_L(Z_0 + Z_L)}{Z_0(2Z_L + Z_0)^2} . \tag{A-32}$$

For no load ($Z_L = \infty$) we get maximal output power P_{max} (A-6). Thus the difference is given by the reflected power

$$P_{refl} = \frac{V_g^2}{8Z_0}\left(\frac{Z_0}{2Z_L + Z_0}\right)^2 . \tag{A-33}$$

The absorbed power is lost in Z_L while the output power is that disippated in the termination load Z_0. The voltage across each is

$$V_{in} = V_g - Z_0 I_{in} = \frac{V_g Z_L}{2Z_L + Z_0} . \tag{A-34}$$

Thus we find that

$$P_{abs} = \frac{V_g^2}{8Z_0} \frac{4Z_0 Z_L}{(2Z_L + Z_0)^2}$$

$$P_t = \frac{V_g^2}{8Z_0}\left(\frac{2Z_L}{2Z_L + Z_0}\right)^2 , \tag{A-35}$$

and we see that

$$P_{refl} + P_{abs} + P_t = P_{max}$$

$$IL = 10 \log\left|\frac{P_{max}}{P_t}\right| = 20 \log\left(1 + \frac{Z_0}{2Z_L}\right) . \tag{A-36}$$

This is the usual result quoted in discussions of the ASTM type coaxial holder [27]. If we compare this to the previous transmission line analysis we see that the real (resistive) part of the impedance Z_{in} plays the role of $Re\{Z(-d)\}$ since the output powers are given by

$$P_{in} = \frac{1}{2}|I_{in}|^2 \, Re\{Z(-d)\} \quad \text{transmission line model}$$

$$P_{in} = \frac{1}{2}|I_{in}|^2 \, Re\{Z_{in}\} \quad \text{circuit model} . \tag{A-37}$$

Thus we may equate the two. For a good electrically thin conductor equating $Re\{Z(-d)\}$ (A-28) and $Re\{Z_{in}\}$ (A-31) yields

$$\frac{Z_0 Z_L}{Z_0 + Z_L} = \frac{Z_0}{1 + \eta_0 \sigma d} \quad \rightarrow \quad \frac{Z_L}{Z_0} = \frac{1}{\eta_0 \sigma d} . \tag{A-38}$$

The insertion loss (A-36) thus yields (A-30) with (A-38) inserted.

APPENDIX B FLANGED COAXIAL HOLDER CIRCUIT ANALYSIS

The flanged coaxial holder shown in figure 14 uses disk shaped flanges to both secure the sample and to capacitively couple fields through the material. From a circuit point of view we will represent the flanged junctions as shown in figure 15 where Z_A through Z_F represent capacitive impedances and R_A through R_F are contact resistances. An application of Kirchhoff's voltage law yields the following set of equations for the unknown currents I_1 through I_6

$$\begin{aligned}
&I_1(Z_0 + R_A + Z_L + R_E) - I_2Z_L - I_3R_A - I_5R_E = V_g \\
&I_2(Z_0 + R_B + Z_L + R_F) - I_1Z_L - I_4R_B - I_6R_F = 0 \\
&I_3(Z_A + Z_C + R_A) - I_1R_A - I_4Z_C = 0 \\
&I_4(Z_B + Z_C + R_B) - I_2R_B - I_3Z_C = 0 \\
&I_5(Z_D + Z_E + R_E) - I_1R_E - I_6Z_D = 0 \\
&I_6(Z_D + Z_F + R_F) - I_2R_F - I_5Z_D = 0 \ .
\end{aligned} \tag{B-1}$$

These equations need to be solved for I_2 in order to find the current delivered to the output impedance Z_0. Solving we find

$$I_2 = V_gB/(AC - B^2) \ , \tag{B-2}$$

where

$$\begin{aligned}
A &= Z_0 + Z_L + R_B + R_F - \frac{R_B^2(Z_A + Z_C + R_A)}{\Omega} - \frac{R_F^2(Z_E + Z_D + R_E)}{\theta} \\
B &= Z_L + \frac{R_AR_BZ_C}{\Omega} + \frac{R_ER_FZ_D}{\theta} \\
C &= Z_0 + Z_L + R_A + R_E - \frac{R_A^2(Z_B + Z_C + R_B)}{\Omega} - \frac{R_E^2(Z_F + Z_D + R_F)}{\theta} \\
\Omega &= (Z_A + Z_C + R_A)(Z_B + Z_C + R_B) - Z_C^2 \\
\theta &= (Z_E + Z_D + R_E)(Z_F + Z_D + R_F) - Z_D^2 \ .
\end{aligned} \tag{B-3}$$

Note that if we let $A' = A - B$ and $C' = C - B$ then we have

$$\begin{aligned}
A' &= Z_0 + \frac{R_B[Z_A(Z_B + Z_C) + Z_B(R_A + Z_C)]}{\Omega} + \frac{R_F[Z_E(Z_F + Z_D) + Z_F(R_E + Z_D)]}{\theta} \\
C' &= Z_0 + \frac{R_A[Z_B(Z_A + Z_C) + Z_A(R_B + Z_C)]}{\Omega} + \frac{R_E[Z_F(Z_E + Z_D) + Z_E(R_F + Z_D)]}{\theta}
\end{aligned} \tag{B-4}$$

and the output current may now be written

$$I_2 = V_g \frac{B}{B(A' + C') + A'C'} \ . \tag{B-5}$$

The power delivered to the output is thus

$$P_t = \frac{Z_0}{2}|V_g|^2 \left|\frac{B}{B(A' + C') + A'C'}\right|^2 \ . \tag{B-6}$$

If no sample is present then $Z_L \to \infty$ (open circuit) and thus $B \to \infty$. Thus

$$P_t \to \frac{Z_0}{2}|V_g|^2 \left|\frac{1}{A' + C'}\right|^2 . \tag{B-7}$$

In addition, if the flanges are tightly joined and there is no compensation material present then R_A through R_F should approach zero, yielding $A' \to Z_0$, $B \to Z_0$, and

$$P_t = |V_g|^2/8Z_0 . \tag{B-8}$$

as usual. Combining (B-6) and (B-7) the insertion loss should behave according to

$$IL = 20 \log\left|1 + \frac{A'C'}{B(A' + C')}\right| , \tag{B-9}$$

with the compensation material in place.

Let us now examine some special cases. If in fact the system behaves in an ideal sense then all the stray impedances (R_A, Z_A, etc.) will be shorted. In this case: $A' \to Z_0$, $B \to Z_L$, and $C' \to Z_0$. Thus IL (B-9) reduces to

$$IL = 20 \log\left|1 + \frac{Z_0}{2Z_L}\right| , \tag{B-10}$$

as expected.

Realistically however, these stray impedances will contribute to some degree. The flange impedances Z_A through Z_F should behave like capacitors, i.e.

$$Z \approx -j/\omega C .$$

As the operating frequency increases these impedances decrease. Thus if $\omega C >> 1$ the capacitor acts much like a short as desired. This should be the case at RF for the direct flange capacitances Z_A, Z_B, Z_E, and Z_F. Dropping these terms we have

$$\begin{aligned} A' &= C' = Z_0 \\ B &= Z_L + \frac{R_A R_B Z_C}{\Omega'} + \frac{R_E R_F Z_D}{\Theta'} \\ \Omega' &= R_A R_B + Z_C(R_A + R_B) \\ \Theta' &= R_E R_F + Z_D(R_E + R_F) . \end{aligned} \tag{B-11}$$

The remaining terms depend on the contact resistances between the material and the flanges (R_A, R_B, R_E, R_F) and the capacitive coupling to the material itself (Z_C, Z_D). For a good conductor Z_L should be small. Thus we may well have the unwanted terms in B of the same order as Z_L. If the material has very good surface conductivity, such that R_A through R_F are zero, then insertion loss tends toward the ideal value (B-10). In fact if (B-11) is valid, then we need only have good surface conductivity on one side, such as R_A, $R_E \approx 0$ or R_B, $R_F \approx 0$ and we again approach the ideal insertion loss value.

If the material has very poor surface conductivity, such that R_A, R_B >> $|Z_C|$ and R_E, R_F >> $|Z_D|$, then B in (B-11) reduces to

$$B \approx Z_L + Z_C + Z_D \ , \tag{B-12}$$

and IL becomes

$$IL = 20 \log\left|1 + \frac{Z_0}{2(Z_L + Z_C + Z_D)}\right| \ . \tag{B-13}$$

For shield materials of good conductivity such that $|Z_L| << |Z_C|, |Z_D|$ we see that unwanted impedances Z_C and Z_D can dominate the insertion loss measurement.

U. S. GOVERNMENT PRINTING OFFICE: 1986—671-641 45,189 REGION NO. 8

NBS-114A (REV. 2-8C)

U.S. DEPT. OF COMM. BIBLIOGRAPHIC DATA SHEET (See instructions)	1. PUBLICATION OR REPORT NO. NBS/TN-1095	2. Performing Organ. Report No.	3. Publication Date May 1986

4. TITLE AND SUBTITLE

A Study of Techniques for Measuring the Electromagnetic Shielding Effectiveness of Materials

5. AUTHOR(S)

Perry F. Wilson and Mark T. Ma

6. PERFORMING ORGANIZATION (If joint or other than NBS, see instructions)

NATIONAL BUREAU OF STANDARDS
DEPARTMENT OF COMMERCE
WASHINGTON, D.C. 20234

7. Contract/Grant No.

8. Type of Report & Period Covered

9. SPONSORING ORGANIZATION NAME AND COMPLETE ADDRESS (Street, City, State, ZIP)

Sponsored in part by
U.S. Army Aviation Systems Command
St. Louis, Missouri 63120

10. SUPPLEMENTARY NOTES

☐ Document describes a computer program; SF-185, FIPS Software Summary, is attached.

11. ABSTRACT (A 200-word or less factual summary of most significant information. If document includes a significant bibliography or literature survey, mention it here)

Shielding effectiveness relates to a material's ability to reduce the transmission of propagating fields in order to electromagnetically isolate one region from another. Because a complex material's shielding capability is difficult to predict, it often must be measured. A number of measurement approaches are studied including the use of a shielded room, coaxial transmission line holders, time domain signals, the dual TEM cell, and an apertured TEM cell in a reverberation chamber. In each case, we consider the system's frequency range, test sample requirements, test field type, dynamic range, time required, analytical background, and present data taken on a common set of materials.

12. KEY WORDS (Six to twelve entries; alphabetical order; capitalize only proper names; and separate key words by semicolons)

aperture coupling; coaxial transmission line holders; dual TEM cell; frequency domain; measurement techniques; reverberation chamber; shielded room; shieling effectiveness; shielding materials; time domain.

13. AVAILABILITY

☒ Unlimited

☐ For Official Distribution. Do Not Release to NTIS

☒ Order From Superintendent of Documents, U.S. Government Printing Office, Washington, D.C. 20402.

☐ Order From National Technical Information Service (NTIS), Springfield, VA. 22161

14. NO. OF PRINTED PAGES 72

15. Price

NBS Technical Publications

Periodical

Journal of Research—The Journal of Research of the National Bureau of Standards reports NBS research and development in those disciplines of the physical and engineering sciences in which the Bureau is active. These include physics, chemistry, engineering, mathematics, and computer sciences. Papers cover a broad range of subjects, with major emphasis on measurement methodology and the basic technology underlying standardization. Also included from time to time are survey articles on topics closely related to the Bureau's technical and scientific programs. Issued six times a year.

Nonperiodicals

Monographs—Major contributions to the technical literature on various subjects related to the Bureau's scientific and technical activities.

Handbooks—Recommended codes of engineering and industrial practice (including safety codes) developed in cooperation with interested industries, professional organizations, and regulatory bodies.

Special Publications—Include proceedings of conferences sponsored by NBS, NBS annual reports, and other special publications appropriate to this grouping such as wall charts, pocket cards, and bibliographies.

Applied Mathematics Series—Mathematical tables, manuals, and studies of special interest to physicists, engineers, chemists, biologists, mathematicians, computer programmers, and others engaged in scientific and technical work.

National Standard Reference Data Series—Provides quantitative data on the physical and chemical properties of materials, compiled from the world's literature and critically evaluated. Developed under a worldwide program coordinated by NBS under the authority of the National Standard Data Act (Public Law 90-396). NOTE: The Journal of Physical and Chemical Reference Data (JPCRD) is published quarterly for NBS by the American Chemical Society (ACS) and the American Institute of Physics (AIP). Subscriptions, reprints, and supplements are available from ACS, 1155 Sixteenth St., NW, Washington, DC 20056.

Building Science Series—Disseminates technical information developed at the Bureau on building materials, components, systems, and whole structures. The series presents research results, test methods, and performance criteria related to the structural and environmental functions and the durability and safety characteristics of building elements and systems.

Technical Notes—Studies or reports which are complete in themselves but restrictive in their treatment of a subject. Analogous to monographs but not so comprehensive in scope or definitive in treatment of the subject area. Often serve as a vehicle for final reports of work performed at NBS under the sponsorship of other government agencies.

Voluntary Product Standards—Developed under procedures published by the Department of Commerce in Part 10, Title 15, of the Code of Federal Regulations. The standards establish nationally recognized requirements for products, and provide all concerned interests with a basis for common understanding of the characteristics of the products. NBS administers this program as a supplement to the activities of the private sector standardizing organizations.

Consumer Information Series—Practical information, based on NBS research and experience, covering areas of interest to the consumer. Easily understandable language and illustrations provide useful background knowledge for shopping in today's technological marketplace.

Order the **above** *NBS publications from: Superintendent of Documents, Government Printing Office, Washington, DC 20402.*

Order the **following** *NBS publications—FIPS and NBSIR's—from the National Technical Information Service, Springfield, VA 22161.*

Federal Information Processing Standards Publications (FIPS PUB)—Publications in this series collectively constitute the Federal Information Processing Standards Register. The Register serves as the official source of information in the Federal Government regarding standards issued by NBS pursuant to the Federal Property and Administrative Services Act of 1949 as amended, Public Law 89-306 (79 Stat. 1127), and as implemented by Executive Order 11717 (38 FR 12315, dated May 11, 1973) and Part 6 of Title 15 CFR (Code of Federal Regulations).

NBS Interagency Reports (NBSIR)—A special series of interim or final reports on work performed by NBS for outside sponsors (both government and non-government). In general, initial distribution is handled by the sponsor; public distribution is by the National Technical Information Service, Springfield, VA 22161, in paper copy or microfiche form.

U.S. Department of Commerce
National Bureau of Standards
Gaithersburg, MD 20899

Official Business
Penalty for Private Use $300

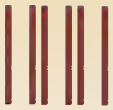

POSTAGE AND FEES PAID
U.S. DEPARTMENT OF COMMERCE
COM-215

SPECIAL FOURTH-CLASS RATE
BOOK